# Nodal design of lattice mechanical metamaterials

Xueyan Chen

UBFC
UNIVERSITÉ
BOURGOGNE FRANCHE-COMTÉ

哈爾濱工業大學
HARBIN INSTITUTE OF TECHNOLOGY

Thèse de doctorat en co-tutelle de l'Université Bourgogne Franche-Comté et de Harbin University of Technology

École doctorale n° 37
Sciences Pour l'Ingénieur et Microtechniques

Doctorat de Mécanique

Par

Xueyan Chen

# Métamatériaux en treillis
# *Nodal design of lattice mechanical metamaterials*

Soutenue à Harbin, Chine, le 09 juillet 2021

Composition du Jury :

| | | |
|---|---|---|
| Gengkai Hu | Président | Professeur, Beijing Institute of Technology |
| Claude Boutin | Rapporteur | Professeur, Université de Lyon |
| Corentin Coulais | Rapporteur | Assistant professor, University of Amsterdam |
| Yuesheng Wang | Examinateur | Professeur, Tianjin University |
| Vincent Laude | Co-directeur | Directeur de recherche, Université Bourgogne Franche-Comté |
| Huifeng Tan | Co-directeur | Professeur, Harbin University of Technology |
| Muamer Kadic | Encadrant | Maître de conférences, Université Bourgogne Franche-Comté |

# Acknowledgments

I would like to express my deepest acknowledge to my three supervisors, Professor Vincent Laude, Professor Muamer Kadic and Professor Huifeng Tan, for their financial support and academic guidance during the times I stayed in UBFC and HIT.

I am also thankful to my colleagues and my friends at UBFC and HIT for their technical support and spiritual accompany. Special thanks to Professor Sébastien Euphrasie, Professor Gwenn Ulliac, Dr.Johnny Moughames, Julio Andrés Iglesias Martínez, Dr. Nicolas Laforge, Samia Adrar , Dr.Xiong bo, Dr. Xiling Luo, Dr.Lin Yu, Dr. Ruiqiang Ma, Dr. Teng ma, Dr. liuyi Yang, Dr. Yongzheng Shen, Dr. Yu zhao and many lovely guys who are not mentioned in this list. I especially acknowledge my best friend Dr. Qingxiang Ji for his encouragement and help during the stay in France.

I greatly thanks the HIT and UBFC for their financial support of this work.

I am particular grateful to my family for their support and understanding during my whole life. Lastly, I owe a debt of gratitude to my wife, Fengying Tai, for her selfless dedication and support without reservation.

# Contents

# General Introduction

During the last two decades, periodic lattice materials, a class of new mechanical metamaterials, have attracted considerable attention due to their outstanding mechanical properties, such as high specific stiffness [Berger 17], high specific strength [Chen 20a, Jang 13, Zheng 14], controlled Poisson's ratio [Bückmann 12, Yang 20, Bückmann 14], tailored anisotropy [Tancogne-Dejean 18a], high energy absorption and ability to recovery after unloading [Frenzel 16, Jang 13]. As a typical structure, joints or nodes with complex geometrical configuration at the connection between rods and rods are commonly found in lattice materials. The existence of nodes will definitely have impact on the mechanical properties of the lattice materials.

For low-density lattice materials, researchers usually ignore the effects of nodal overlapping volume and complex geometry on their overall performance. Recently, with advance in 3D printing technology, a large number of high relative lattice materials [Gu 15, Tancogne-Dejean 16], which possess excellent performance beyond people's imagination, are prepared. Their unusual properties cannot be well explained by traditional theoretical models [Deshpande 01a]. In the first chapter, we establish a new theoretical prediction model for the high density octet lattice. The nodal effects on the mechanical properties of lattice materials are also analyzed in detail.

From the loading support view, hollow truss lattices have shown better mechanical properties in contrast to solid truss lattice [Schaedler 11]. The nodal effect also has a significant impact on the mechanical properties of hollow lattice materials. During deformation, the stress concentration phenomenon can be found around the nodes and the hollow parts have poor resistance to deformation. This makes it easy for lattices to fail at the nodes and the performance of the material to remain far from expectations. Moreover, hollow lattice materials are highly sensitive to defects. During the preparation process, the material is prone to defects at the nodes. The existence of defects will significantly affect the mechanical properties of lattice materials, such as the elastic modulus, the load-bearing capacity, the energy absorption characteristics and Poisson's ratio. In the second chapter, by introducing spherical nodes and smooth connection around nodes, we design a stretching-dominated mechanical metamaterial that can absorb very large energies while at the same time retaining a low density. A few examples of lattice materials are considered and we show that a new class of body centered cubic (BCC) shellular metamaterials has the best mechanical properties for shock absorption: they are ultrastiff, ultrastrong, and they possess high specific energy absorption at a low relative density.

After realizing the nodal effect of solid and hollow lattice materials, we try to tailor the mechanical behavior of simple cubic (SC) lattice using what we obtained from the previous study. As the last member of the elementary cubic truss family, the simple-cubic truss lattice, possessing the highest stiffness and strength along the principal directions, plays an important role in load-bearing mechanical metamaterials. Highly anisotropic mechanical properties and low resistance to buckling loading and shearing loading, however, limit its use in energy absorption. In the third chapter, we present a class of simple-cubic closed tubular lattice with limited loading direction dependence along with high mechanical properties and irregular stable post-yield response. The fabrication of its complex structure was made possible by direct laser writing at the microscale. Experiments and simulations demonstrate that both the elastic modulus and the yield strength of the simple-cubic closed tubular lattice are significantly larger than those of the simple-cubic truss lattice, regardless of the loading direction. At a relative density of 0.1 and compared to the truss lattice, the closed tubular lattice can absorb respectively 4.45 times and 6.14 times as much energy along directions [100] and [110]. Its average normalized Young's modulus and yield strength are respectively 28% and 53% larger than those of the most outstanding shellular metamaterial with the same mass. Such excellent mechanical properties make it a promising candidate for applications to load-bearing and energy absorption.

The choice of node provides one with another possibility to control the elastic isotropy of lattice materials. Well-designed stretching-dominated lattices indeed play an important role to achieve elastic behaviour in addition to their high specific stiffness and strength. However, their high anisotropic and instable nonlinear mechanical properties limit their applications to energy absorption. Meanwhile, bending-dominated lattices are well known for high energy absorption capacity and incredibly stable nonlinear responses. In the fourth chapter, we propose a new class of light-weight elastic isotropic bending-dominated truss lattice by replacing the inner node of the BCC lattice with a SC lattice. We use analytical and numerical predictions for the design of their elastic moduli and collapse strength. Additional numerical simulations reveal that the proposed lattices not only exhibit elastic isotropy but also nearly isotropic nonlinear response. In particular, our material with relative density below 1% almost attains the upper bound of Poisson's ratio for isotropic materials. Uniaxial compression tests are performed to confirm the design. Results show that the fabricated materials have a relative modulus 2 times larger and a relative collapse strength and specific energy absorption about 1.6 times larger in constrast to BCC truss lattices. Thus, our material can be consider as a noteworthy alternative to bear loadings and to absorb energy.

Finally, we propose a new class of isotropic and reusable cork-like metamaterial that is designed from an hybrid truss-lattice material with complex node connections to show an isotropic Poisson's ratio close to zero. Optimization is conducted using a multi-objective genetic algorithm, assisted by an elliptical basis function neural network, and coupled with finite element simulations. The optimal micro-structured metamaterial, fabricated by two-photon lithography with a lat-

tice constant of 300 μm, has an almost isotropic Poisson's ratio smaller than 0.08 in all directions. It can recover 96.6% of its original shape after a compressional test exceeding 20% strain.

# Chapter I
# An effective length model for octet lattices

## I.1 Introduction

During the last two decades, periodic lattice materials, a class of mechanical metamaterials, have attracted considerable attention due to their outstanding mechanical properties [Coulais 18, Florijn 14, Milton 95, Schittny 14, Frenzel 19, Frenzel 17, Zhu 19, Tao 20, Tan 19, Tan 20, Chen 20c, Chen 20d, Chen 21] such as high specific stiffness[Berger 17], high specific strength [Chen 20a, Jang 13, Zheng 14], controlled Poisson's ratio [Bückmann 12, Yang 20, Bückmann 14], high energy absorption and ability to recovery after unloading [Frenzel 16, Jang 13]. Early experiments performed by Deshpande et al. have shown that a well-designed periodic truss lattice material exhibits much higher mechanical properties than non-periodic structural materials of equal mass such as commercially available aluminum foams [Deshpande 01a]. Thus, truss lattice materials are very promising, especially when combined with current additive manufacturing techniques such as selective laser melting or direct laser writing (DLW) [Deubel 04, Kadic 12, Blasco 16].

As pointed out by Gibson and Ashby, the mechanical properties of truss lattice materials are determined by structural topology and geometrical parameters besides the base material [Gibson 99a]. For instance, the stiffness and the strength of lattice materials that are governed by the bending of micro-components scale non-linearly with the relative density (with an exponent between 1.5 and 2), while for lattice materials that deform in stretching mode, both stiffness and strength are expected to scale linearly. Later, Deshpande et al. identified the topological criteria for dictating the deformation mechanism of truss lattice materials [Deshpande 01b]. Henceforth, truss lattice materials can be topologically categorized as either bending-dominated or stretching-dominated. Their study showed that the deformation mechanisms in lattice materials were determined by their nodal connectivity and the minimum nodal connectivity for 2D and 3D stretching-dominated lattice materials was 6 and 12 respectively.

Octet lattices play an important role in stretching-dominated lattices for their outstanding mechanical properties. In early works, researchers paid more attention to octet lattices with low relative density. Their effective mechanical properties was studied by Deshapande et al. both experimentally and theoretically [Deshpande 01a]. They found that for small aspect ratio, $r/l$, the effect of bending moment on compressive properties could be negligible and the pin-jointed assumption sufficed. The effective mechanical properties linearly scale with relative density. The relative compressive stiffness and strength are given by $\overline{E} = \overline{\rho}/9$ and $\overline{\sigma} = \overline{\rho}/3$ respectively, where $\overline{\rho}$ is the relative density of the octet lattice material. As technology advances in 3D printing, octet lattice materials can be made with a wide range of strut aspect ratios. A recent parametric finite element study carried out by Tancogne-Dejean et al. indicated that the relative compressive stiffness for relative density higher than 0.1 scaled with a power exponent higher

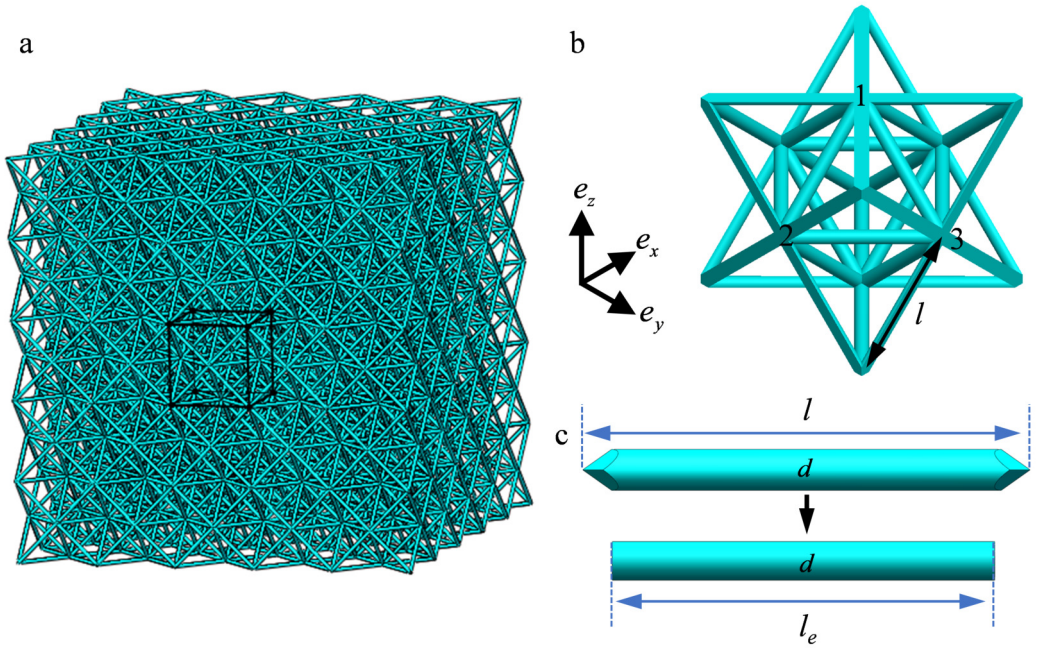


Figure I.1: Geometrical model of (a) octet lattice and corresponding representative unit cell. (c) The process to obtain effective length: convert from actual strut to perfect cylindrical strut.

than 1 [Tancogne-Dejean 16]. In other word, the ideal linear model gives quite low predictions for large ratio ranges. Hence, there is a need to develop a satisfying theoretical model for large aspect ratio ranges.

In this chapter, an effective length is defined to calculate the effective compressive stiffness and strength of octet lattices. Predictions are validated by both finite element simulations and experiments. Effects of strut joint, bend and shear on the relative compressive stiffness and strength are further discussed.

## I.2 Relative density of octet lattice material and equivalent length of strut

A unit cell of octet lattice material is shown in Figure I.1b, which can be stacked in three principal directions to construct the entire structure's geometry shown in Figure I.1a. The unit cell consists of 36 cylindrical struts with same length $l$. For a perfect cylindrical strut with a constant radius $r$, a first-order approximation of the relative density is given by

$$\overline{\rho} = 6\sqrt{2}\pi \left(\frac{r}{l}\right)^2 . \tag{I.1}$$

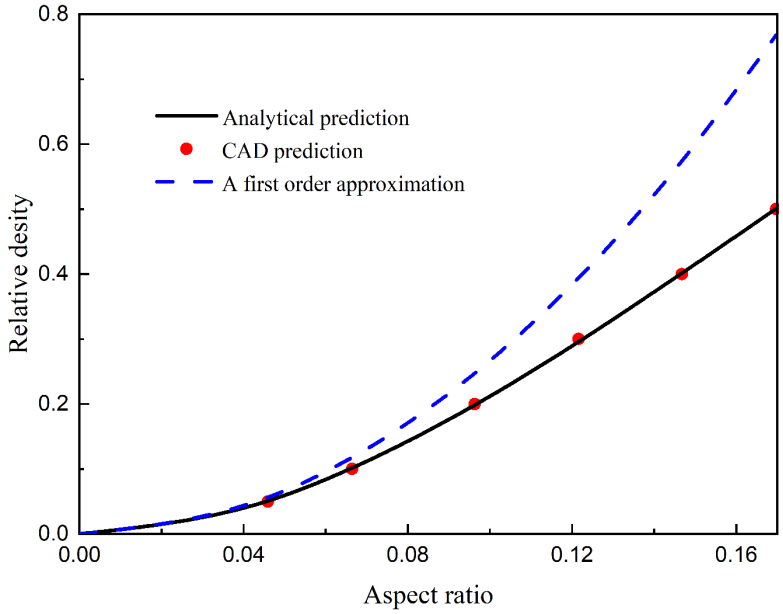


Figure I.2: Evolution of relative density as a function of strut aspect ratio, as obtained from the first order approximation [Deshpande 01a], CAD prediction and analytical prediction, respectively.

However, the above analytical relationship is only valid for low relative density due to strut joint effect. To mathematically analyze the octet unit cell, the actual geometry of individual struts need to be taken into account. As is shown in Figure I.1c, both ends of a micro strut have very complex and non-smooth surfaces. It is difficult to exactly determine the actual radius of the whole strut. In this study, the strut radius is assumed to be constant. An effective strut length $l_e$ is introduced by equaling the volume of an ideal perfect strut with that of the actual one. Consider the overlapping parts of struts in the unit cell, the actual volume of a micro-strut can be obtained by integration as

$$V_l = \pi r^2 l_e, \tag{I.2}$$

where the effective strut length can be written as:

$$l_e = \left(1 - \left(\sqrt{(2)} + \frac{2}{\pi}\right)\frac{r}{l}\right) l. \tag{I.3}$$

It can be easily obtained that the equivalent length is determined by the aspect ratio, $r/l$, of struts. If the aspect ratio is small enough, $l_e$ can be approximated by $l$. When the aspect ratio is large, $l_e$ is far smaller than $l$ and the strut joint effect must be considered in the relative density calculation.

As some struts in a unit cell are shared by adjacent cells, the total volume of strut in the unit cell is $V = 24\pi r^2 l_e$. Here, the volume of unit cell is $V_c = 2\sqrt{2}l^3$. Then, the relative density of octet lattice material can be rewritten as

$$\overline{\rho} = \frac{V_c}{V} = 6\sqrt{2}\pi \left(\frac{r}{l}\right)^2 \frac{l_e}{l}. \tag{I.4}$$

In Figure I.2, the evolution of relative density as a function of strut aspect ratio is shown for both Equation I.1 and Equation I.4. To compare the effectiveness of both equations, the CAD prediction for the relative density is also given in the same figure. From the figure, the error with Equation I.1 increases compared to the CAD prediction as the aspect ratio increases. Inevitably, prediction errors will also affect the accuracy of theoretical predictions for relative compressive stiffness and strength, which are of critical importance for cellular materials. However, Equation I.4, that account for the nodal overlapping effect, is always in good agreement with CAD results for all aspect ratios considered in this work.

## I.3 Analytical model

### I.3.1 Determination of the compressive stiffness

As detailed in the previous section, the irregular geometrical structure of struts also affects theoretical derivations. Considering that bending beam theory is only applicable to perfect struts, $l_e$ will be used in the following for energy computations, instead of $l$.

As a result of symmetry, the struts shown in Figure I.1b can be divided into three types, labeled as 12, 13 and 23, according to their spatial direction. When the octet lattice structure is under uniaxial compression, both ends of the micro struts are able to move in the three main directions. These struts can be considered as doubly clamped beams subjected to an axial stretching force, a bending moment and a shear load.

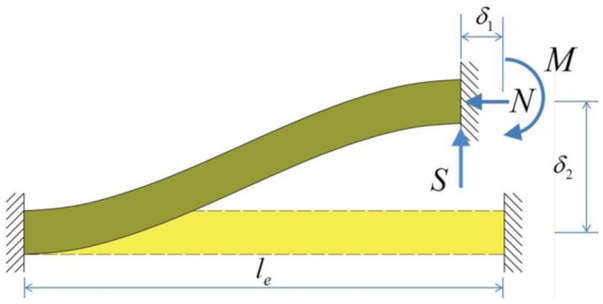


Figure I.3: Force analysis on a strut when the unit cell is under uniaxial compression.

Considering the doubly clamped beam 12 shown in Figure I.3, the relative displacement between 1 and 2 can be determined by the unknown global displacements $u$ and $w$ as $(u, 0, w)$. The axial displacement $\delta_1$ of strut 12 is given by

$$\delta_1 = u\cos\theta - w\sin\theta = \frac{\sqrt{2}}{2}(u - w). \tag{I.5}$$

Based on Timoshenko's beam theory, the axial force $N$ is given by

$$N = E_s A \frac{\delta_1}{l_e}, \tag{I.6}$$

where $E_s$ is Young's modulus of the strut material, $A$ is the cross-sectional area of the strut. For a perfectly cylindrical strut, $A$ is given by $\pi r^2$.

The bending and shearing deflection $\delta_2$ of strut 12 is written as

$$\delta_2 = u\cos\theta + w\sin\theta = \frac{\sqrt{2}}{2}(u+w). \tag{I.7}$$

The bending and shearing energy stored in strut 12 is given by

$$U_{12}^1 = \int_0^{l_e} \frac{(M-Sx)^2}{2E_s I} + \frac{S^2}{2G\kappa A}\, dx, \tag{I.8}$$

where $S$ is the shear force in the strut, $M$ is the bending moment at both ends given by $Sl_e/2$, $I$ is the moment inertia of the beam given by $\pi r^4/4$ for a circular cross section, $G$ is the shear modulus of the strut material, $\kappa$ is the shear coefficient given by [MISSING EQUATION?] for a circular beam.

Note that the relationship between $\delta_2$ and $U_{12}^1$ is given by

$$\delta_2 = \frac{\partial U_{12}^1}{\partial S} = \frac{S l_e^3}{12 E_s I}\left(1 + \frac{12EI}{G\kappa A l_e^2}\right). \tag{I.9}$$

Hence, the shear force $S$ is expressed as

$$S = \frac{12 K_1 E_s I \delta_2}{l_e^3}, \tag{I.10}$$

where $K_1 = 1/\left(1 + 12E_s I/G\kappa A l_e^2\right)$ is the bending and shearing coefficient of the beam. The elastic strain energy stored in strut 12 is given by

$$\begin{aligned} U_{12} &= \int_0^{l_e} \frac{N^2}{2E_s A} + \frac{(M-Sx)^2}{2E_s I} + \frac{S^2}{2G\kappa A}\, dx \\ &= \frac{E_s A}{4 l_e}(u-w)^2 + \frac{3K_1 E_s I}{l_e^3}(u+w)^2. \end{aligned} \tag{I.11}$$

The same analysis methodology can be adopted to obtain the elastic strain energy of struts 13 and 23. The axial displacement and bending and shearing deflection of strut 23 are given by

$$\delta_3 = u\cos\theta + v\sin\theta = \frac{\sqrt{2}}{2}(u+v), \tag{I.12}$$

$$\delta_4 = u\cos\theta - v\sin\theta = \frac{\sqrt{2}}{2}(u-v). \tag{I.13}$$

Then the elastic strain energy stored in strut 23 is written by

$$\begin{aligned} U_{23} &= \int_0^{l_e} \frac{N^2}{2E_sA} + \frac{(M-Sx)^2}{2E_sI} + \frac{S^2}{2G\kappa A}\,dx \\ &= \frac{E_sA}{4l_e}(u+v)^2 + \frac{3K_1E_sI}{l_e^3}(u-v)^2. \end{aligned} \tag{I.14}$$

The axial displacement and bending and shearing deflection of strut 13 can be written in terms of unknown displacement $v$ and $w$ as

$$\delta_5 = v\cos\theta - w\sin\theta = \frac{\sqrt{2}}{2}(v-w), \tag{I.15}$$

$$\delta_6 = v\cos\theta + w\sin\theta = \frac{\sqrt{2}}{2}(v+w). \tag{I.16}$$

The elastic strain energy stored in strut 13 is given by

$$\begin{aligned} U_{13} &= \int_0^{l_e} \frac{N^2}{2E_sA} + \frac{(M-Sx)^2}{2E_sI} + \frac{S^2}{2G\kappa A}\,dx \\ &= \frac{E_sA}{4l_e}(v-w)^2 + \frac{3K_1E_sI}{l_e^3}(v+w)^2. \end{aligned} \tag{I.17}$$

Considering the overlapping part of micro struts at the boundary, the total elastic strain energy per unit cell is written

$$\begin{aligned} U = 8(U_{12}+U_{23}+U_{13}) = \frac{2E_sA}{l_e}\Big\{&\left[(u-w)^2+(u+v)^2+(v-w)^2\right] \\ &+K_2\left[(u+w)^2+(u-v)^2+(v+w)^2\right]\Big\}, \end{aligned} \tag{I.18}$$

where $K_2 = 12K_1I/Al_e^2 = 3K_1(r/l_e)^2$ is the coupling coefficient of the beam.

The external work done by the surface stress can be written as

$$Q = 4L^2\sigma_z w. \tag{I.19}$$

The total potential energy $V$ per unit cell can be obtained as

$$\begin{aligned} V = U - Q = \frac{2E_sA}{l_e}\Big\{&\left[(u-w)^2+(u+v)^2+(v-w)^2\right] \\ &+K_2\left[(u+w)^2+(u-v)^2+(v+w)^2\right]\Big\} - 4L^2\sigma_z w. \end{aligned} \tag{I.20}$$

Based on the theorem of minimum potential energy, the partial differentials of the total potential energy with respect to the unknown displacements $u$, $v$ and $w$ vanish, leading to

$$\begin{cases} \dfrac{\partial V}{\partial u} = \dfrac{4E_sA}{l_e}\left[2(1+K_2)u + (1-K_2)v - (1-K_2)w\right] = 0, \\ \dfrac{\partial V}{\partial v} = \dfrac{4E_sA}{l_e}\left[(1-K_2)u + 2(1+K_2)v - (1-K_2)w\right] = 0, \\ \dfrac{\partial V}{\partial w} = \dfrac{4E_sA}{l_e}\left[-(1-K_2)u - (1-K_2)v + 2(1+K_2)w - \dfrac{l^2l_e\sigma_z}{E_sA}\right] = 0. \end{cases} \tag{I.21}$$

Then the unknown displacements $u$, $v$ and $w$ can be obtained by solving the above equations as

$$\begin{cases} u = \dfrac{1-K_2}{3K_2+1}\dfrac{l^2 l_e}{4E_s A}\sigma_z, \\ v = \dfrac{1-K_2}{3K_2+1}\dfrac{l^2 l_e}{4E_s A}\sigma_z, \\ w = \dfrac{K_2+3}{3K_2+1}\dfrac{l^2 l_e}{4E_s A}\sigma_z. \end{cases} \tag{I.22}$$

Hence, the compressive strain $\varepsilon_z$ per unit cell is given by

$$\varepsilon_z = \frac{2w}{\sqrt{2}l} = \frac{K_2+3}{3K_2+1}\frac{\sqrt{2}ll_e}{4E_s A}\sigma_z. \tag{I.23}$$

So the relative compressive stiffness of the octet lattice material is written as

$$\bar{E} = \frac{\sigma_z}{\varepsilon_z}/E_s = \frac{1}{9}ab\bar{\rho}, \tag{I.24}$$

where

$$a = \left(\frac{l}{l_e}\right)^2 = \left[\frac{1}{1-\left(\sqrt{2}+\frac{2}{\pi}\right)\frac{r}{l}}\right]^2, \tag{I.25}$$

and

$$b = 1 + \frac{8K_2}{K_2+3}. \tag{I.26}$$

Note that $a$ and $b$ are nodal modifying and bending coupling coefficients, respectively. $a$ is determined by the aspect ratio of the strut and $b$ depends on the coupling effect of bending and shearing. Obviously, $a$ is larger than 1, which will always increase the compressive stiffness of octet lattice. $b$, accounting for bending moment and shearing force, is also no less than one, which again increases the compressive stiffness. From Equation I.25 and Equation I.26, the nodal and bending effects are second-order quantities compared to the compressive stiffness. If the relative density of the octet lattice material is small enough, both $a$ and $b$ can be approximated by 1, which means that modifications of strut joint and bending can be ignored. Therefore, the ideal linear analytical model suggested by Deshapande et al. is valid for small relative densities [Deshpande 01a]. At high relative densities, the strut joint effect and the bending effect need to be taken into account.

### I.3.2 Determination of the collapse strength

The strut joint effect is taken into account to predict the collapse strength of the octet lattice material. Under compression, the octet lattice structure collapses either by plastic yielding or elastic buckling of the struts, depending on its relative density [Deshpande 01a].

At low relative density, the lattice structure fails by elastic buckling before plastic yielding. According to Equation I.5, Equation I.6, Equation I.12, Equation I.15 and Equation I.22, the axial forces in struts 12, 13 and 23 are given by

$$N_{12} = N_{13} = -\frac{\sqrt{2}}{4}\frac{1+K_2}{1+3K_2}l^2\sigma_z, \tag{I.27}$$

$$N_{23} = \frac{\sqrt{2}}{4}\frac{1-K_2}{1+3K_2}l^2\sigma_z. \tag{I.28}$$

From Equation I.27 and Equation I.28, it can be seen that struts 12 and 13 are subjected to compressive loading, while strut 23 is subjected to axial tension. In this case, the failure of the lattice material is dominated by the elastic buckling of struts 12 and 13. According to the theorem of Timoshenko and Gere, the elastic buckling stress is given by

$$\sigma_E = \frac{n^2\pi^2 E_s}{4}\left(\frac{r}{l_e}\right)^2, \tag{I.29}$$

where $n$ is the end constraint factor depending on the supporting conditions at both strut ends. Here, struts are assumed to be rigid-jointed. Thus, the rotational stiffness of the nodes is zero and $n = 2$. Hence, failure resulting from elastic buckling is

$$\sigma_E^Z = \frac{\sqrt{(2)}}{36}\pi E_s a^4 c\bar{\rho}^2, \tag{I.30}$$

with

$$c = \frac{3K_2+1}{K_2+1}. \tag{I.31}$$

The factor $c$ is always larger than 1, which implies that the bending and shearing coupling effect increase buckling strength.

At high relative densities, struts are strong enough to avoid the occurrence of elastic buckling. Octet lattice material will then collapse by plastic yielding of the struts. The maximum normal stress in struts 12 and 13 resulting from compressive loading and bending moment is given by

$$\sigma_{12}^{max} = \sigma_{23}^{max} = \frac{N}{A} + \frac{Mr}{I} = \frac{1+K_2+12K_1\dfrac{r}{l_e}}{1+3K_2}\frac{\sqrt{2}l^2}{4A}\sigma_z. \tag{I.32}$$

The normal stress in strut 23 is given by

$$\sigma_{23} = \frac{1-K_2}{1+3K_2}\frac{\sqrt{2}l^2}{4A}\sigma_z. \tag{I.33}$$

Comparing Equation I.32 and Equation I.33, one finds that struts 12 and 13, which undergo much stronger stress at both ends, are the first to yield. As a result, the octet lattice material turns to elasticity-plasticity. It is worth noting the octet lattice structure can still undergo more compressive loading until strut 23 begins

to yield and the compressive response becomes nonlinear. The initial collapse strength of the lattice material is obtained as

$$\sigma_Y^Z = \frac{\bar{\rho}}{3} de \sigma_y, \tag{I.34}$$

with

$$d = \frac{l}{l_e} \tag{I.35}$$

and

$$e = \frac{l + 3K_2}{1 - K_2}. \tag{I.36}$$

The factors $d$ and $e$ are modifications of strut joint and bending effect, respectively. It can be seen that both $d$ and $e$ are larger than 1, which means the strut joint effect and the bending and shearing effect increase the compressive strength. The strut joint modifying coefficient and bending modifying coefficient are first-order and second-order quantities as compared to the compressive strength. At low relative density, the strut joint effect and the bending and shearing effect can be neglected. The ideal linear analytical model works well. When the relative density of the lattice material is large enough, the bending and shearing effect of strut must be considered.

## I.4 Experiments

### I.4.1 Manufacturing specimens

Specimens of an octet lattice material and a dog-bone material used for tensile test were manufactured on an selective laser sintering (SLA) machine from 3D Systems, PROX* SLS 500, with a laser power of 100 W. DuraForm* PA, a 3D printable version of Polypropylene material commercially supplied by 3D Systems, was used as the base material. Octet lattice specimens were fabricated with several relative densities ranging from 10% to 30%. For each relative density, two specimens were manufactured for uniaxial compression experiments. Specimens comprise $5 \times 5 \times 5$ (125) unit cells. The strut diameter of specimens was fixed as 1.4 mm, and the sizes of specimens depending on strut length were varied to study the effect of relative density on compressive stiffness and strength. The strut length decreased with an increase in relative densities. Strut lengths were 10.5, 8.5, 7.3, 6.4 and 5.7 $mm$, respectively, which corresponded to the relative densities $\bar{\rho} = 0.1, 0.15, 0.2, 0.25, 0.3$. Table I.1 summarizes dimensions and weight of the specimens. From Table I.1, one can see that the measured dimensions are larger by about 1% compared to the design dimensions. In addition, the calculated relative densities of specimen are shown in Table I.1. The measured density of the base material is 1 $g/cm^3$. At low relative density, the mass error is less than 10%. At high relative density, the maximum mass error is about 16%.

| Specimen number | Mass (g) | Design dimension (mm) | Building direction 1 (mm) | Building direction 2 (mm) | Building direction 3 (mm) | Relative density (%) |
|---|---|---|---|---|---|---|
| 1 | 41.87 | 74.25 | 74.33 | 74.3 | 74.31 | 10.22 |
| 2 | 40.5 | 74.25 | 74.16 | 74.25 | 74.31 | 9.69 |
| 3 | 27 | 60.1 | 60.22 | 60.13 | 60.25 | 12.41 |
| 4 | 27.1 | 60.1 | 60.19 | 60.22 | 60.25 | 12.45 |
| 5 | 27.21 | 51.62 | 51.66 | 51.67 | 51.65 | 20 |
| 6 | 28.44 | 51.62 | 51.63 | 51.73 | 51.67 | 21 |
| 7 | 20.8 | 45.25 | 45.28 | 45.34 | 45.32 | 22 |
| 8 | 21.1 | 45.25 | 45.47 | 45.34 | 45.3 | 23 |
| 9 | 22.4 | 40.31 | 40.52 | 40.37 | 40.35 | 34 |
| 10 | 23.48 | 40.31 | 40.42 | 40.39 | 40.33 | 35 |

Table I.1: Geometrical parameters of the specimens.

### I.4.2 Tensile stress-strain curve of the base material

To obtain the material properties of the base material, five printed dog-bone specimens according to the ASTM standard 638 were manufactured for uniaxial tensile test. The dog-bone specimens were printed edgewise with length along the direction of the struts of the octet lattice structure. The tensile test on printed dog-bone specimens was conducted using a SHMADZU machine with a 5 kN load cell at a nominal strain rate of $10^{-3}s^{-1}$, as shown in Figure I.4a. Two extensometers were used to measure vertical and horizontal deformations of the gauge section. The stress-strain curve of the tensile specimen is shown in Figure I.4a. Young's modulus is measured to be about 1.78 GPa and the 0.2% offset yield stress is found to be 24 MPa. Poisson's ratio is calculated to be 0.44. One can also find that an ultimate strength of about 43 MPa is found at a strain of 14%.

### I.4.3 Uniaxial compressive test on the octet lattice material

The compressive response of the octet lattice material was tested using a SHMADZU machine with 50 kN load cell at a nominal strain rate of $10^{-3}s^{-1}$. Due to complex geometry of the octet lattice structure, it was difficult to apply an extensometer to measure strain directly. Here, an experimental procedure similar to Bonatti and Mohr's was employed to determine the elastic modulus of the tested specimens [Bonatti 17a]. The printed specimens were placed between two polished steel platens with a suitable pre-load force which was applied to make sure no slip between platens and specimens. Digital Image Correlation (DIC) black speckles were applied onto the surface of the tested specimens with an average speckle size of 60 $\mu m$. Two digital cameras equipped with 50 mm macro lenses were employed to capture the deformation in one lateral direction of the specimen surface. The

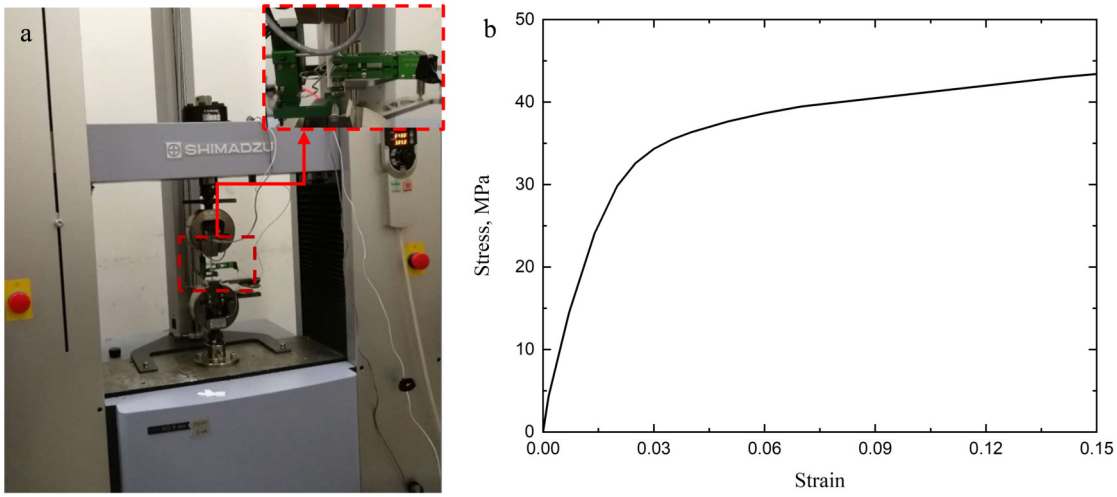


Figure I.4: (a)Tensile test for 3D printed dog-bone specimens using SHMADZU machine and extensometer. (b) Tensile stress-strain curve of printed PA dog-bone specimen.

work distance from the digital cameras to the specimen surface was about 450 mm. A calibration board (4 $mm$) shown in Figure I.5 was used to calibrate the camera system. DIC images were conducted in Vic-3D with a subset size of 31 pixels and a step size of 4 pixels. As illustrated in Figure I.5 b, the elastic modulus was calculated based on the axial strain measured from 8 reference circles at the central row of unit cells. The engineering stress and strain were obtained by dividing the force and displacement by the specimen cross sectional area and height, respectively.

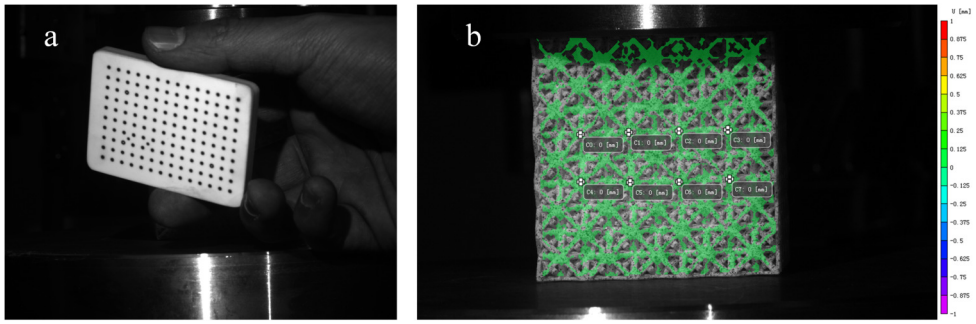


Figure I.5: (a) A calibration board (4mm) used for calibrating the camera system, (b) Position of reference area used to determine the elastic modulus.

## I.5 Numerical analysis

To validate the presented theoretical approach, a series of finite element models were built by using the commercial finite element software ABAQUS. The material is modeled by using a simple plasticity model with isotropic hardening. The linear

hardening stress-strain curve is obtained from the previous tensile experiment. Here, Young's modulus and yield stress are assumed to be 1.78 GPa and 24 MPa, respectively. Poisson's ratio adopted in finite element models is 0.44.

Figure I.6 shows a series of unit cell models with different relative densities adopted in the FE analysis. For all unit cell models, the strut radius is 0.7 $mm$ and the strut length changes with the relative density. The strut length is 10.5, 8.5, 7.3, 6.4, 0.32 and 5.7 $mm$, respectively, which corresponded to the relative density $\bar{\rho} = (0.1, 0.15, 0.2, 0.25, 0.3)$. THe strut in the unit cell is composed of thousands of first-order solid elements (type C3D8R). Element sizes vary from models to models, depending upon the diameter to length ratio. For the same strut diameter, the element sizes increases as the strut length decreases. Given the symmetrical nature of the problem, periodic boundary conditions are applied on unit cell models [Li 04]. A global strain up to 5% is applied to obtain the yield stress.

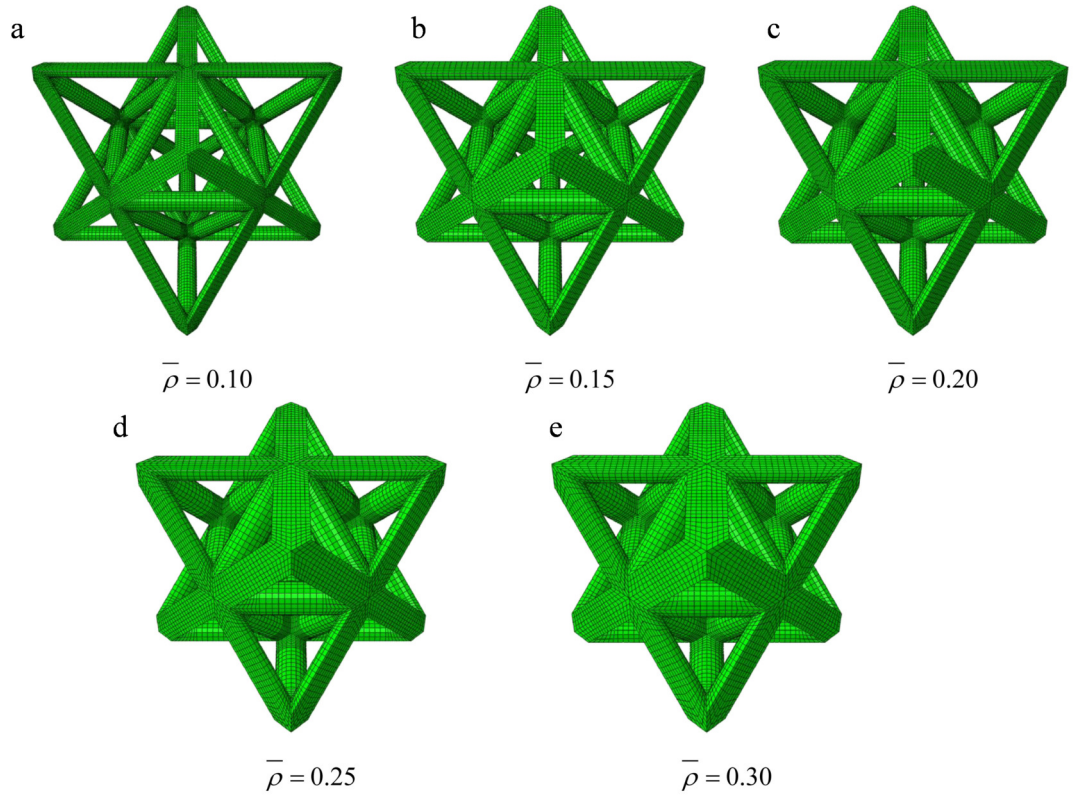


Figure I.6: Finite element models of the octet truss lattice with different relative densities.

## I.6 Results and discussions

### I.6.1 Compressive response of the octet lattice material

Figure I.7 shows the compressive response of the printed specimens with different relative densities. After an initially linear elastic phase, the engineering stress-strain response turns to a nonlinear increasing phase, up to a first peak stress. The latter is affected by the relative density of the tested specimens. As the relative density increases, the peak stress and the corresponding engineering strain increase. The lowest peak stress of nearly 1 MPa is reached at the lowest relative density of 0.1, whereas the highest peak stress of nearly 5.68 MPa is reached at the highest relative density of 0.34.

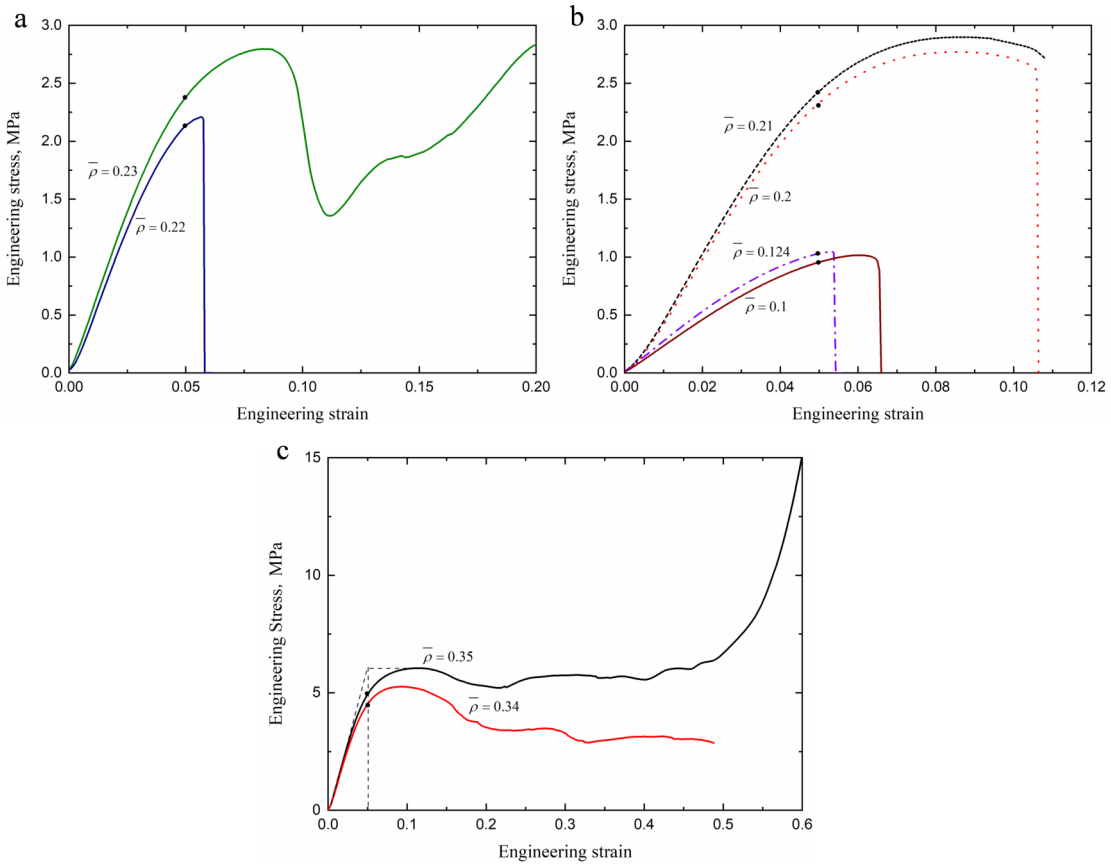


Figure I.7: Experimental stress-strain curves of the printed specimens with different relative densities under uniaxial compression: (a) low relative densities, (b) transition zone, and (c) high relative densities.

The deformations of the tested specimens at the first peak stress are shown in Figure I.8. After reaching a first peak stress, a decrease in stress is observed in all configurations and is due to the brittle fracture of the polymer struts. Subsequently, the tested specimens with low relative density loose their loading capacity. For other configurations, an increase in stress can be observed after a decrease in stress.

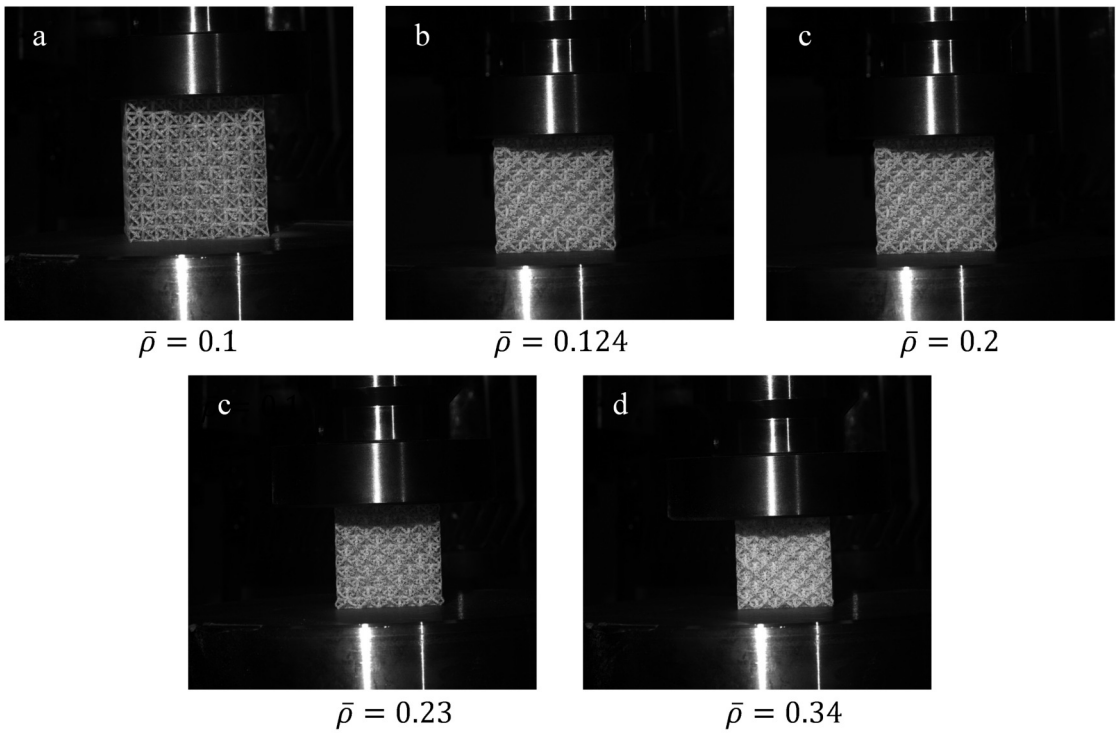


Figure I.8: Deformation of samples with different relative density under peak force.

Difference in mechanical properties between tested specimens can be attributed to the different failure modes of the configurations. At low relative density, the tested specimens fail by unstable shear mode, as shown in Figure I.8(a). Struts are too slender to stand axial stress resulting from bending moment and tension force. The brittle fracture of struts 12 near the strut joints lead to the collapse of the octet lattice structure. For the tested specimens with high relative density, struts are strong enough to stand axial stress and tensile yield failure of struts 23 dominates the failure of the tested specimens. It is found in Figure I.6(b) and Figure I.9 that the compressive response of the tested specimens changes from an unstable shear mode to a stable buckling free mode at a relative density between 0.22 and 0.23.

The yield strain is defined by an engineering strain at the intersection of the tangents of linear and nonlinear phases, and is nearly 5%. The corresponding stresses, highlighted in Figure I.7, are defined to be the yield stress of the tested specimens. It is clear that the elastic modulus, the yield stress and the peak strength all increase with relative density. At low relative density, the yield stress is close to the peak stress which demonstrates that brittle fracture of struts 12 and 13 occurs shortly after tensile yield of struts 23. With an increase in the strut aspect ratio, differences between the yield stress and the peak stress increase.

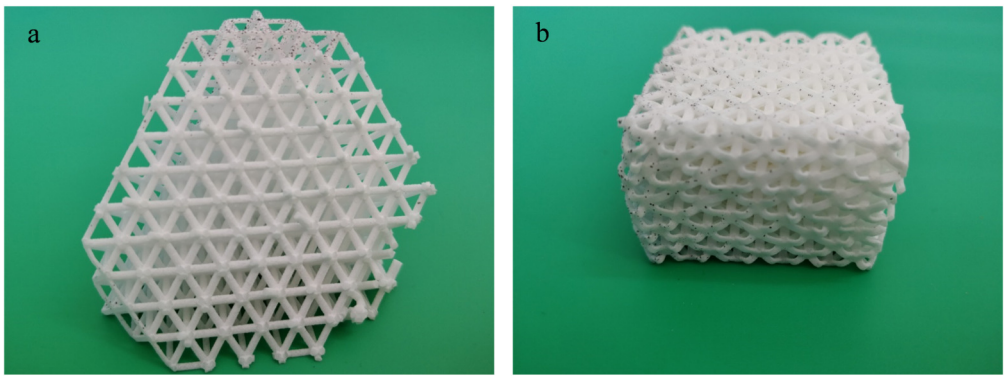


Figure I.9: Failure modes of the tested specimens: (a) shear failure and (b) stable buckling failure.

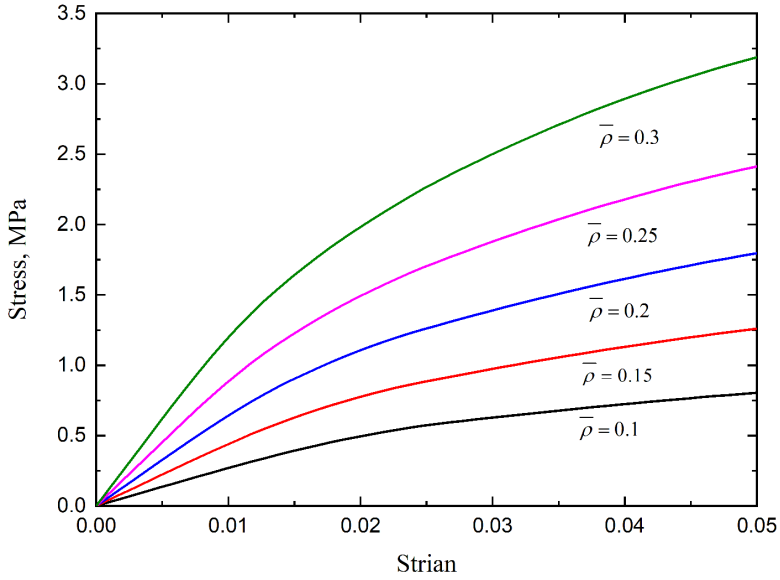


Figure I.10: Stress strain curves for different relative densities obtained from the numerical approach.

Figure I.10 shows stress-strain curves for different relative densities obtained from the numerical approach. The numerical models capture an initial linear elastic behavior followed by an increasing nonlinear plastic behavior, which has been validated by experimental results. It can be seen that the compressive responses are monotonically increasing. With an increase in relative density, the elastic modulus and yield strength increase. However, there are slight differences between the predicted and experimental results. Underestimations of the yield strength result from the variable diameter and from powders present on strut surfaces which are not considered in FE simulations.

### I.6.2 Effect of strut joint, bend and shear on compressive modulus and strength

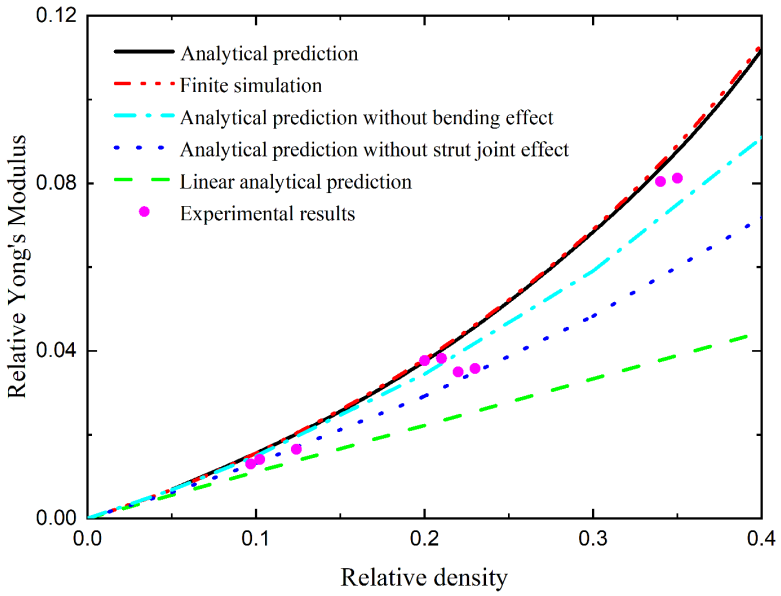


Figure I.11: Comparison of predictions for the relative Young's modulus from theory, finite element simulation, and experiment.

To recognize the roles of strut joint, bend and shear in analytical derivations, Figure I.11 shows a comparison of the relative Young's modulus for different relative densities obtained from experimental results, from theoretical considerations, and from numerical simulations. It is clear that the analytical model accounting for strut joint, bend and shear agrees well with both numerical and experimental results. As can be seen from Figure I.11, both the linear and bending analytical models give serious differences as the relative density becomes larger. For example, there are differences of about 19.4% and 10.1% between analytical and FE predictions for relative density 0.05. However, the analytical model, though only accounting for the strut joint, can give a more approximate prediction. The prediction error compared to the FE simulation is only 8% for relative density 0.2. When the relative density increases, the prediction error is significantly higher. This demonstrates that the effect of compressive stiffness not only depends on the relative density, but also relates to the effect of the strut joint, bend and shear. At low relative density, the strut joint effect is the dominating factor in stiffness analytical derivations. However, the importance of bend and shear are more obvious as the relative density increases.

Figure I.12 shows the evolution of the relative yield strength as a function of the relative density. The linear and the nonlinear predictions are shown in the figure with dotted and solid lines, respectively. From the figure, one finds that the improved analytical model is in better agreement with experimental results compared to the linear analytical model. It is also found that, as the relative density

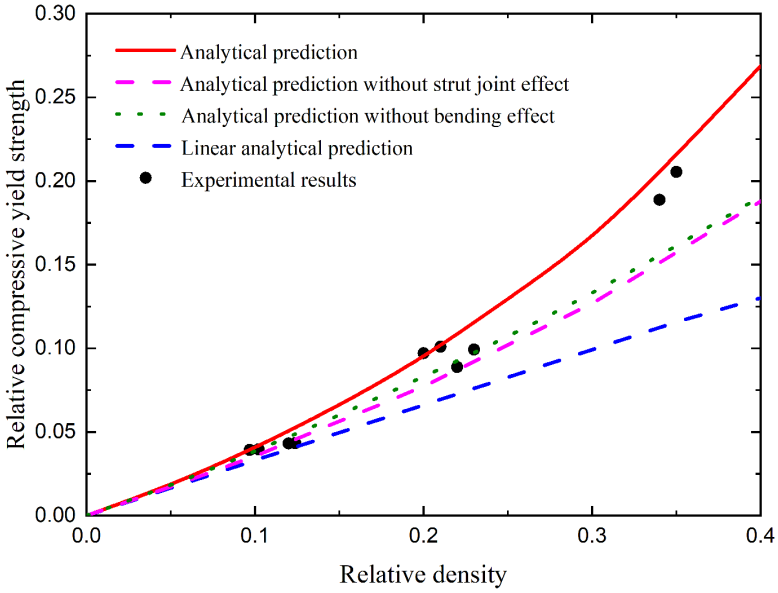


Figure I.12: Evolution of the relative yield strength as a function of the relative density.

increases, the relative yield strength increases. The gradient of the yield strength increases with the relative density. From these results, it can be concluded that the strut joint effect and the shearing and bending effect play an important role in the compressive strength of the octet lattice material. The coupling effect between the shearing force and the bending moment can also increase the compressive strength, especially for the strut lattice.

## I.7 Conclusions

An analytical model considering the influence of material overlapping on the strut joint, bend and shear has been derived. The model can be used to predict the compressive stiffness and strength of the octet lattice material with cylindrical struts. The analytical model shows a good agreement with both FE simulations and experimental results. This agreement validates the model.

Specimens of the octet lattice material were manufactured from PA. Compressive experimental results show that the compressive response of the octet lattice material changes from an unstable shear mode to a stable buckling free mode at a relative density between 0.22 and 0.23. The findings in this chapter may be helpful to provide a guidance for material design. Moreover, the relative compressive stiffness and strength not only depend on the relative density, but also relate to the effect of the strut joint, bend and shear. At low relative density, the strut joint effect is the dominating factor in stiffness analytical derivations. However, the importance of bend and shear are more obvious with an increase in the relative density.

# Chapter II

# Light-weight shell-lattice metamaterials for mechanical shock absorption

## II.1 Introduction

Absorbing mechanical shocks and vibration energy is crucial in industrial, domestic and medical applications [Khelif 16, Babaee 16, Craster 12]. Very often, systems (such as hydraulic cylinder) or structures (such as helmets) are used to achieve energy absorption – or protection – from impacts or periodic vibrations. In this respect, mechanical metamaterials have received much attention in recent years due to their extraordinary mechanical properties, including outstanding specific stiffness and strength [Gibson 99b, Deshpande 01a, Bonatti 17b, Bonatti 19b], and energy absorption [Valdevit 13]. Recently, scientists have shown that metamaterials based on bending-dominated buckling inclusions can absorb more energy than commercially available aluminum foams. This method is very promising, especially when combined with current fabrications techniques such as 3D micro and macro printing. Body-centered cubic (BCC) lattice materials are the best-known bending-dominated materials [Ushijima 11, Gümrük 13, Tancogne-Dejean 18d]. Such metamaterials, however, lack scalability toward extremely low densities [Schaedler 11] – instabilities disappear together with the stiffness. Furthermore, the bending-dominated behavior localizes the plasticity regions toward the hinges.

Here, we design a stretching-dominated mechanical metamaterial that can absorb very large energies while at the same time retaining a low density. In this study, a few examples of lattice materials are considered and we show that a new class of BCC shellular metamaterials has the best mechanical properties for shock absorption: they are ultrastiff, ultrastrong, and possess high specific energy absorption at a low relative density. The mechanical properties are calculated numerically and verified experimentally under uniaxial compression. Compared to octet lattice metamaterials, our metamaterial has a relative elastic modulus 2.4 times larger and a relative compressive strength about 5.4 times larger, for a relative density of 10%.

## II.2 Design and Fabrication of Metamaterials

### II.2.1 BCC shellular lattice design

One of the crucial limiting aspect in 3D buckling/absorbing metamaterials is the ratio between the volume of material that is really used (for deformation of absorption) compared to the total volume of the host material. In other words, one needs to optimize all hinges and bending parts such that they deform homogeneously. Obviously, the simplest candidate would be the homogeneous material itself. However, one also needs to decrease the volume and thus to create inner holes. Holes thus become the real playground for optimization.

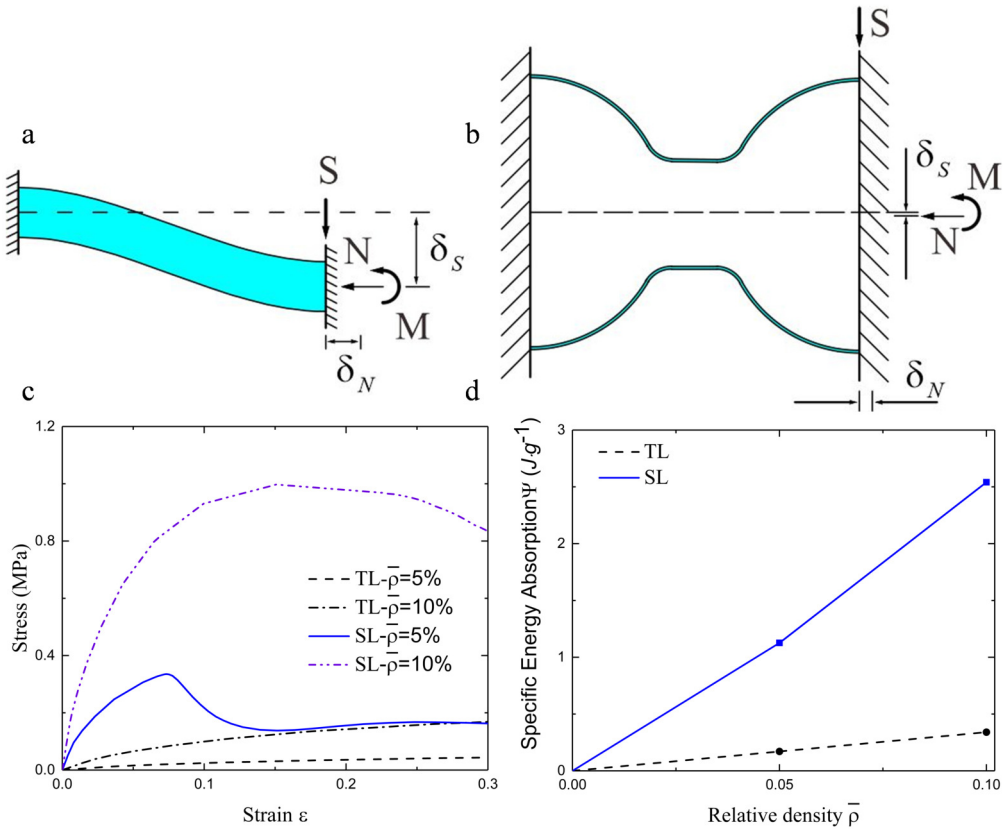


Figure II.1: Simplified doubly clamped beam model of (a) bending-dominated truss-lattice (TL) metamaterial and of (b) variable cross-section shell model of stretching-dominated shell-lattice (SL) metamaterial. Deformations under axial compressing force, bending moment and shearing load are shown. Under the same loading conditions, the shell model appears to have less axial and deflection displacements than the beam model. (c) Compressive stress-strain curves obtained from finite simulations. SL has higher elastic modulus and strength than TL. (d) The specific energy absorption (SEA) of SL is almost 4 times larger at low relative density.

We show in Figure II.1 the stiffness and the potential energy absorption that one can aim at using standard bending-dominated metamaterials versus stretching-dominated materials. The stretching-dominated mechanism appears clearly as a much better candidate for energy absorption.

Figure II.2(a) and (c) display the geometry of the bending-dominated truss-lattice (TL) metamaterial and its corresponding unit cell model which consists of eight struts. Here, the cross-section of each strut is assumed to be circular with a constant diameter $d$ and a length $l$. As presented by Ushijima et al., the relative density of the TL metamaterial is the ratio of the actual volume occupied by the lattice structure to the volume of the overall structure [Ushijima 11], or

$$\bar{\rho} = \frac{3\sqrt{3}\pi}{4}\left(\frac{d}{l}\right)^2. \tag{II.1}$$

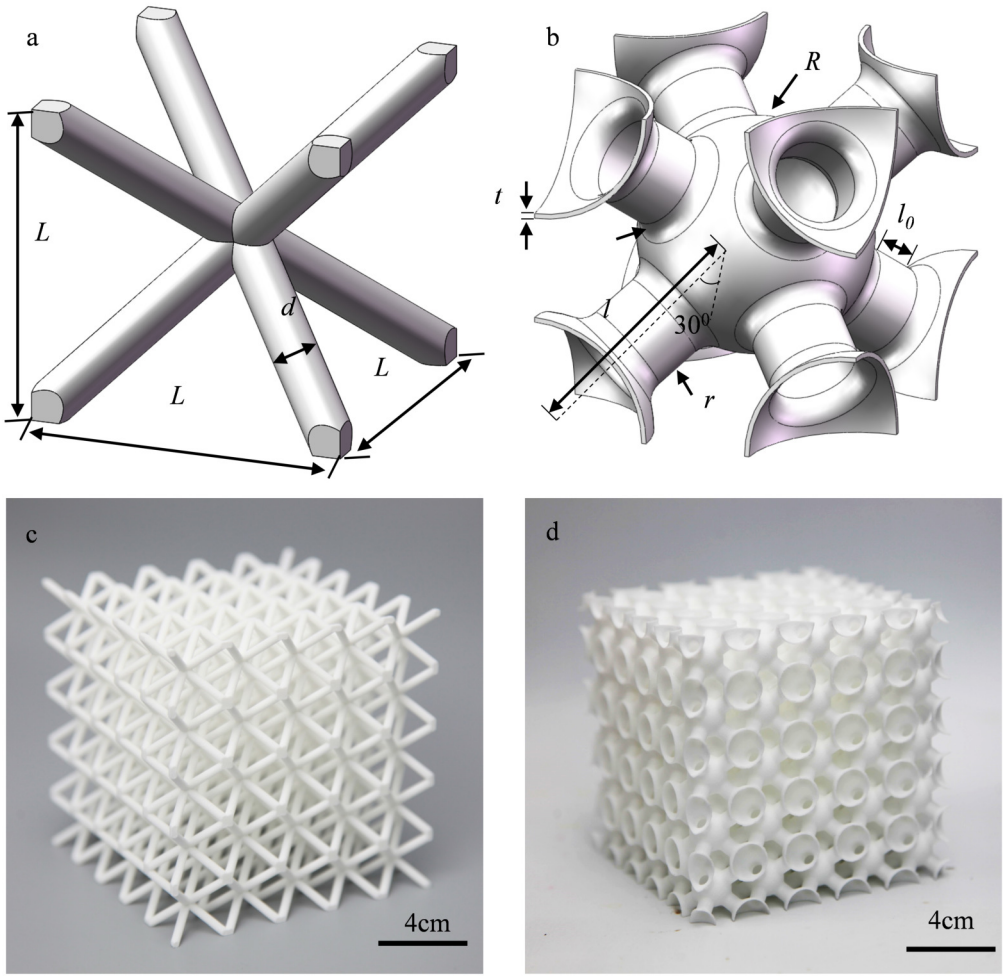


Figure II.2: Representative photographs of (a) bending-dominated TL and (b) stretching-dominated SL samples are shown. The unit-cells of (c) TL and (d) SL metamaterials have a base-centered cubic (BCC) symmetry. Important geometrical parameters are shown.

However, the above analytical relationship is only valid for TL metamaterials with very low relative density. At high relative density, the influence of material overlap at the nodes cannot be neglected. Subtracting the overlap volume at the nodes, a more precise expression for the relative density is [Gümrük 13]

$$\overline{\rho} = \frac{3\sqrt{3}\pi}{4}\left(\frac{d}{l}\right)^2 - \frac{9\sqrt{2}}{2}\left(\frac{d}{l}\right)^3. \tag{II.2}$$

Figure II.2(b) and (d) show a configuration of stretching-dominated shell-lattice (SL) metamaterials and its corresponding unit cell model. The SL unit cell is composed of a spherical shell, which has circular openings on the eight lateral corners, and of four cylindrical shells. The adjacent parts are connected by a smooth variable cross-section cylindrical shell. The unit cell model can be geometrically described by four main parameters, that are the radius of the spherical shell $R$,

the radius of the cylindrical shell $r$ , the length of the cylindrical shell $l_0$, and the wall thickness $t$. With a given inclination angle of 30°, the radius of the variable cross-section cylindrical shell is given by

$$r_0 = 2R - r. \tag{II.3}$$

and the total length of the shell strut is expressed as

$$l = l_0 + 2\sqrt{3}(R - r). \tag{II.4}$$

Hence, the analytical expression for the relative density of SL metamaterial is

$$\overline{\rho} = \frac{V}{(\frac{2}{\sqrt{3}}l)^3}, \tag{II.5}$$

where $V$ is the unit cell volume of the SL metamaterial and is given by

$$V = V_c + V_s, \tag{II.6}$$

with the volume of the cylinder shell struts

$$V_c = 8\pi(2r - t)l_0 t \tag{II.7}$$

and the volume of the spherical shell nodes

$$V_s = 8\pi t \left[\frac{4}{3}\pi(R - r)^2 + (4\sqrt{3} - \frac{2\pi}{3})(R - r)(2r - t) - 3R(R - t) - t^2\right]. \tag{II.8}$$

### II.2.2 Experimental samples

We designed stretching-dominated shell-lattice (SL) metamaterials and compared them to standard bending-dominated truss-lattice (TL) metamaterials. Samples were fabricated by selective laser sintering (SLS) using a 3D printer (EOS model P110) with the base material PA 2200 (EOS Nylon 12), using a laser power of 30 W and a scanning speed of 5 m/s. The operational temperature was 190°C and the layer thickness was 0.06 mm. Representative samples and their unit-cells are displayed in Figure II.2. As a note, all structures presented here are anisotropic due to cubic symmetry. We only consider in experiments the (1,0,0) direction, which is one of three principal directions and the strongest of them, as representative for the investigation of the compressive response. Each specimen comprises $5 \times 5 \times 5$ unit cells and features a strut length $l = 17.32$ mm. Three configurations and relative densities $\bar{\rho} = 0.05$ or 0.10 were investigated. Configuration TL has strut diameter $d = 1.01$ mm or 1.45 mm (Figure II.2a and Figure II.2c). Two different SL configurations were selected in order to investigate the effect of parameters $R/r$ and $l_0/(l - l_0)$ on mechanical properties. Configuration SL1 is composed of small ball shells and long cylindrical shell struts ($R = 6.94$ mm, $r = 2.78$ mm, $l_0/(l - l_0) = 0.2$). The wall thickness $t$ is either 0.29 mm or 0.59 mm. Configuration SL2 is composed of large ball shells and short cylindrical shell struts ($R = 8.04$ mm, $r = 3.5$ mm, $l_0/(l - l_0) = 0.1$). The wall thickness $t$ is either 0.23 mm or 0.56 mm. For each configuration, two samples were manufactured for uniaxial compression experiments. The maximum dimensional error between as-designed and measured samples was 0.8%. As a note, the smallest relative density of about 5% was imposed by fabrication constraints.

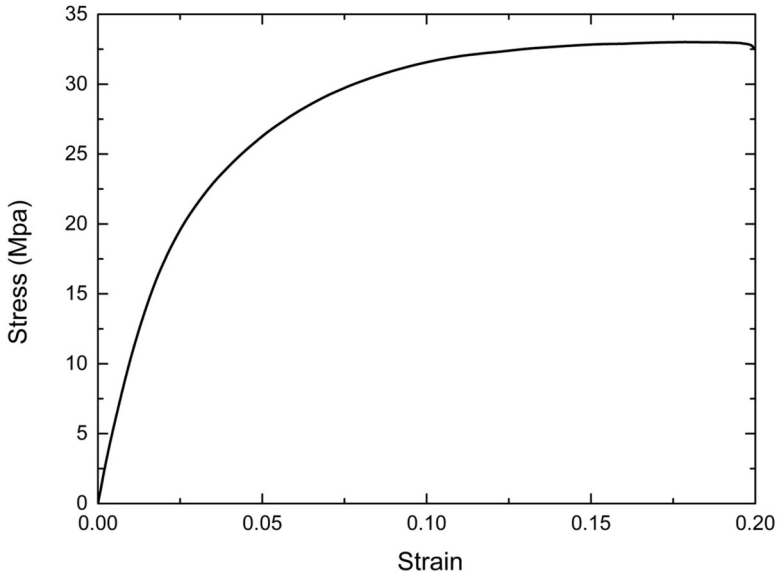


Figure II.3: Tensile stress-strain curve of the dog-bone specimen.

## II.3 Characterization

To obtain the mechanical properties of parent material PA2200, five dog-bone specimens were manufactured according to the ASTM 638 standard with the same laser processing as used to build lattice and shellular structures for uniaxial tensile test. The uniaxial tensile test on the printed dog-bone specimens were performed on a 5 kN SHMADZU testing machine at a nominal strain rate of $10^{-3}$ $s^{-1}$. The axial tensile deformations of the tested specimens were measured by a mechanical gripping type extensometer. Figure II.3 shows the stress-strain curve of the tensile specimen. The average elastic modulus is about 1.17 GPa and the 0.2% offset yield stress is nearly 14.09 MPa. The ultimate strength is about 33 MPa and the corresponding strain is 20%.

Once fabricated, samples were experimentally tested under uniaxial loading. Quasi-static compression tests were conducted on an Instron machine with 50 kN load cell at a nominal strain rate of $10^{-3}$ $s^{-1}$. Samples were positioned between two polished steel platens with suitable preload forces applied to ensure no slip. During the test, samples were placed in the center of the loading device to avoid the influence of eccentric forces. Tests were continued until the onset of densification. Engineering stresses were calculated by dividing measured loads by the specimen cross sections. Engineering strains were obtained by dividing the displacement of the moving platen by the specimen height.

Figure II.4(a-d) shows compressive deformations of the samples at a relative density of 5%. The TL sample exhibits a monotonically increasing engineering compressive response. After an initial linear phase, the stress-strain curve turns into a weakly increasing elastic-plastic phase. After an initial elastic phase followed by an infinitesimal nonlinear increasing behavior, the response of SL1 reaches a

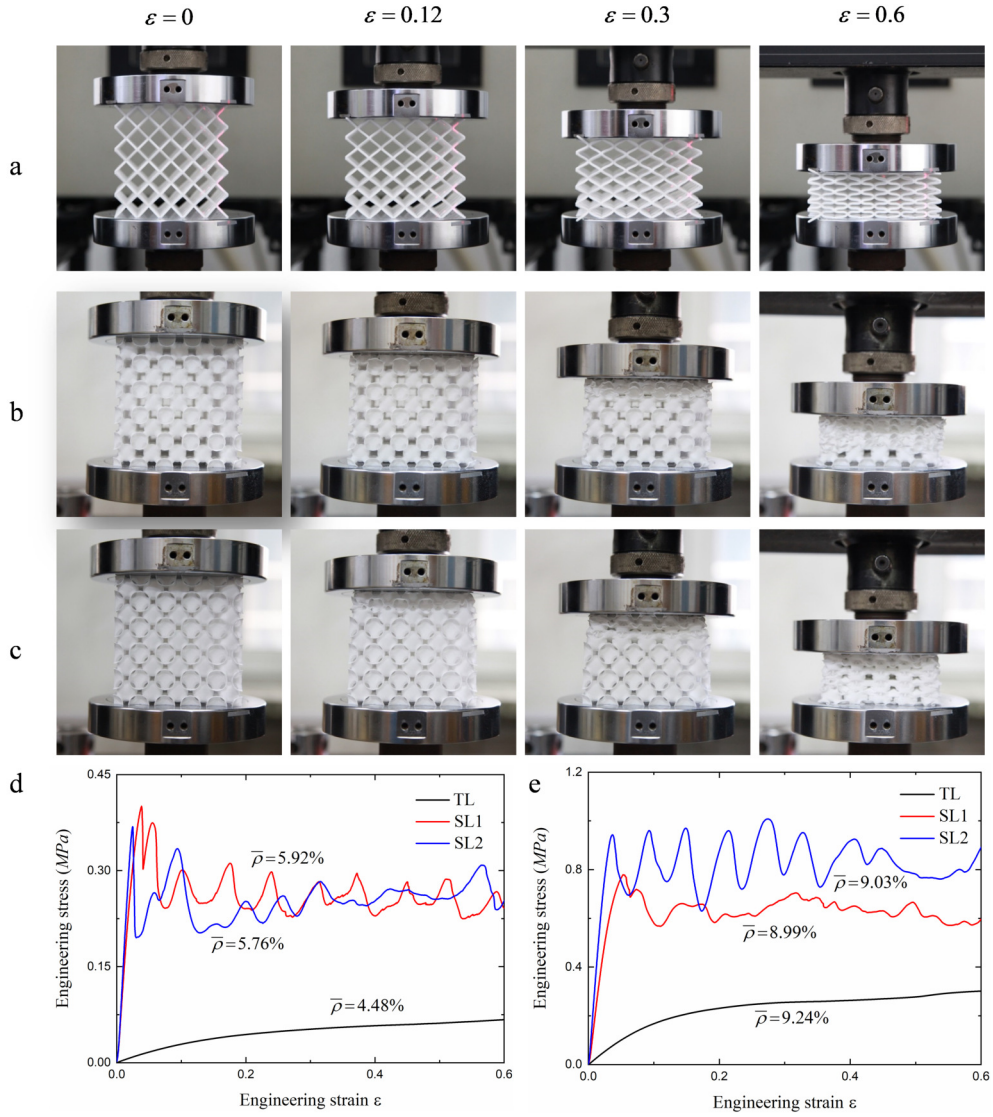


Figure II.4: Compressive deformations of (a) TL, (b) SL1 and (c) SL2 samples are shown as a function of strain. For strains of 0.12, top and bottom surfaces of the TL sample are not entirely in contact with the compression platens. The error from this defect in the applied load is likely to be small, and certainly far less than the effect of geometry which can be neglected. The particular photographs shown are for a relative density of 5%. (corresponding images for a relative density of 10% are shown in Figure A.1). Engineering stress-strain curves are shown for a relative density of 5% in panel (d) and 10% in panel (e).

first peak stress of about 0.4 MPa followed by buckling oscillations. The main differences between SL1 and SL2 are that the first hump of SL2 has lower amplitude and its elastic modulus is larger. For both SL samples, a weakly damped oscillation stress-strain response can be observed. During the compression test, the struts of the TL sample are mainly subjected to bending moments, whereas the deformation of the TL samples are uniform. It is observed that the SL samples are

collapsing from upper to lower boundaries in a layer by layer fashion. Figure A.1 and Figure II.4(e) show compressive deformations and responses of the samples at a relative density of 10%. The compressive response of TL and SL1 samples show trends similar to those at 5% relative density. Their collapsing modes are also unchanged. Interestingly, SL2 at 10% relative density has the highest modulus and strength among all configurations. SL2 collapses from upper and lower boundaries to middle plane in a layer by layer fashion. The deformation mode is also more stable compared with other configurations and there is no obvious attenuation in amplitude oscillations.

## II.4 Simulation

A series of unit-cell models with different relative densities were built using the commercial finite element software ABAQUS with first-order solid elements (type C3D8R). The constituent material (PA 2200) was assumed to be isotropic and is modeled as a perfectly elasto-plastic material. The stress-strain curve is obtained from a tensile test. For PA 2200, Poisson's ratio is usually set to be 0.4. For all models, the edge length of unit cells is fixed to 2 mm. The corresponding strut diameter for TL and wall thickness for SL change with relative density. For the SL unit cell, there are four solid elements along the wall thickness direction at low relative density. Five solid elements through thickness were used in high relative density models. To improve the calculation accuracy, periodic boundary conditions are applied. The compressive strength due to yield and buckling is extracted from the simulations. Buckling strengths were obtained by eigenvalue buckling analysis, following Valdevit *et al.* [Valdevit 13]. The yield strength can be defined as the first peak in the stress-strain curve calculated by elastic-plastic analysis. For the TL metamaterial, $\epsilon = 7\%$ is chosen as the collapsing strain and the corresponding strength is taken as the yield strength.

## II.5 Results and discussion

The parameters chosen for SL metamaterials were obtained from numerical analysis and are optimal for the chosen relative densities. Figure II.5 shows the variation of the relative compressive stiffness and of the strength of SL metamaterials as a function of geometrical parameters $R/r$ and $l_0/(l - l_0)$.

When $R/r$ is smaller than 2.5, a tiny increase followed by a continuous decrease in elastic modulus is found. When $R/r$ is larger than 2.5, the compressive modulus is a monotonic decreasing function of $l_0/(l - l_0)$. When $l_0/(l - l_0)$ is larger than 0.2, the compressive modulus decreases with $R/r$. Similar trends are found in Figure II.5(c) and Figure II.5(e). The only difference is that the transition value of $R/r$ decreases as the relative density increases.

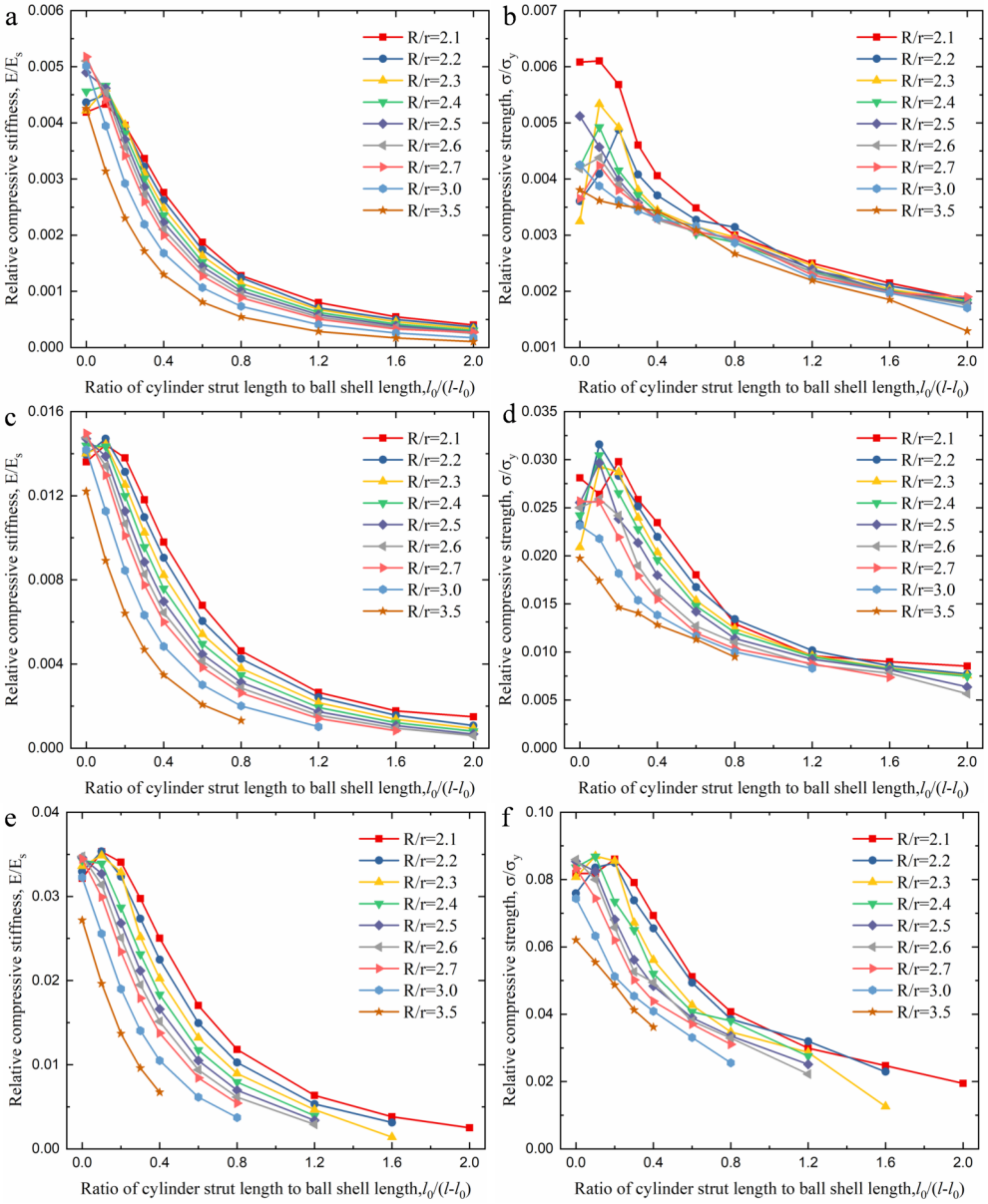


Figure II.5: Optimization of SL metamaterial: the compressive stiffness and strength of SL metamaterial with relative densities of 0.02, 0.05 and 0.10 are plotted as a function of geometrical parameters $R/r$ and $l_0/(l-l_0)$.

Similarly, the maximum compressive strengths are always found for $l_0/(l-l_0)$ smaller than 0.3. However, compared with the stiffness curves, the variations of compressive strength are more disordered at small $R/r$. That may contribute to the occurrence of local buckling at low relative density, which decreases the compressive strength significantly. The main conclusion of this analysis is that in order to achieve the best compressive performance the interval of geometrical parameters is $R/r = 2.1$ to 2.5 and $l_0/(l-l_0) = 0.1$ to 0.3.

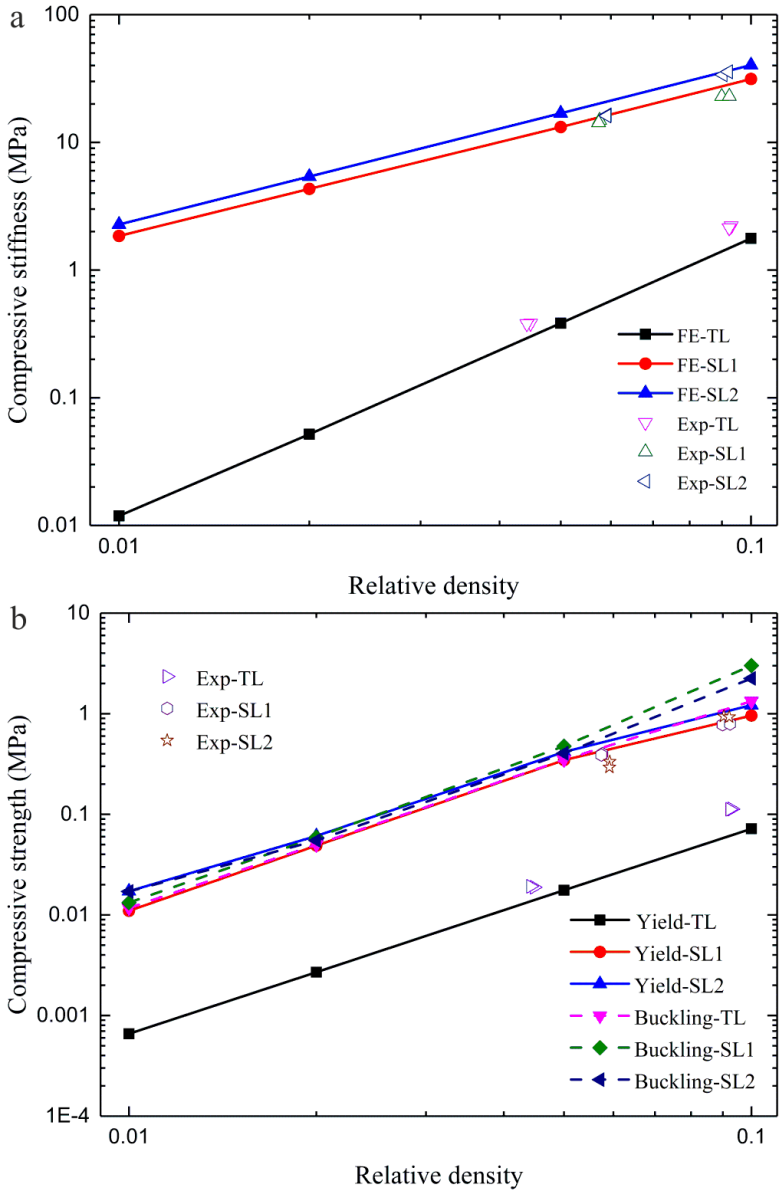


Figure II.6: Evolution of compressive stiffness (a) and strength (b) as obtained from experiments and finite element simulations as a function of relative density for TL, SL1 and SL2 metamaterials.

We compared experimental results to numerical simulations and found them to be in good agreement (see Figure II.6). With an increase in relative density, the compressive stiffness and strength of all three configurations increase. SL2 has the largest stiffness. The elastic modulus of TL is always much less than that of SL. When the relative density is smaller than 5%, SL1 possesses the highest compressive strength. At high relative densities, the compressive strength of SL2 is in contrast significantly higher than that of SL1.

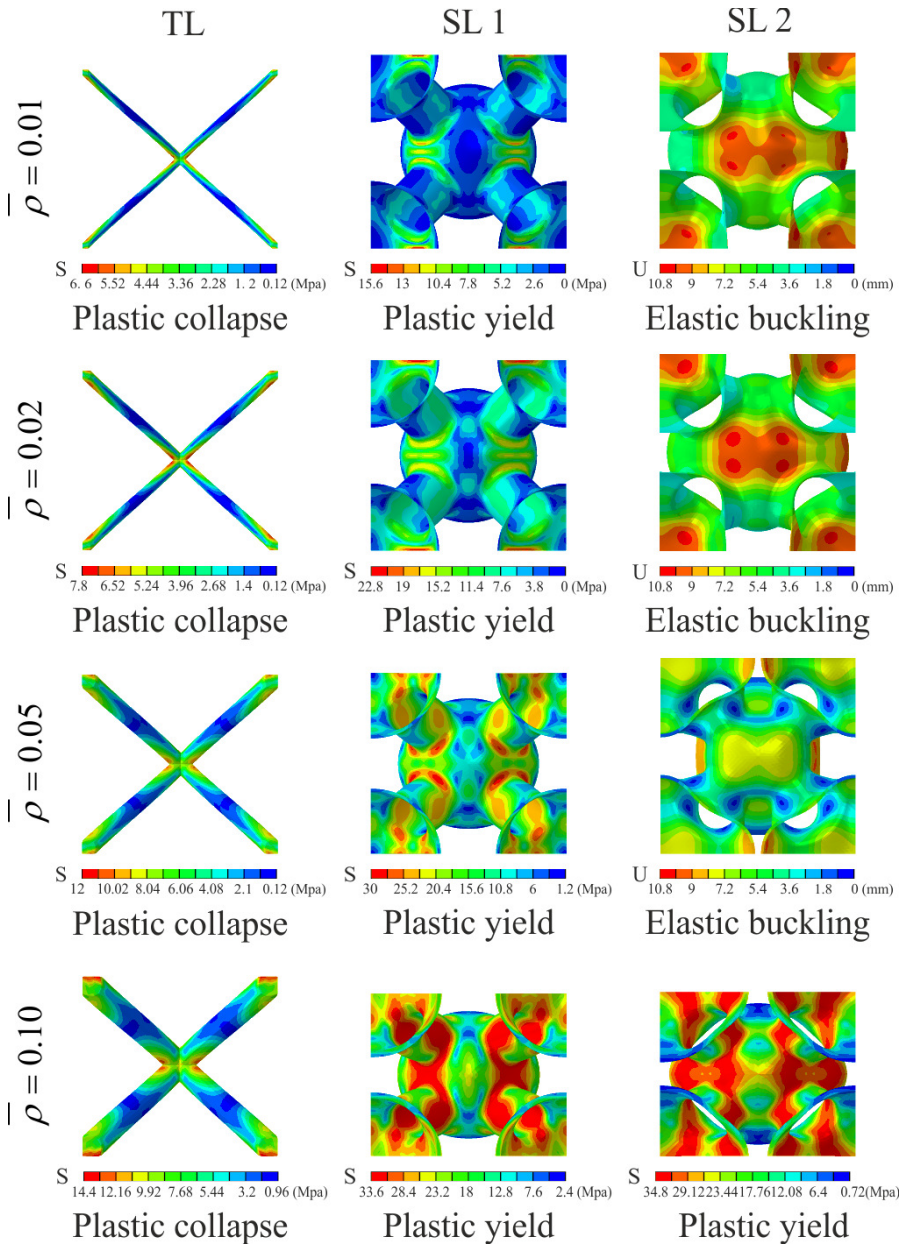


Figure II.7: Failure mode of TL, SL1 and SL2 metamaterials with relative densities ranging from 0.01 to 0.1 under uniaxial compressive loading.

Figure II.7 displays the failure modes of TL, SL1 and SL2 metamaterials with relative densities ranging from 0.01 to 0.1 under uniaxial compressive loading. SL metamaterials always fail by plastic collapse of the struts before the onset of elastic buckling. The strength of TL is always much less than that of SL1 and SL2 materials. The stress concentration is located at the connections of adjacent struts where plastic hinges occur. The appearance of plastic hinges can guarantee the stability of mechanical performance, but at the expense of reducing the structure capability. The failure of SL1 structures is dominated by plastic yield, not by

elastic buckling. At low relative densities, the SL1 structure possesses the highest compressive strength and the stress concentration is located near variable cross-section cylindrical shells. With a relative density increase, the range of stress concentration extends to shell struts. Different from TL and SL1 metamaterials, SL2 metamaterials fail by elastic buckling or plastic yield, as determined by the relative density. When the relative density is smaller than 5%, the buckling strength is close to the yield strength and stress concentration is always located at the middle areas of the ball shells. Spherical shells are too thin to resist local buckling and the failure of the SL2 metamaterial is dominated by local buckling of spherical shells. Note that in our simulations the elastic buckling strength and the yield strength of SL1 are very close to that of SL2 at low relative density. The strength of SL2 should be larger than that of SL1. However, SL2 structures are more sensitive to flaws, imperfections and boundary effects due to their structural characteristics, that is, the ratio of wall thickness and ball shell radius is too small. Hence, as compared to the SL1 material, the load bearing capacity of SL2 is good but not improved. However, at high relative density the compressive strength of SL2 is significantly higher than that of SL1, which is validated by the previous experiments. Stress concentration is located at most areas of spherical shells and cylinder strut shells. Of course, flaws, imperfections and boundary effects are also the most important factors, but they have less effect on compressive strength as the wall thickness increases. Moreover, the advantage of a large ratio of spherical radius to cylinder strut length is more obvious.

We also compared the effective stiffness and strength with other stretching-dominated lattice materials and other shellular materials [Nguyen 16, Valdevit 13, Bonatti 19b], as reported in Figure II.8. For a fair comparison between different constituent materials, we use the normalized elastic modulus $E/(\bar{\rho}E_S)$ and the normalized compressive stress $\sigma/(\bar{\rho}\sigma_Y)$. SL metamaterials have higher relative compressive stiffness and strength (see Figure II.8). For relative density of about 10%, SL2 metamaterial has a relative strength about 5.4 times and a relative elastic modulus about 2.4 times larger than those of octet lattice material [Meza 17], which makes it a noteworthy alternative to support structures.

Finally, the specific energy absorption (SEA), a crucial characteristics of any shock absorber, is defined as the work performed under uniaxial compression up to a strain of -0.6 per gram of mass by

$$\mathrm{SEA} = \frac{V\int_0^{0.6}\sigma \mathrm{d}\epsilon}{M}. \tag{II.9}$$

The SEA is obtained experimentally from compressive stress-strain curves (see Fig. 3). At low relative density, the SEA of the SL1 metamaterial is almost 4 times larger than the SEA of the BCC lattice material and is slightly larger than the SEA of the SL2 metamaterial. When the relative density is about 9%, the SL2 metamaterial has a SEA nearly 3.56 times as large as the SEA of the BCC metamaterial and nearly 1.26 times as large as the SEA of the SL1 metamaterial. In absolute numbers for the low density of 5% we get $\mathrm{SEA_{TL}} = 0.61$ J/g, $\mathrm{SEA_{SL1}} = 2.71$ J/g and $\mathrm{SEA_{SL2}} = 2.61$ J/g and for the high density of 10% we get $\mathrm{SEA_{TL}} =$

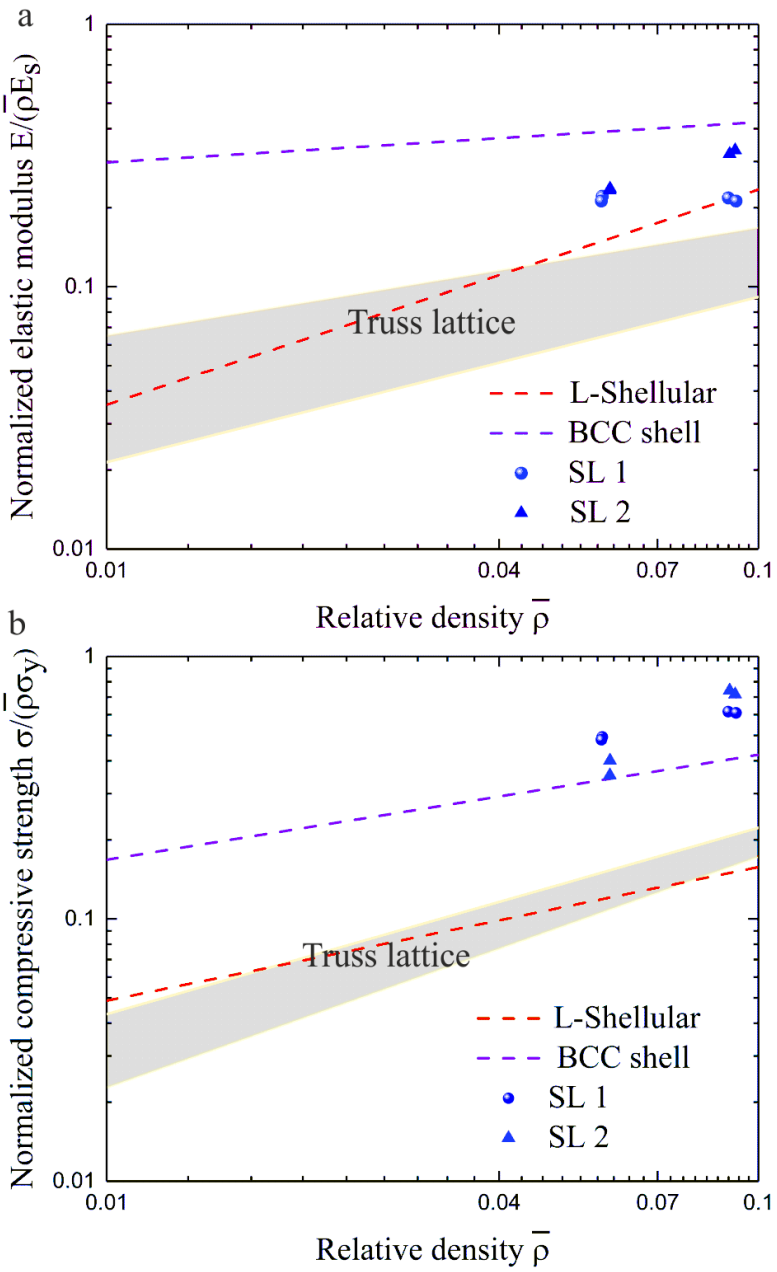


Figure II.8: Comparison of normalized (a) elastic modulus and (b) strength between our SL samples and other stretching-dominated lattice and shellular materials, including octet truss-lattice [Meza 17], L-shellular [Nguyen 16], and BCC shellular [Bonatti 19b] metamaterials.

0.47 J/g, $SEA_{SL1} = 4.15$ J/g and $SEA_{SL2} = 5.23$ J/g. Lately, a paper by Bonatti *et al.* [40] reported results similar to ours, but for metallic structures. In comparison, we achieve a lower normalized elastic modulus (normalization is to the constituent material in order to enable a fair comparison of the designed metamaterials) but a larger normalized compressive strength with much cheaper fabrication technique and constituent materials.

## II.6 Conclusions

As a conclusion, we have designed a stretching-dominated mechanical metamaterial that are ultrastiff, ultrastrong, and that exhibit high specific energy absorption properties at low relative density. These stretching-dominated mechanical metamaterials can absorb large energies while at the same time retaining a low density. They are promising candidates for applications to shock absorption and as a model for closed-cell crystalline foams.

# Chapter III

# Closed tubular mechanical metamaterial as lightweight load-bearing structure and energy absorber

## III.1 Introduction

As defined by Zok et al., the simple-cubic (SC) lattice, together with the BCC lattice and the FCC lattice, constitute an elementary cubic truss family [Zok 16]. In theory, the SC lattice should belong to the bending-dominated family. In fact, the SC lattice possesses the highest Young's modulus but the lowest shear modulus along the [100] direction within the elementary cubic family. High anisotropic mechanical properties and low resistance to buckling loading and shearing loading limit its application to energy absorption. A recent work on elastically-isotropic elementary cubic lattices has shown that tailoring the hollow beam could reduce anisotropy, however, at the expense of stiffness [Tancogne-Dejean 18b].

In this chapter, a new class of SC lattice composed of closed tubes is proposed for energy absorption and load-bearing. Finite element simulations are performed to investigate the elastic moduli and the collapse strength of the proposed material for relative density ranging from 0.1 to 0.5. Numerical results show that the closed tubes lead to higher mechanical properties, reduced anisotropy, and significantly enhanced resistance to shearing and buckling loading, without affecting the stiffness. Uniaxial compressive experiments on micro lattices fabricated by two-photon lithography show that the designed metamaterial outperforms truss and shellular cubic metamaterials of the same relative density.

## III.2 Closed tubular mechanical metamaterial design

For 3D lightweight load-bearing and energy absorbing material design, a crucial aspect is to make the best use of every part of the structure. Obviously, in the absence of weight constraints, the ideal candidate would be the homogeneous solid itself. However, when aiming at the design of a lightweight structure, one has to decrease the volume and thus to remove material or to create inner holes. Structural design therefore becomes the real playground for optimization.

Under uniaxial compression, a lightweight 2D SC frame generally exhibits a decreasing post-buckling response following the initial linear regime valid for small displacements, as depicted in Figure III.1a and b. Only the vertical strut supports loading, which is unreasonable from the design point of view. The mechanical behavior changes significantly when the plain struts are replaced with a closed tube. The force–displacement curves suggest that the tube possesses a slightly larger elastic stiffness but mostly a much more stable nonlinear response. This may be attributed to the fact that the sides of the cylinder tube provide additional support under loading and resist the buckling strength, in contrast to struts.

This design idea also applies to the 3D case. Figure III.1c defines the relevant geometrical parameters. For a solid cylindrical strut of length $L$, the cross-section is circular with a constant diameter $d$. For a closed cylindrical tube of length $L$

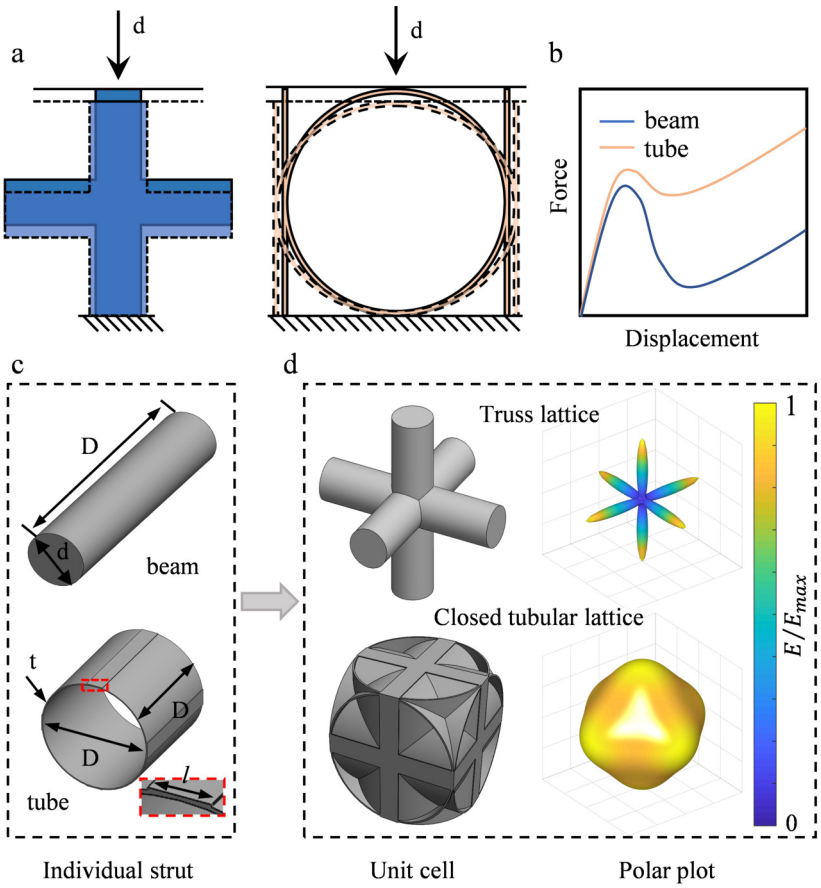


Figure III.1: Design concepts for tubular lattices. (a) Uniaxial compression mechanism for two dimensional simple cubic lattices composed of either solid beams or closed tubes. (b) Schematic force–displacement curves of a single unit cell show that the tubular lattice always exhibits higher elastic response and more stable nonlinear response compared to a truss lattice of the same relative density. Geometrical parameters for (c) individual struts (either beam or tube) and (d) the corresponding representative unit cell of an assembly. Polar plots depict the normalized Young's modulus as a function of the loading direction.

and diameter $D$, the thickness $t$ allows controlling the relative density. The unit cells are shown in Figure III.1d. The unit cell for the truss lattice is composed of three intersecting struts. The unit cell for the tubular lattice is also composed of three intersecting tubes, but to avoid vanishing surface contacts between adjacent unit cells, a cuboid with constant length $l$ and thickness $t$ is added, with $l = 0.15D$. The relative density $\rho^*$ is defined as the ratio of the actual volume to the volume of the cubic unit cell and can be easily obtained via a 3D CAD software.

The anisotropy of lattice materials is a very important property. An energy absorbing material is indeed expected to display a similar mechanical behavior for all loading directions or at least to have no obvious weak directions, to avoid stress shielding. For example, from the polar plots in Fig. III.1D we find that the

SC truss lattice possesses a high stiffness in the principal directions but a much lower stiffness in all other directions. The SC tubular lattice is also, of course, anisotropic. Its anisotropy, however, is significantly reduced from $E_{\max}/E_{\min} = 14.36$ down to $E_{\max}/E_{\min} = 1.25$ compared to the truss lattice.

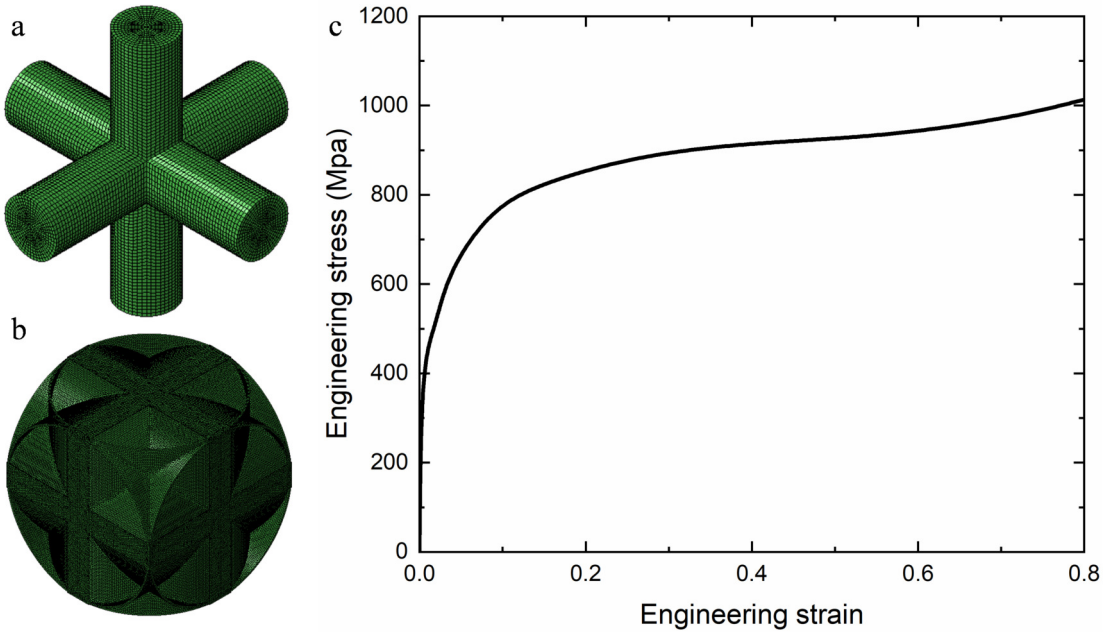


Figure III.2: Mesh model for (a) truss and (b) closed tubular lattices at a relative density of 0.1. (c) Engineering stress-strain curves for 316L stainless steel adopted in simulations.

## III.3 Numerical simulation

To identify the elastic moduli and yield strength of the SC lattice metamaterials, a series of unit cell models with relative density ranging from 0.1 to 0.5 were built using commercial software Abaqus. Truss lattice lattices are meshed with first-order solid elements (type C3D8R) using at least seven elements along the radius of a beam. Due to their complex geometry, closed tubular lattices are built using quadratic tetrahedral elements (type C3D10). To ensure computation accuracy, we employ meshes with 80,784 elements for the truss lattice and 670,320 elements for the closed tubular lattice, as illustrated in Figure III.2 (a and b). For the same models with a relative density larger than 0.1, twice coarser meshes are adopted.

The basis material used in simulations is stainless steel 316L. Such a homogeneous solid is modeled using an isotropic hardening elasto-plastic material model with a Young's modulus of 210 Gpa and a Poisson's ratio of 0.3. The 0.2% offset yield strength is assumed to be 418 Mpa. The detailed stress-strain response for

stainless steel is depicted in Figure III.2 c. For all models, the edge length of unit cells is fixed to 200 $\mu m$. The corresponding strut radius for the truss lattice and the wall thickness for the closed tubular lattice change with relative density. Periodic boundary conditions are applied by matching points for each pair of parallel unit-cell boundary surfaces with linear constraint equations.

Elastic simulations considering a small strain under uniaxial compression, pure shearing loading and hydrostatic compression along principal direction are conducted to extract Young's modulus, shear modulus and bulk modulus, respectively. Additional compression simulations up to a strain of $-0.01$ along 21 directions are performed to find extreme values for the yield strength of cubic symmetric lattices. The initial yield strength is defined by the axial stress at the point where the permanent strain is 0.2%.

### III.3.1 Elastic mechanical properties

In the linear case, the elastic anisotropy of cubic lattices is often quantified by Zener's ratio

$$Z = G\frac{9K - E}{3KE}, \tag{III.1}$$

where $G$, $K$ and $E$ are respectively the shear modulus, the bulk modulus and Young's modulus of the lattice material in a principal direction. Elastic isotropy is achieved only when $Z = 1$. Figure III.3a illustrates the dependence of Zener's ratio with relative density for both the closed tubular lattice and the truss lattice; at a relative density of 0.1, $Z = 0.76$ for the former and $Z = 0.05$ for the latter. For both lattices, as the relative density increases, Zener's ratio increases and would converge to 1 in the limit of the plain material. The influence of overlapping nodes as well as bending and shearing coupling deformation on anisotropy become more important as the relative density decreases, thus playing against lightweight lattices. It can also be observed that Zener's ratio for the closed tubular lattice is always far larger than for the truss lattice. As a whole, the presence of the closed tube largely reduces the anisotropy of the SC lattice by redistributing the stress in a more uniform manner.

For cubic lattices, the directional dependence of Young's modulus can be obtained as [Meyers 08]

$$\frac{1}{E_{ijk}} = \frac{1}{E} - \frac{Z-1}{2G}\left(l_{i1}^2 l_{j2}^2 + l_{j2}^2 l_{k3}^2 + l_{i1}^2 l_{k3}^2\right), \tag{III.2}$$

where $E_{ijk}$ is Young's modulus in the $[ijk]$ direction, and $l_{i1}$, $l_{j2}$ and $l_{k3}$ stand for the direction cosines of the $[ijk]$ direction vector with respect to the principal axes. Figure III.3b shows the evolution of the maximum and the minimum Young's modulus as a function of the relative density, for both lattices. Hereafter, the effective mechanical properties of the metamaterial are normalized to those of the basis material and to the relative density, to allow a fair comparison. Both SC lattices exhibit their stiffest and softest uniaxial Young's modulus respectively along directions [100] and [111]. The stiffness of the closed tubular lattice is always

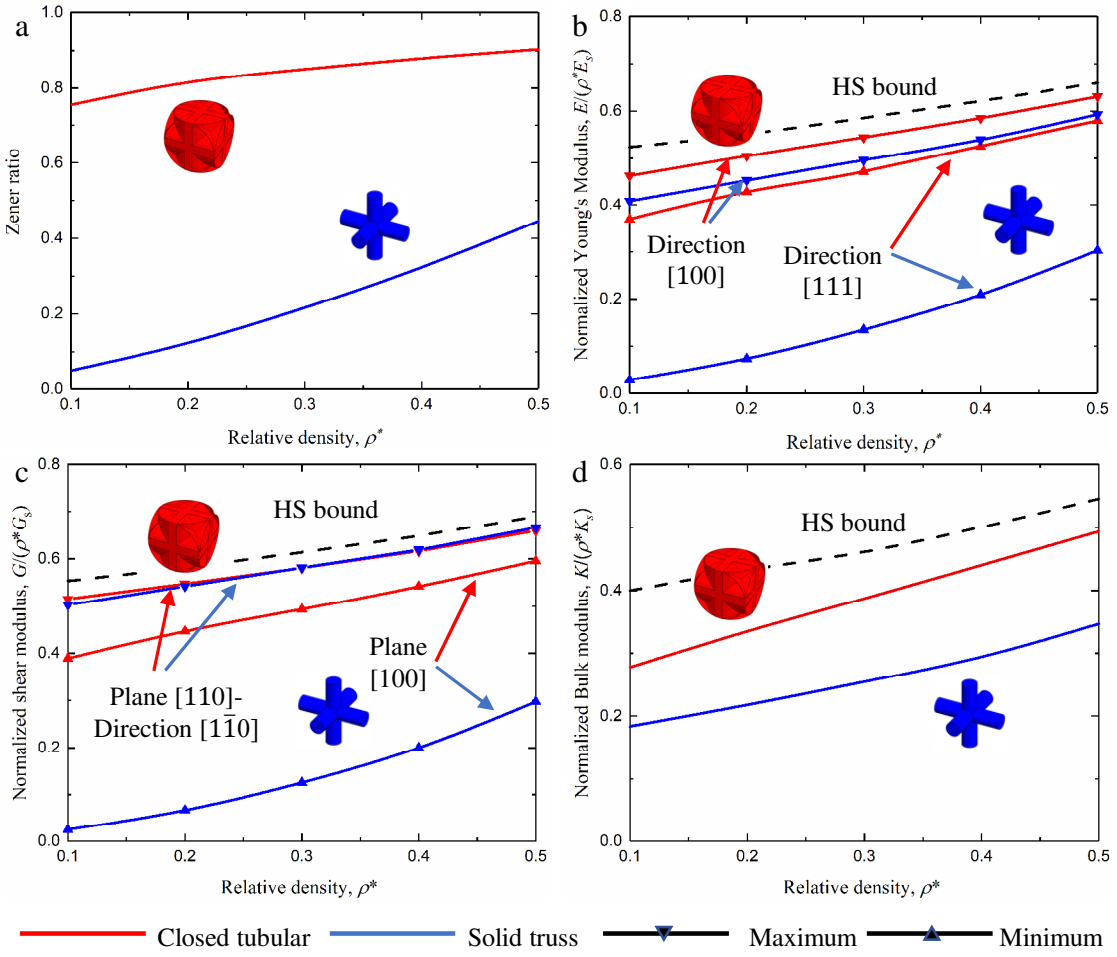


Figure III.3: Comparison of the elastic properties of simple-cubic closed tubular lattices and of truss lattices, as obtained from numerical simulation. (a-d) Evolution as a function of relative density of Zener's ratio, of the normalized Young's modulus, of the normalized shear modulus, and of the normalized bulk modulus.

larger than that of the truss lattice, regardless of the loading direction. The choice of loading direction has little influence on the stiffness of the closed tubular lattice, since it is always stretching dominated, while the opposite observation is true for the truss lattice: the stiffness of the truss lattice is stretching-dominated for [100] direction loading and bending-dominated for [111] direction loading. At a relative density of 0.1, the normalized stiffness of the truss lattice has a maximum of 0.41 and a minimum of 0.02. At the same relative density, the normalized stiffness of the closed tubular lattice is 1.12 times larger at the maximum and 18.5 times larger at the minimum. The normalized stiffness of the closed tubular lattice, whether in the maximum or the minimum direction, is very close to the theoretical limit for a plain solid. At a relative density of 0.5, the maximum and minimum values for the closed tubular lattice attain respectively almost 96% and 89% of the Hashin-Shtrikman(HS) bound.

The definition of the shear modulus requires to consider both the normal to the shear plane and the direction of shear. It is practical to consider a transformed coordinate system in which axis 3 is parallel to the normal of the shear plane and axis 2 is the direction of shear. The shear modulus can then be determined as [Knowles 15]

$$G_{ijk} = G\left(1 + 2\left(\frac{1}{Z} - 1\right)\left(a_{31}^2 a_{21}^2 + a_{32}^2 a_{22}^2 + a_{33}^2 a_{23}^2\right)\right), \tag{III.3}$$

where the $a_{ij}$ are direction cosines specifying the angle between the $i$th axis of the transformed reference frame and the $j$th axis of the material reference frame. Figure III.3c illustrates the scaling of the maximum and the minimum of the shear modulus as a function of the relative density, for both the closed tubular lattice and the truss lattice. The shear modulus generally increases with the relative density. Both lattices have their softest elastic shear modulus when either the shear direction is [100] or the shear plane is {100}. The lower limit for the closed tubular lattice is much larger than for the truss lattice. At a relative density of 0.1, the closed tubular lattice possesses a normalized shear modulus of about 0.39, almost 15.6 times as much as for the solid truss lattice, and almost reaches 71% of the HS bound. The stiffest elastic shear modulus is found on plane {100} when the shear direction is $[\bar{1}00]$, almost irrelevant of the choice of strut element. Both lattices have nearly the same extreme elastic shear response and attain about 93% of the HS bound even at relative densities as low as 0.1.

Figure III.3d depicts the variation of the bulk modulus as a function of the relative density for the closed tubular lattice and the truss lattice. The bulk modulus increases with the relative density for both lattices. It is noted that the closed tubular lattice exhibits a larger bulk modulus than the truss lattice; it is at least 1.5 times larger at a relative density of 0.1. Moreover, the closed tubular lattice reaches the HS bound faster than the truss lattice.

### III.3.2 Yield strength

Figure III.4 and Figure III.5 compare the computed compressive responses of the truss lattice and the closed tubular lattice. While not isotropic, the closed tubular lattice exhibits a similar linear elastic behavior along the three high-symmetry directions for all relative densities considered. In contrast, the linear elastic response of the truss lattice is highly dependent on the loading direction, especially at low relative density. With regard to the subsequent nonlinear region of the compressive response, the closed tubular lattice still offers distinctive advantages over the truss lattice. The Von Mises stress distributions in Figure III.4b-g clearly indicate that stress in the closed tubular lattice is distributed much more uniformly than in the truss lattice. As a result, the closed tubular lattice makes better use of its components than the truss lattice regardless of the loading direction.

The evolution of the relative yield strength as a function of relative density is summarized in Figure III.6. For the truss lattice, the strongest direction is [100], whereas the weakest direction is [110]. The yield strength distributions

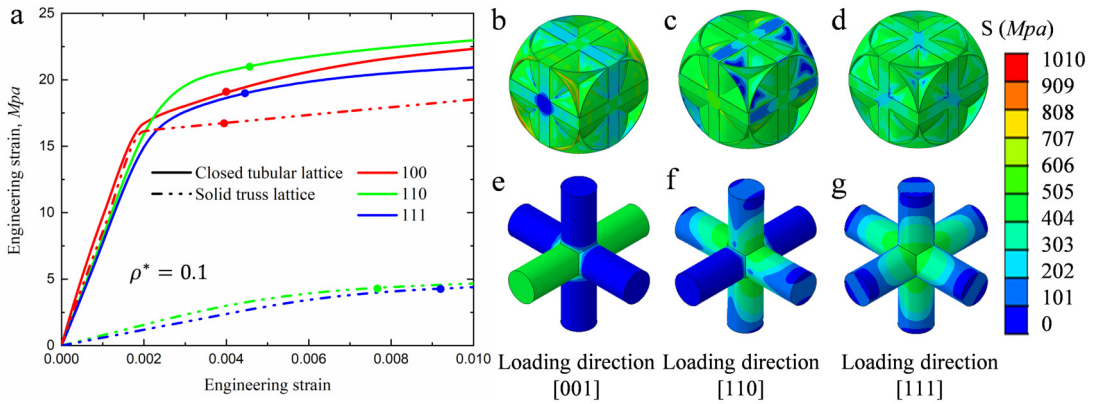


Figure III.4: (a) Engineering stress-strain curves for SC truss and closed tubular lattices at a relative density of 0.1, under uniaxial compression along directions [100], [110] and [111]. (b-g) Corresponding contour plots of the Von Mises stress in closed tubular and truss lattices at a strain of 0.01.

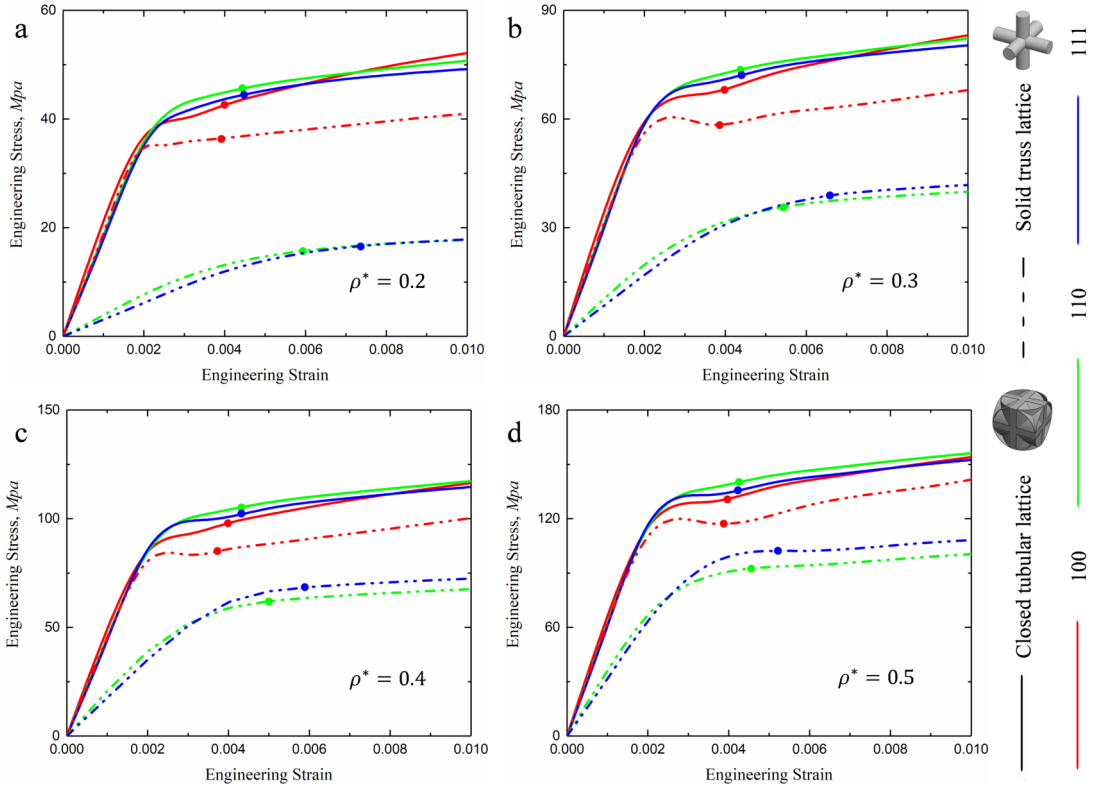


Figure III.5: (a-d) Compressive response of truss lattices and closed tubular lattices, with the relative density ranging from 0.2 to 0.5.

in the closed tubular lattice with relative densities of 0.1 and 0.2 are presented in Figure III.6(c,d). The maximum and minimum values are respectively found around directions [53,10,0] (as can be identified from the polar plot) and [100].

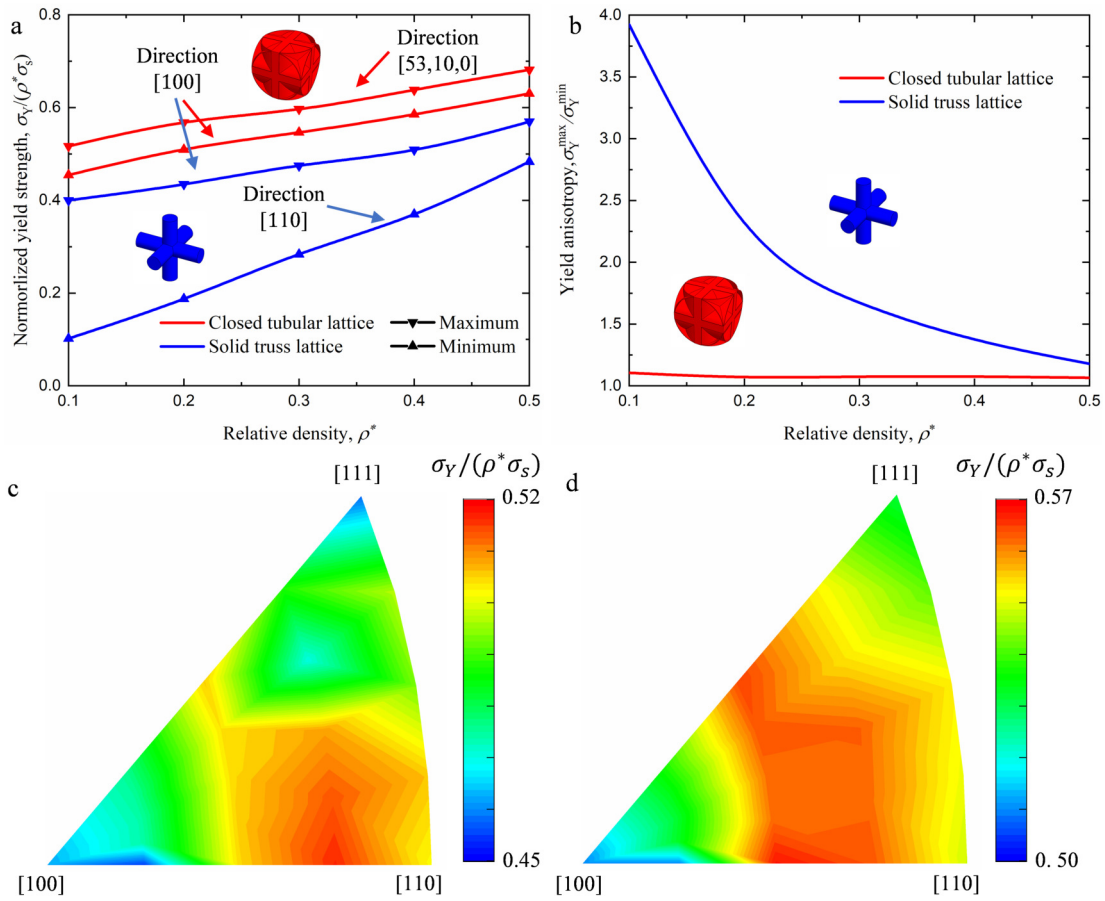


Figure III.6: (a) Normalized yield strength and (b) yield anisotropy of closed tubular and truss lattices as a function of relative density. Polar figures for yield strength distribution of the closed tubular lattice are shown with relative densities (c) 0.1 and (d) 0.2. Similar trends are observed at higher relative densities.

The yield strength of the closed tubular lattice is significantly larger than that of the truss lattice. Even in the worst case, when the loading direction is [100], the closed tubular lattice is stronger than the truss lattice. Figure III.6b displays the anisotropy of the yield strength. The relative density has little effect on the yield anisotropy of the closed tubular lattice: the yield strength ratio $\sigma_Y^{\max}/\sigma_Y^{\min}$ is almost constant and close to 1. In contrast, the truss lattice possesses a much higher yield anisotropy. At a relative density of 0.1, the yield strength ratio $\sigma_Y^{\max}/\sigma_Y^{\min} \approx 4$. Anisotropy decreases as the relative density increases.

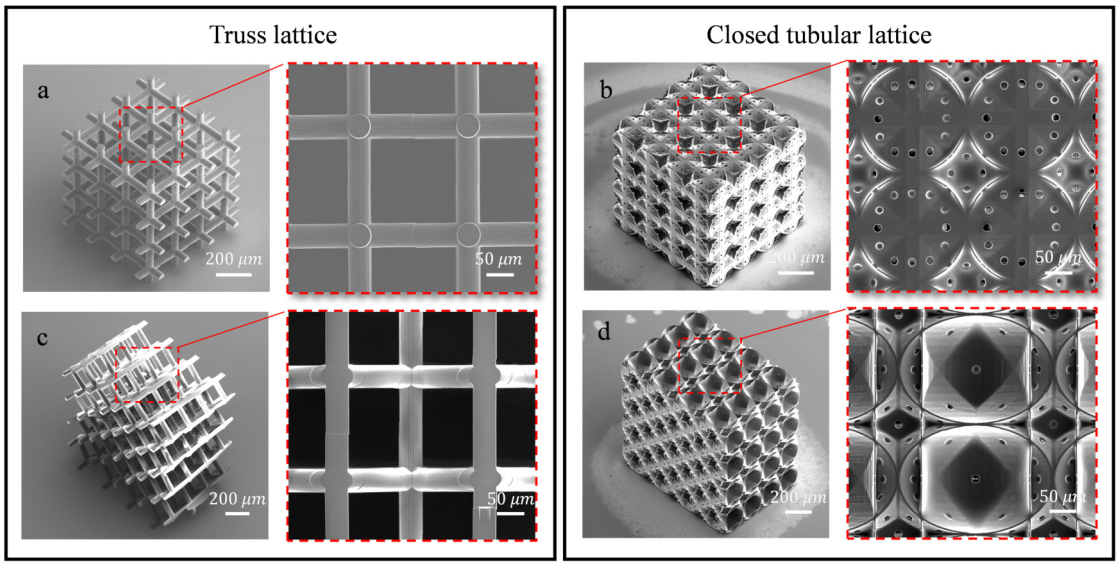


Figure III.7: SEM images of simple-cubic polymeric samples fabricated via 3D printing technology. Isometric views and zoom-in views are shown for truss and closed tubular lattices with relative density 0.1. (A) [100] truss lattice and (B) [100] closed tubular lattice. (C) [110] truss lattice and (D) [110] closed tubular lattice.

## III.4 Experiment

Polymeric samples with 4×4×4 unit cells were fabricated from the 'IPS' resin, using a 3D commercial printing system (Photonic Professional GT, Nanoscribe GmbH, Germany) with a speed of 100 $mm/s$ and a laser power of 100 $mW$. Samples on top of fused silica substrates were developed via the polymerization of the liquid negative-tone photoresist. A subsequent 20 min PGMEA(1-methoxy-2-propanol acetate) bath is applied to remove the unexposed photoresist.

Two different configurations with relative densities 0.1 and 0.2 are considered in this work. For each configuration, two types of samples oriented along directions [100] and [110] were fabricated by dip-in DLW optical lithography in view of compression tests (see Figure III.7). All samples feature a unit cell length of 200 $\mu m$. For the SC truss lattice, relative densities of 0.1 and 0.2 are obtained respectively for a strut diameter of 44.3 $\mu m$ and 65 $\mu m$. For the SC closed tubular lattice, the tube thickness is respectively 2.3 $\mu m$ and 5.1 $\mu m$. As a note, circular holes of a diameter of 15 $\mu m$ had to be added at the center of each face to remove the unexposed resin.

To identify adequate geometrical parameters for those circular holes, a series of unit cell structures with the same unit cell length and thickness but different circular diameters were constructed (see Figure III.8). For the unit cell with smallest diameter $d = 9$ $\mu$m, the unexposed liquid resin is completely barricaded inside the structure and one can hardly identify the printed construction. When the diameter is increased to be 12 $\mu$m, the construction is observed to be improved;

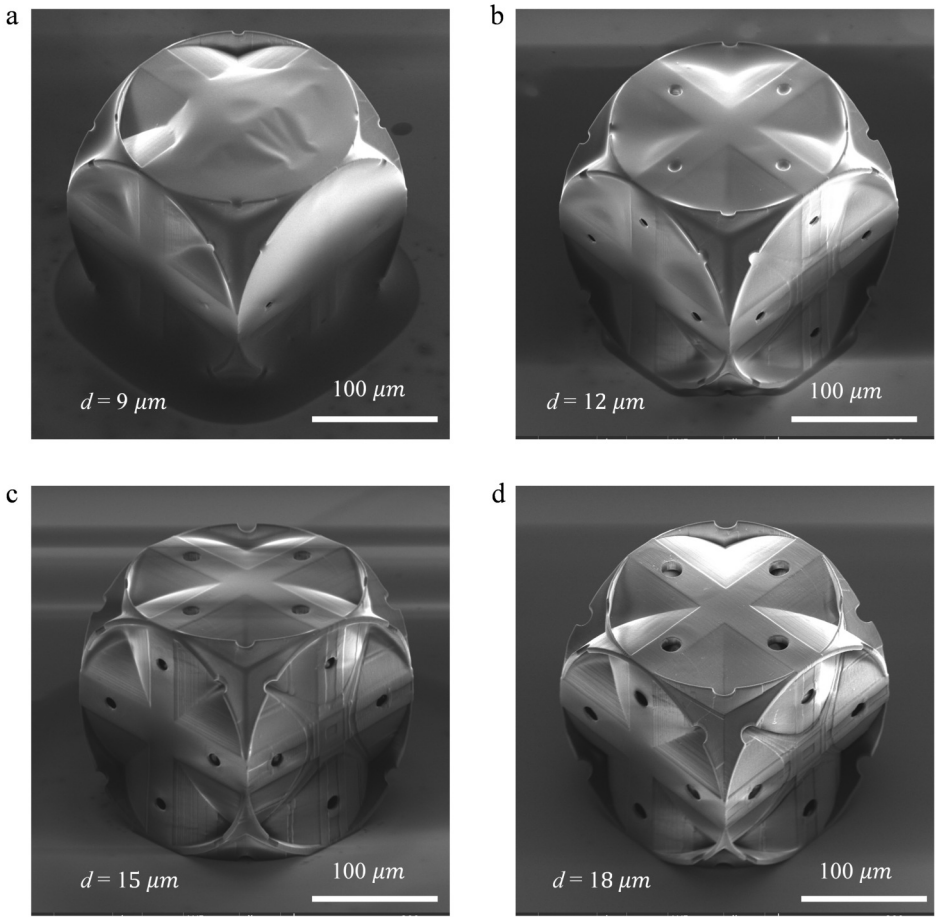


Figure III.8: SEM images of closed tubular unit-cell models fabricated with different hole diameters d. For unit cell with smaller diameter (a) d = 9 $\mu$ m and (b) d = 12 $\mu$m, the unexposed liquid resin is completely barricaded inside the structure and one can hardly identify the printed construction. In contrast, samples with diameters of (c)15 $\mu$m and (d) 18 $\mu$m are correctly printed.

however, some holes are still blocked by spurious polymerized resin remnants. In contrast, samples with diameters of 15 $\mu$m and 18 $\mu$m are correctly printed. To minimize the change in the mechanical properties of lattice, the smaller diameter $d = 15$ $\mu$m was chosen. Their effect of the holes on mechanical properties is almost insignificant, as detailed in the supplementary material (see Figure A.2).

Once fabricated, the polymeric microlattices were mechanically tested under uniaxial compression at a constant strain rate of $10^{-3}$ $s^{-1}$. Samples were placed between a fixed glass substrate and a flat loading device. The loading device equipped with an sensitive force sensor was driven by a stepping sensor and used to record the reacting force. The position obtained directly from the linear stage was only used to monitor the fatigue of the material. Front-view videos of samples were used to monitor the deformation of the lateral faces and hence to correct the load and displacement curves via an in-house digital image correlation

(DIC) algorithm. The Young's modulus was calculated based on the local axial strain measured from reference points at the central row of the unit cells (Figure III.9), and yield strengths were taken as the 0.2% offset strength of the engineering stress-strain curves. The local axial strain is calculated from expression $\varepsilon = \left| \frac{y_1^{'} + y_2^{'} + y_3^{'} + y_4^{'} - y_5^{'} - y_6^{'} - y_7^{'} - y_8^{'}}{y_1 + y_2 + y_3 + y_4 - y_5 - y_6 - y_7 - y_8} \right|$, where $y$ and $y^{'}$ stand for the original coordinates and coordinates after deformation.

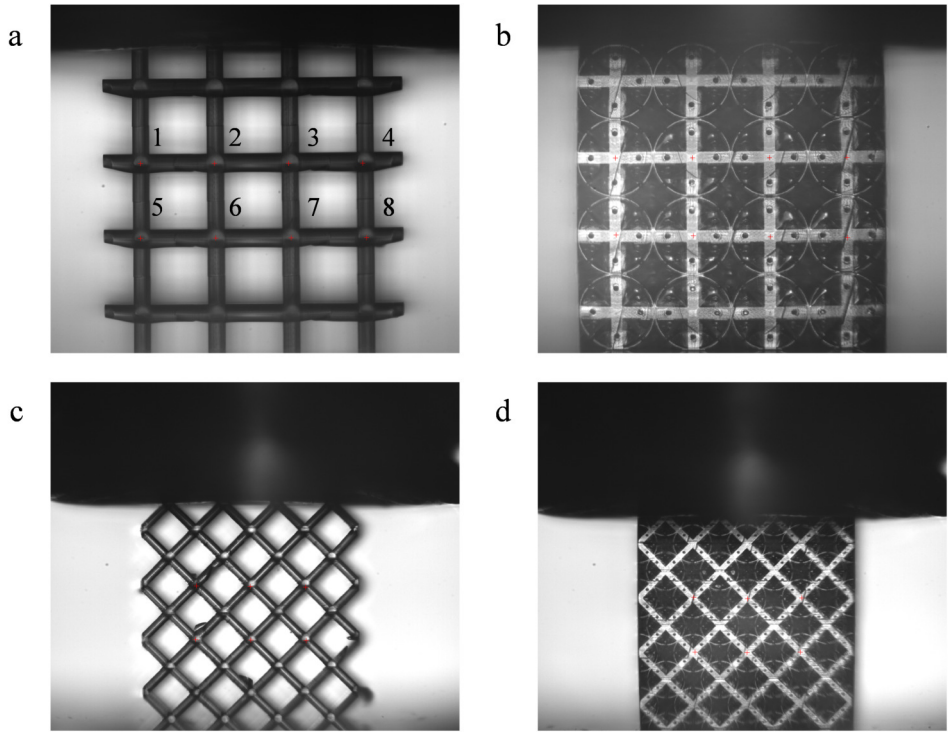


Figure III.9: Measurement of the average relative displacement of the center row of samples through digital image correlation technology.

## III.5 Results and discussion

Figure III.10 illustrates the result of compressive experiments. Experimental stress-strain curves at a relative density of 0.1 are shown in Figure III.10a. The [100] truss lattice samples exhibit an almost linear elastic response followed by a brittle fracture at a stress of about 3 $Mpa$. The peak stress is taken as the experimental yield strength $\varepsilon_Y$ in the following. The subsequent decrease of the response continues until the engineering strain reaches 0.15. At this point, the structure almost looses its loading capacity due to the catastrophic failure of sub-bottom layer struts (see Figure III.10 c). The following oscillations of stress are caused by layers contacting and collapsing one after the other. In contrast, the catastrophic collapse mode of the [110] truss lattice sample is greatly reduced, as

well as its compressive mechanical response. The brittle failure of struts along the diagonal direction is mainly affected by shearing forces rather than by nonlinear buckling (see Figure III.10 d).

In the case of the closed tubular lattice samples, the mechanical response and the deformation mechanisms are completely different. For both directions [100] and [110], a nearly stable nonlinear response and a progressive failure are observed during compression (see Figure III.10 e and f). Deformations are more uniform compared to the truss lattice and slight oscillations arise from local buckling of the thin tubes. Similar trends were observed for all samples with the higher relative density 0.2 (see the stress-strain curves in Figure III.10 b). The main difference is that truss lattice samples were completely crushed at an engineering strain of only 0.15. It may be attributed to the fact that struts with large diameters bear larger strength at low strain and are hence more sensitive to flaws and imperfections.

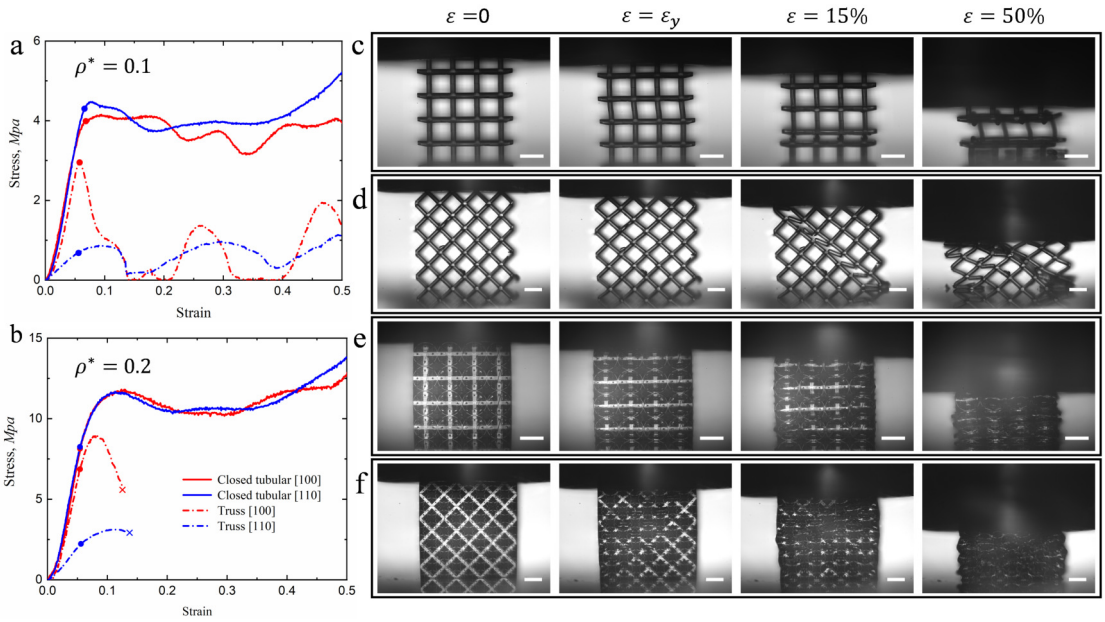


Figure III.10: Uniaxial compression experiments of SC [100] and [110] samples with different relative densities. Engineering stress-strain curves for the closed tubular and the truss lattices are shown for relative density (a) 0.1 and (b) 0.2. Photographs of the deformed samples during compression are shown for relative density 0.1 for (c) the [100] truss lattice, (d) the [110] truss lattice, (e) the [100] closed tubular lattice, and (f) the [110] closed tubular lattice. $\varepsilon_Y$ is the strain at the peak stress $\sigma_Y$, or the experimental yield strength. All scale-bars are 200 $\mu$m long.

Table III.1 summarizes the experimental values of Young's modulus, the yield strength and the specific energy absorption (SEA) of all test samples. At low relative density, Young's modulus and yield strength of the tubular lattice along the [100] direction are sightly larger than those of the truss lattice. For the [110] direction, however, they are respectively 8.05 times and 6.6 times larger. Experimental

values for the [110] direction are respectively 17 % smaller and 20 % larger than the simulated values. Differences may come from the limited number of unit cells which significantly reduces the elastic response of stretching-dominated materials, whereas it has limited influence on bending-dominated material. The opposite observation is true for the elastic-plastic phase. Samples at higher relative density show similar trends. The SEA is defined as the work performed under uniaxial compression up to a strain of 0.5 per gram of mass as SEA $= \left(V \int_0^{0.5} \sigma d\varepsilon\right) / M$. At low relative density, the SEA for the closed tubular lattice along the [100] direction and the [110] direction is respectively 4.45 times and 6.14 times larger than for the truss lattice. For a relative density of 0.2, absolute values SEA $= 25.13\ J/g$ and $25.73\ J/g$ are found respectively for directions [100] and [110].

| Specimens | Relative density | Direction | E (MPa) | $\sigma_Y$(MPa) | SEA (J/g) |
|---|---|---|---|---|---|
| Truss lattice | 0.1 | [100] | 97.76 | 2.95 | 4 |
| | | [110] | 13.93 | 0.65 | 3.13 |
| Tubular lattice | 0.1 | [100] | 112.98 | 3.99 | 17.79 |
| | | [110] | 111.13 | 4.3 | 19.21 |
| Truss lattice | 0.2 | [100] | 227.35 | 6.86 | |
| | | [110] | 48.77 | 2.22 | |
| Tubular lattice | 0.2 | [100] | 249 | 8.13 | 25.13 |
| | | [110] | 270 | 8.24 | 25.73 |

Table III.1: Mechanical data absorption of the tested samples, including Young's modulus, yield strength and specific energy, for different configurations and different relative densities.

## III.6 Comparison with other shellular and tubular lattices

Figure III.11 shows the dependence versus relative density of the average normalized Young's modulus and yield strength for the closed tubular lattice, compared with competing isotropic tubular lattices [Tancogne-Dejean 18b] and shellular lattices [Bonatti 19c]. It is interesting to observe that both normalized elastic modulus and yield strength of the closed tubular lattice scale almost linearly with relative density. They can be approximated by the linear functions $E/(E_s\rho^*) = 0.365 + 0.475\rho^*$ and $\sigma/(\sigma_s\rho^*) = 0.4 + 0.48\rho^*$. Both elastic modulus and yield strength are significantly larger than in the case of isotropic tubular lattices and shellular lattices, with a maximum advantage of 28% in stiffness and of 53% in strength at a relative density of 0.1. Concurrently, the modulus and strength of the SC closed tubular lattice reach respectively about 80% and 67% of their respective HS bound. These values become closer to the HS bound as the rel-

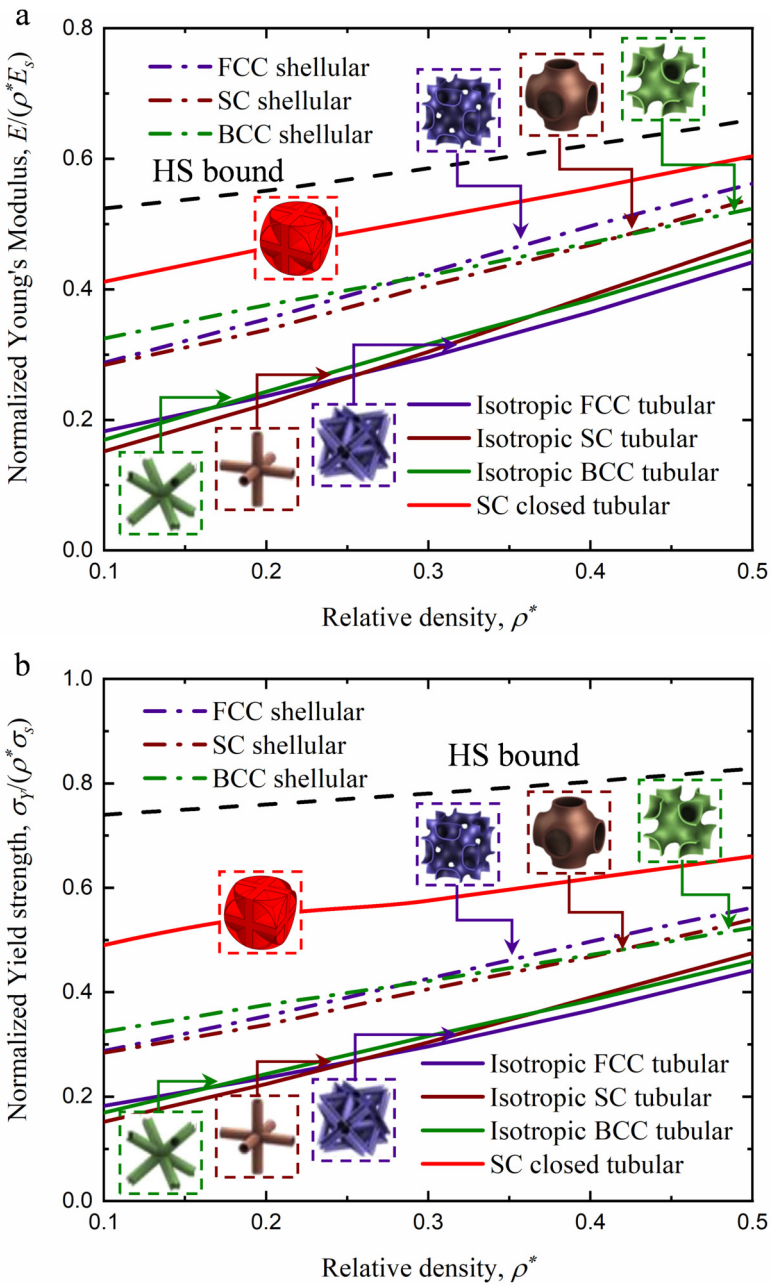


Figure III.11: Comparison of the mechanical properties of shellular and tubular lattices versus relative density. For a fair comparison, the average normalized (A) Young's modulus and (B) the yield strength of SC closed form tubular and other typical counterparts [Tancogne-Dejean 18b, Bonatti 19c] are shown.

ative density increases. When the relative density is as large as 0.5, modulus and strength almost attain 92% and 81% of their respective HS bound. As a whole, the combination of limited loading direction dependence, high specific stiffness,

strength and irregular stable post-yield response make the closed tubular lattice a promising candidate for applications to static compression and dynamic shock absorption.

## III.7 Conclusions

Here, we have introduced a class of lightweight simple-cubic closed tubular lattice material possessing ultra-high specific stiffness, ultra-high specific yield strength and stable post-yield response. Compared to the most stiff and strong smooth shellular lattice and tubular lattice materials, for the same relative density, the gain in average stiffness and strength is respectively 28% and 53%. Experiments with samples fabricated by DLW optical lithography and simulations demonstrate that the replacement of solid struts with closed tubes largely reduces the elastic and the yield anisotropy of simple-cubic lattice materials. As a direct benefit of the incredibly stable mechanical response of cylindrical tubes, the resistance of the closed tubular lattice to buckling strength is further enhanced and recoverablity is foreseeable by further reducing the thickness of the shell. This work provides a feasible pathway for applications in lightweight design, loading support, and shocking absorption.

# Chapter IV

# 3D lightweight energy absorber with nearly nonlinear isotropic compressive response

## IV.1 Introduction

Recent attention has been focused on the elastic isotropic response of mechanical metamaterials. The most popular method for designing isotropic structural materials is to combine different anisotropic structures with proper proportion, that is, to enhance the weaker directions and limit the stronger directions. Gurtner et al. presented a new class of optimal and isotropic three-dimensional truss lattice material [Gurtner 14]. Tancogne et al. enriched the isotropic truss-lattice family using combinations of elastically-anisotropic elementary cubic truss lattice and changing the ratio of bending-to-axial stiffness of the constituent beams [Tancogne-Dejean 18b, Tancogne-Dejean 18c]. Lately, Bonatti et al. showed that a family of elastically-isotropic shell-lattice materials are always stiffer than optimal isotropic truss-lattices and approach the Hashin–Shtrikman bound at high relative densities [Bonatti 19a]. According to theoretical predictions, only closed-cell materials can attain the Hashin–Shtrikman upper bounds on isotropic mechanical properties, even at ultra low relative density [Christensen 86]. Numerically, Berger et al. identified a class of cubic-octet hybrid closed foams achieving the maximum isotropic stiffness [Berger 17]. By placing plates along the closest packed planes of crystal structures with cubic symmetry, Tancogne et al. presented a class of lightweight plate-lattices providing near isotropic yield strength together with elastic isotropy [Tancogne-Dejean 18a]. Crook et al. further introduced a class of plate nano-lattices that are the only materials to experimentally achieve the Hashin-Shtrikman and Suquet upper bounds for isotropic elastic stiffness and strength, respectively [Crook 20]. Similarly, by synthesizing $n+1$ sets of continuous plates in a transversely quasi-periodic manner, a dual family of quasi-periodic mechanical metamaterials with extreme maximum isotropic stiffness were achieved in theory [Wang 20].

As stretching-dominated materials with low relative density, the structural lattices mentioned above exhibit a higher specific stiffness and strength, but a less stable nonlinear response than those deforming in a bending-dominated mode [Deshpande 01b]. This is mainly because, in the initial elastic region, stretching-dominated materials store more strain energy during deformation than bending-dominated materials do. Under compression or tension, unlike bending-dominated materials, there exist micro-components in stretching dominated materials to support tensile forces and thus prevent displacements and rotations of nodes. When considering the nonlinear regime, things change drastically. In general, stretching-dominated materials lack stability toward large strain deformations and exhibit decreasing post-yield or post-buckling response. In contrast, bending-dominated materials make full use of plastic bending joints allowed for large deformations and provide relatively large and nearly constant stress in the nonlinear regime. Moreover, large mechanical properties always come with large nonlinear anisotropy [Gurtner 14, Tancogne-Dejean 18b, Tancogne-Dejean 18c, Tancogne-Dejean 18a]. Thus far and to best of our knowledge, however, few works have focused on designing isotropic nonlinear bending-dominated materials for energy absorption.

In this chapter, a class of isotropic bending dominated truss lattice materials, formed by replacing the central connecting node of the body-centered cubic (BCC) truss lattice [Ushijima 11, Gümrük 13, Tancogne-Dejean 18d] with a simple cubic (SC) truss lattice element, is proposed for absorbing energy. The effects of geometrical parameters on the effective mechanical properties are analyzed using numerical simulations and an analytical theory. Results show that the designed metamaterials exhibit not only isotropic stiffness, but also nearly isotropic nonlinear response. A series of samples with different relative densities are printed using two-photon polymerization in two different crystallographic directions, [100] and [110]. Uniaxial compression tests confirm the designed mechanical properties. Compared to BCC truss lattice materials, the designed metamaterials have a relative elastic modulus about twice as large and a specific energy absorption about 1.6 times as large.

## IV.2 Design of isotropic bending dominated lattice material

We first outline the general design procedure for combining the properties of BCC and SC truss lattices and achieving linear isotropy. As shown in Figure IV.1a and Figure IV.1b, both lattices at low density are highly anisotropic and Young's modulus varies by more than 2 or 3 orders of magnitude as a function of the loading direction. The directions along which maxima occur, however, are different: they are the principal axes of the cubic unit cell for the SC lattice and its diagonals for the BCC lattice. The BCC-SC truss lattice is then defined by replacing the central connection of the BCC lattice with an element of the SC lattice, as Figure IV.1c depicts. The impact of struts on the mechanical behavior is indeed highly direction dependent. In the [100] direction, the struts of the inner SC lattice element enhance the overall mechanical properties, whereas the struts of the BCC lattice provide rotational degrees of freedom and thus guarantee the steadiness of the post-collapse response. In the [111] direction, the converse is true: mechanical properties are enhanced by the BCC struts whereas the post-collapse response is stabilized by the SC struts. As a result, isotropy can be achieved by adjusting the geometrical dimensions of the struts, as we show next. The relevant dimensions are the ratio of inner cubic strut length to unit cell length $L_2/L$ and the ratio of strut diameter to unit cell length $D/L$. Both ratios influence the overall density of the structure $\bar{\rho}$. For compactness, we discuss their numerical values in the following, as obtained from numerical computations based on finite element analysis. A full analysis including analytical derivations is provided in the following section.

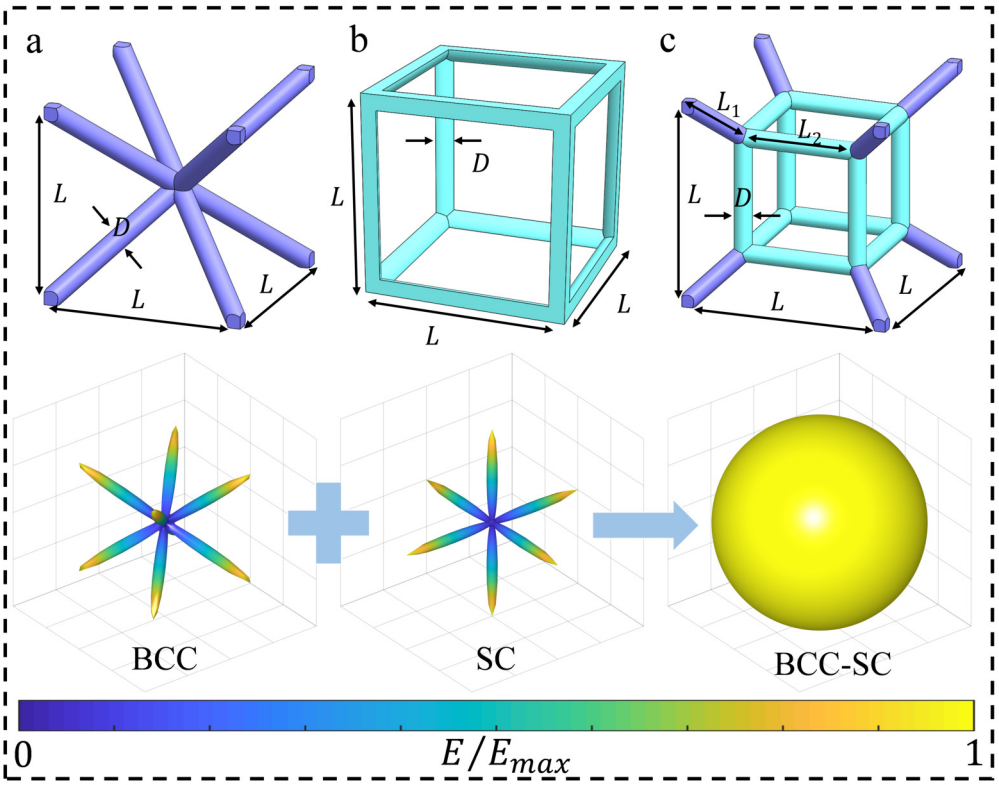


Figure IV.1: Representative unit cells of three cubic symetric truss lattice materials and corresponding Young's modulus as functions of the direction of loading:(a) BCC, (b) SC and (C) BCC-SC lattice.

### IV.2.1 Relative density

Figure IV.1a displays a non primitive cubic symmetric unit cell model of the body-centered cubic (BCC) lattice, composed of eight identical intersecting struts. Here, the struts are assumed to have uniform circular cross-section with constant radius $R$ and length $l = \sqrt{3}L/2$, with $L$ the side length of the cubic cell. For BCC truss lattice material, the relative density is defined as the ratio of the actual volume $V$ occupied by the lattice structure to the total volume of the unit cell,

$$\overline{\rho} = \frac{V}{L^3}. \tag{IV.1}$$

$V$ is obtained by integration as

$$V = 8\left(\pi R^2 l - 2\sqrt{6}R^3\right). \tag{IV.2}$$

Equation (IV.1) can therefore be written

$$\bar{\rho} = 3\sqrt{3}\pi\left(\frac{R}{l}\right)^2 - 18\sqrt{2}\left(\frac{R}{l}\right)^3. \tag{IV.3}$$

The above formula comprises two terms: the relative density of the ideal perfect struts minus the material overlap at nodes. The material overlap contribution increases with the aspect ratio $R/l$. For example, material overlap accounts for a correction by less than 5% when $R/l = 0.01$, but the correction reaches 50% for $R/l = 0.1$.

As shown in Figure IV.1c, the BCC-SC lattice is composed of 8 outer struts along diagonal directions with length $L_1$ and 12 inner struts along horizontal and vertical directions with length $L_2$. All struts have the same radius $R$. The volumes of outer and inner struts are

$$V_1 = \pi R^2 L_1 - C_1 R^3 \tag{IV.4}$$

and

$$V_2 = \pi R^2 L_2 - C_2 R^3. \tag{IV.5}$$

Constants $C_1$ and $C_2$ account for the overlap volume at nodes. Their numerical values were estimated using a 3D computer-aided design (CAD) software and are $C_1 = 3.35$ and $C_2 = 2.83$. The volume $V = 8V_1 + 12V_2$. The relative density of the BCC-SC lattice is given by

$$\bar{\rho} = 4\sqrt{3}\pi \left(\frac{R}{L}\right)^2 + (12 - 4\sqrt{3})\pi \left(\frac{R^2 L_2}{L^3}\right) - C \left(\frac{R}{L}\right)^3 \tag{IV.6}$$

with $L = L_2 + \frac{2}{\sqrt{3}} L_1$ the unit cell length. The numerical value of the last constant is $C = 8C_1 + 12C_2 = 60.73$. The relative density is determined by two independent variables, for instance the ratio of radius to unit cell length $R/L$ and the ratio of inner strut length to unit cell length $L_2/L$. One can use equally well $D/L$ and $L_2/L$ as the independent variables, with $D = 2R$ the diameter of the struts. For a given relative density, only one of the two variables needs to be adjusted to regulate the mechanical properties of the BCC-SC lattice.

### IV.2.2 Elastic behavior of BCC and BCC-SC lattices

As depicted in Figure A.3b, micro-struts have an irregular geometry at both ends and hence their mechanical behavior around nodes has to be quite complex. Strictly speaking, traditional theoretical analysis based on perfect beam theory is not applicable in such a case. To overcome the problem and for the sake of generality, irregular struts will be effectively replaced by perfect cylinders with the same volume. Thus, an effective strut length will be introduced instead of the original strut length. Table IV.1 gives the values of effective strut lengths for both BCC and BCC-SC lattices.

To facilitate the discussion, we remind that in a Cartesian coordinate system the constitutive law of linear elasticity relates the strain tensor $\varepsilon$ to the stress tensor $\sigma$ via a fourth-order symmetric elastic compliance tensor $S$, as

$$\varepsilon = \mathbf{S} : \sigma. \tag{IV.7}$$

| Topology | $l_e$ | $l_1$ | $l_2$ |
|---|---|---|---|
| BCC | $l - 2\sqrt{6}R/\pi$ | | |
| BCC-SC | | $L_1 - C_1 R/\pi$ | $L_2 - C_2 R/\pi$ |

Table IV.1: Effective strut length for BCC and BCC-SC lattices

For cubic-symmetric lattice materials, there are only three independent elements in the compliance matrix, i.e.

$$\boldsymbol{S} = \begin{bmatrix} 1/E & -\upsilon/E & -\upsilon/E & 0 & 0 & 0 \\ & 1/E & -\upsilon/E & 0 & 0 & 0 \\ & & 1/E & 0 & 0 & 0 \\ & & & 1/G & 0 & 0 \\ & \text{sym} & & & 1/G & 0 \\ & & & & & 1/G \end{bmatrix}. \tag{IV.8}$$

$E$, $G$ and $\upsilon$ are Young's modulus, the shear modulus and Poisson's ratio of the lattice material in principal directions. The principal axes, as shown in Figure A.3, are aligned with the unit cell edges. The detailed derivation of the above formulas for BCC and BCC-SC lattice are listed in section A.3.

### IV.2.3 Identification of isotropy

An analytical expression for Young's modulus along an arbitrary direction can be obtained as [Meyers 08]:

$$\frac{1}{E_{ijk}} = \frac{1}{E} - \frac{1}{2G}(Z-1)\left(l_{i1}^2 l_{j2}^2 + l_{j2}^2 l_{k3}^2 + l_{i1}^2 l_{k3}^2\right), \tag{IV.9}$$

where $[ijk]$ is the loading direction, and $l_{i1}$, $l_{j2}$ and $l_{k3}$ are direction cosines between the $[ijk]$ direction and the three principal directions. Zener's ratio $Z$, which is used to quantify the anisotropy of cubic crystals, is

$$Z = \frac{2(1+\upsilon)G}{E}. \tag{IV.10}$$

When $Z = 1$, a cubic material is exactly elastically isotropic. Finally, a combination of Equation IV.10 and simulations for three elastic moduli will help us to identify the suitable geometrical parameters for isotropy.

## IV.3 Numerical study

### IV.3.1 Simulation

To obtain the mechanical response of BCC and BCC-SC truss lattices, a series of unit cell models with different relative densities ranging from 1 to 20% were built using the commercial finite element software ABAQUS. To ensure the calculation accuracy, as shown in Figure IV.2, there exist at least fourteen three dimensional linear solid elements (type C3D8R) along the strut diameter direction. IP-S polymer is chosen as constituent material for simulations. The constituent material was modeled as an isotropic elasto-platic material with Young's modulus 3.6 GPa and Poisson's ratio 0.35. A 0.2% offset strength of 81 Mpa is taken as yield strength. The detailed engineering stress-strain curve shown in Figure IV.2is from a compression experiment on a micro-cube. For all models, the edge length of unit cells was fixed to 200 μm. The strut diameter was changed with the relative density, as well as the other geometrical parameters of the BCC-SC lattice. Periodic boundary conditions were applied by matching mesh nodes on opposite planes with linear constraint equations [Li 04]. Independent elastic moduli together with Poisson's ratio were extracted from uniaxial compression numerical experiments along the principal compression direction and along the two pure shear directions, respectively.

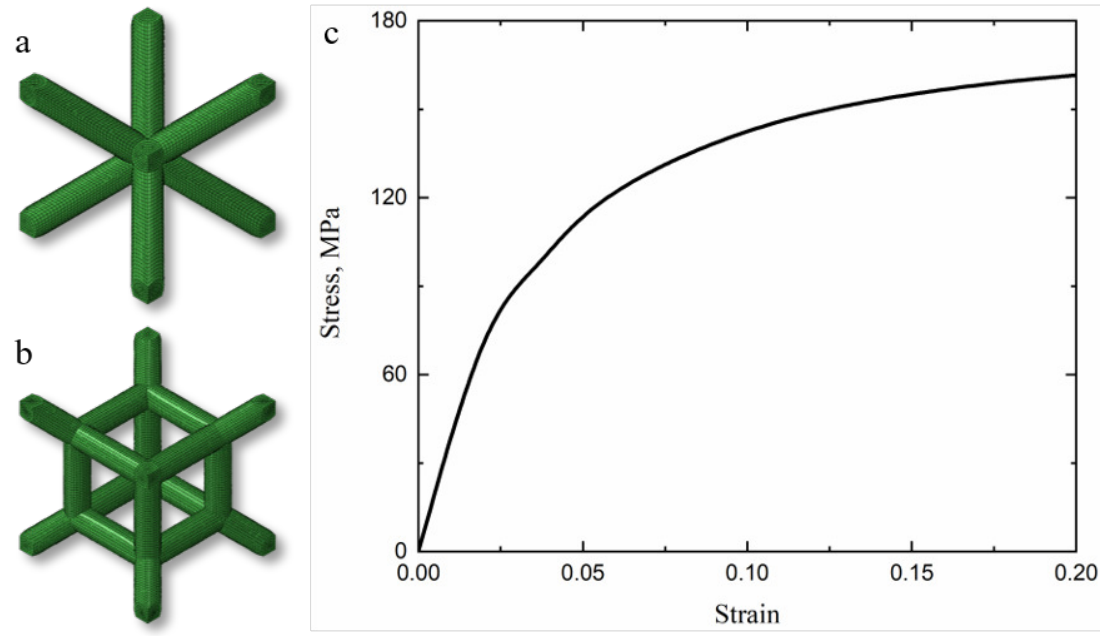


Figure IV.2: Representative numerical unit cell models for (a) BCC and (b) BCC-SC truss lattices. (c) The engineering stress-strain curve of material IP-S is obtained from compression experiments.

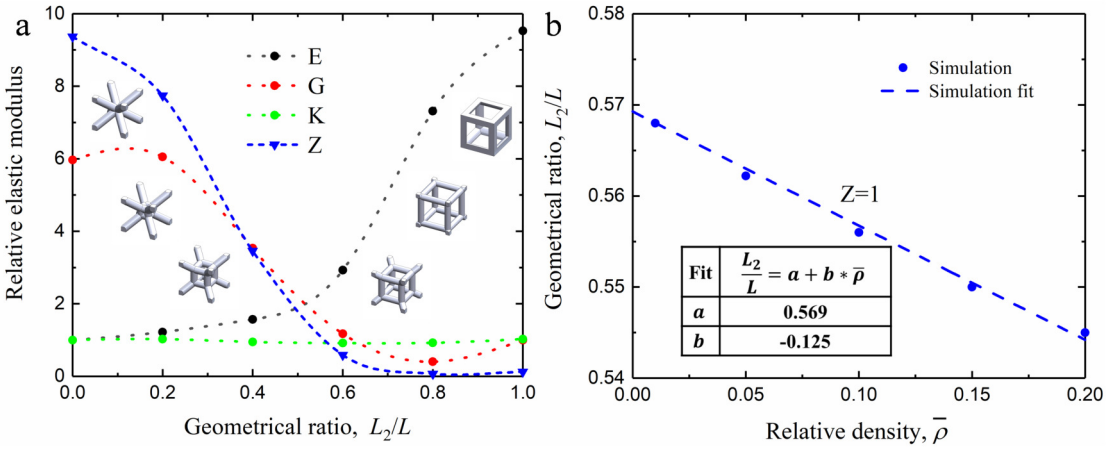


Figure IV.3: (a)Effect of geometrical parameter on elastic modulus and isotropy for a relative density of 0.2. (b) Evolution of ratio of inner strut length to unit cell length as a function of relative density obtained by simulation and curve fitting.

### IV.3.2 Effect of geometrical parameter on elastic properties

Figure IV.3(a) depicts variation of relative elastic moduli, including Young's modulus, shear modulus and bulk modulus, and Zener ratio for a relative density of 0.2. Here, Young's modulus and bulk modulus of BCC lattice and shear modulus of SC lattice are taken as original value, respectively. The inner strut length to unit cell length ratio $L_2/L$ have a strong influence on Young's modulus along principal direction. With an increase in $L_2/L$ , the [100] Young's modulus increase. Especially when $L_2/L$ is larger than 0.5, the Young's modulus growth of configuration accelerates. It increases more than 4 times, when $L_2/L$ increases from 0.5 to 1, from 2 to 9.5. While it also contributes to the transformation of the deformation behavior from bending-dominated to stretching-dominated mode. [100] shear modulus is shown to be more sensitive to $L_2/L$. When $L_2/L$ is smaller than 0.8, continuous decrease follow by a tiny increase in shear modulus is found. This maybe attributed to the fact that SC structure cannot efficiently react to shear force in contrast to BCC structure. Whereas, $L_2/L$ have a little influence on bulk modulus. It can be observed that the relative elastic bulk modulus is almost 1, which maybe due to the fact that all configurations consist of SC and BCC lattices are stretching-dominated and shown to possess similar response.

Figure IV.3 also illustrates the evolution of Zener ratio as a function of $L_2/L$. Obviously, BCC and SC lattices are far from isotropy. Isotropy is achieved only when $L_2/L$ lies between 0.5 and 0.6. To further distinguish the exact value for $L_2/L$ to reach isotropy, a series of unit cell simulations with $L_2/L$ ranging from 0.5 to 0.6 are conducted. After finishing simulations, a generalized Least Squares method is used to estimate the obtained Zener ratios and generate approximate function. By setting value of the function equal to 1, then we get the $L_2/L$ for elastic isotropy,

which can be validated by numerical simulation. The same analysis methodology is applied to obtain the corresponding $L_2/L$ for other relative densities, as shown in Figure IV.3 b, represented by blue dot. The geometrical ratio $L_2/L$ is almost linear with relative density. As the relative density increases, $L_2/L$ sightly decreases. When the relative density increases from 0.01 to 0.2, $L_2/L$ for isotropy changes from 0.568 to 0.545.

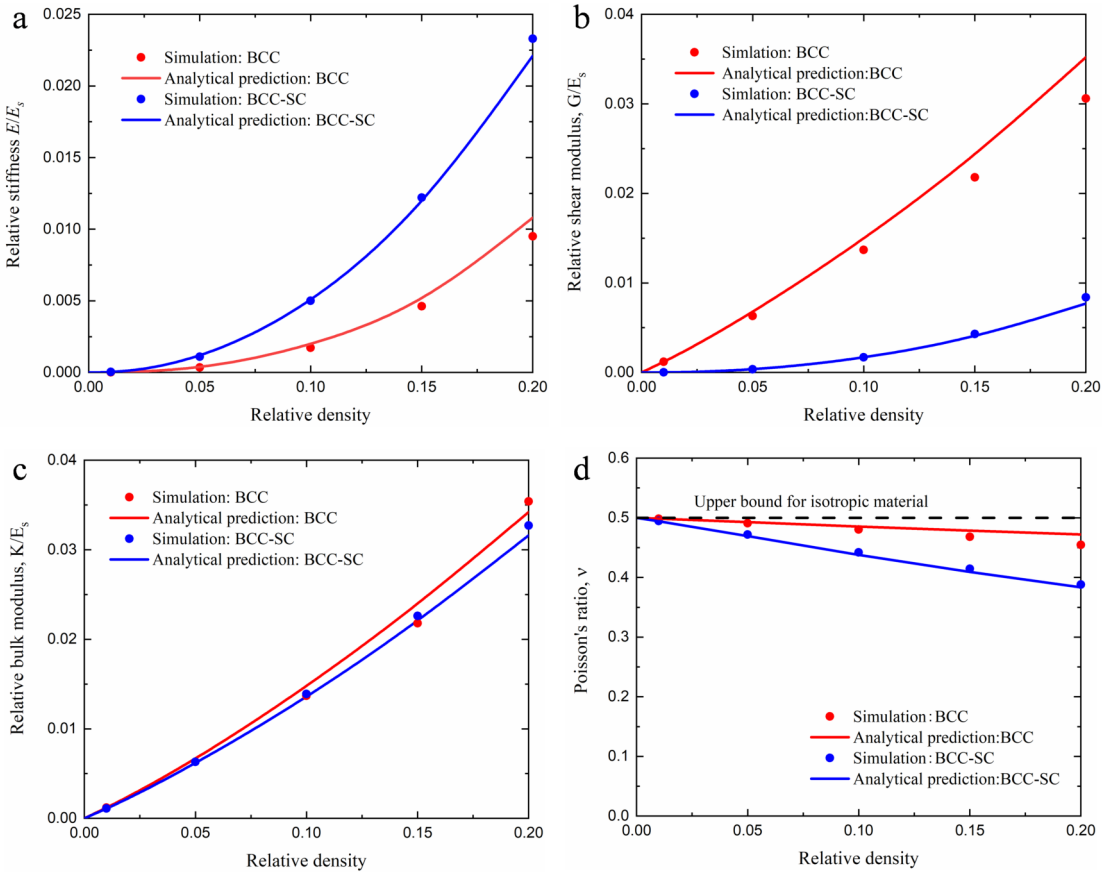


Figure IV.4: Comparison of relative elastic properties from simulations and analytical theory for BCC lattice and BCC-SC lattice.

### IV.3.3 Elastic properties

Figure IV.4 depicts comparison of relative stiffness, relative shear modulus, relative bulk modulus and Poisson's ratio obtained from numerical simulation and analytical theory (see section A.3) for BCC lattice and BCC-SC lattice. For all elastic properties, the analytical predictions which account for nodal effect and bending effect are in good agreement with simulations. Observed that both BCC lattice and BCC-SC lattice are bending-dominated. The stiffness of the BCC-SC lattice is at least twice as large as that of the BCC lattice. Conversely, the shear modulus of the BCC lattice is always larger than that of the BCC-SC lattice

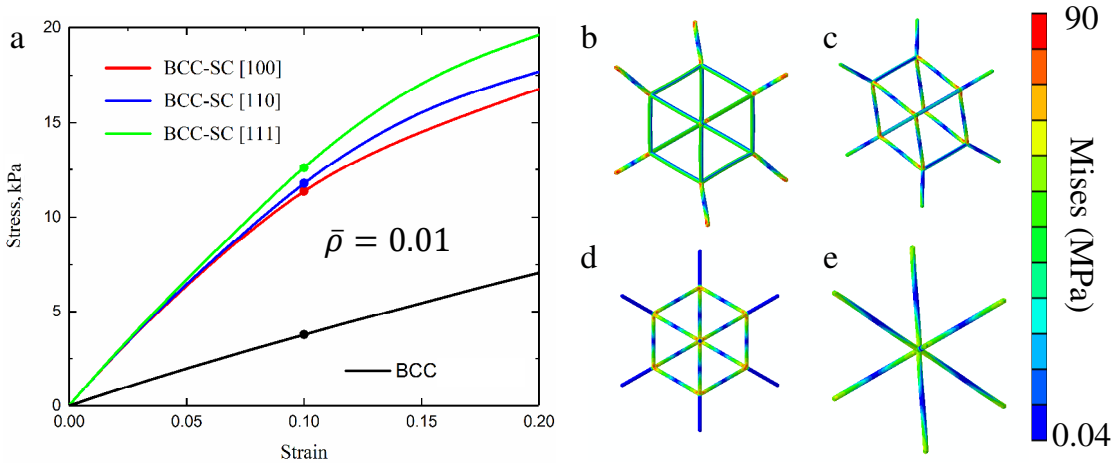


Figure IV.5: (a) At a relative density of 0.01, compressive response for isotropic BCC-SC lattice along [100], [110] and [111] directions and BCC lattice along [100] direction. (b)-(e) Illustration of the corresponding contour plot in stress when the applied strain is 0.1.

for relative densities of up to 0.2. Having a similar deformation mode with the BCC lattice, the BCC-SC lattce always possess nearly the same bulk modulus as the BCC lattice. Poisson's ratio of both configurations are also presented in Fig.Figure IV.4d. It is clear that the Poisson's ratio of BCC lattice is always larger than that of BCC-SC lattice. For both configurations, the Poisson's ratio decreases as relative density increases. In particular, the isotropic BCC-SC lattice with a relative density of 0.01 have a Poisson's ratio which almost attains the upper bound, 0.5, for isotropic material. This value of the effective Poisson's ratio leads to a fairly large ratio of bulk modulus to shear modulus of about $K/G = 90.6$, making the elastically isotropic BCC-SC lattice an interesting structural basis in the field of transformation elastodynamics (see section A.3).

### IV.3.4 Large deformation response and nonlinear isotropy

To investigate the nonlinear response of both configurations, a large engineering strain of -0.2 is applied on corresponding numerical models. For elastic isotropic lattices, additional uniaxial compression along [110] and [111] directions are performed to check the nonlinear isotropy. Figure IV.5a and Figure IV.6 present the stress-strain response for BCC lattice and isotropic BCC-SC lattices. It can be observed that the loading direction do not significantly affect the nonlinear response of isotropic BCC-SC lattices. For relative density ranging from 0.01 to 0.2, the strongest direction and weakest direction are [111] and [100], respectively. In all loading directions, the isotropic BCC-SC lattice exhibits an elastic response followed by a weakly increasing elastic-plastic behavior and a nearly constant stress plateau, which is similar to BCC lattice in [100] direction. With an applied uniaxial strain up to 0.1, their deformation and stress distribution are presented in

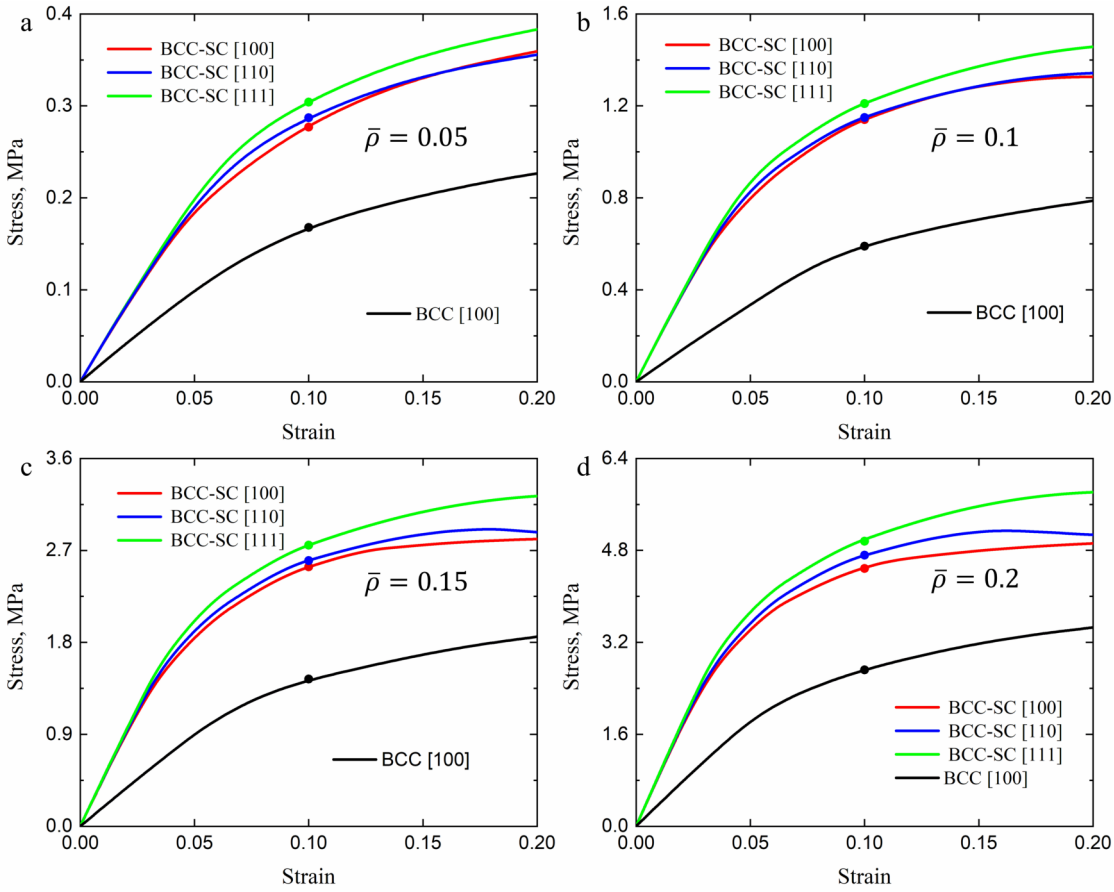


Figure IV.6: Stress-strain curves for two configurations with different relative density subjecting to different loading directions.

Figure IV.5b-e. During deformation, plastic bending hinges along with stress concentration occur around the nodes. It should be noted that the distribution of plastic bending hinges of the isotropic BCC-SC lattice are highly loading-direction depended. Plastic bending hinges can be found at the ends of diagonal struts for [100] direction and inner SC struts for [110] direction and [111] direction. This implies that the combination of inner SC lattice and outer BCC lattice provide sufficient rotational degrees of freedom and guarantee the occurrence of plastic bending hinges regardless of loading direction. Bending-dominated lattices are always failed by bending collapse rather than yield or buckling. As pointed out by Gumruka et al. [Gümrük 13], the collapse strength of bending-dominated lattices can be calculated from the intersection point of the elastic–plastic collapse and the plastic collapse regions. The collapse strength $\sigma_c$ is here defined empirically as the value of the engineering stress where strain equals 0.1. All of them have been highlighted in stress-strain curves as colored dots. For a fair comparison between different configurations, collapse strength in [100] direction are selected. The evolution of the relative collapse strength as a function of the relative density is shown in Figure IV.7. It is observed that the collapse strength of both configu-

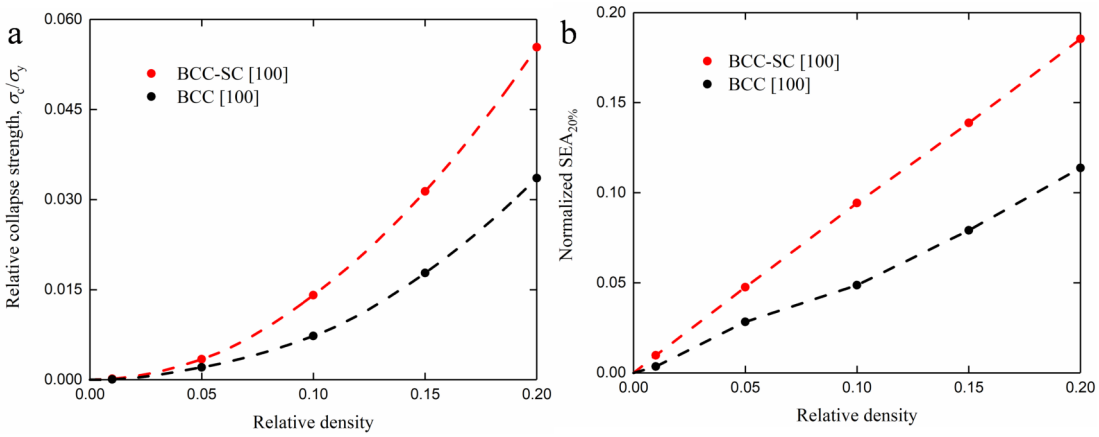


Figure IV.7: Evolution of (a) the relative collapse strength and (b) the normalized SEA as a function of relative density.

rations scales non-linearly with relative density. The BCC-SC lattice always has a higher relative compressive strength. For relative density around 0.2, the BCC-SC lattice has a relative strength about 1.6 times and a relative elastic modulus about 2.1 times larger than those of the BCC lattice.

The SEA is defined as the work performed by a uniaxial compression up to constant strain $\varepsilon_0$, taken as 0.2 for simulations and 0.5 for experiments, normalized by the total mass

$$\text{SEA} = \frac{V \int_0^{\varepsilon_0} \sigma d\varepsilon}{M}. \tag{IV.11}$$

In Figure IV.7b, the obtained results are normalized by the SEA of the constituent material, taken as 25.7 J/g. For both configurations, the normalized SEA varies nearly linearly with relative density. The BCC-SC lattice always has a larger normalized SEA. For relative density around 0.2, the BCC-SC lattice has a normalized SEA about 1.64 times larger than that of the BCC lattice (detailed experimental data can be found in Figure A.5).

Only elastic isotropy valid for small strain is enforced by the above design rules. For applications to energy absorption and load bearing, it is also important to quantify nonlinear anisotropy. In this respect, the collapse strength and the specific energy absorption (SEA) are the most important aspects for 3D energy absorbing metamaterials. They are respectively used to evaluate the load bearing capacity and the entire energy absorption of a structural lattice. In this work, we consider that nonlinear isotropy is achieved when both collapse strength and SEA are constant regardless of the loading direction. To check these mechanical properties, elasto-plastic solid elements simulations with compressive loading along 91 different directions were conducted [Suwas 14, Tancogne-Dejean 18a]. Nonlinear anisotropy is quantified by the ratios $\sigma_c^{\max}/\sigma_c^{\min}$ and $\text{SEA}^{\max}/\text{SEA}^{\min}$, where minima and maxima are taken over all loading directions in 3D space. Figure IV.8a and b summarize in the form of pole figures the dependence of collapse strength and specific energy absorption with loading direction for the BCC-SC lat-

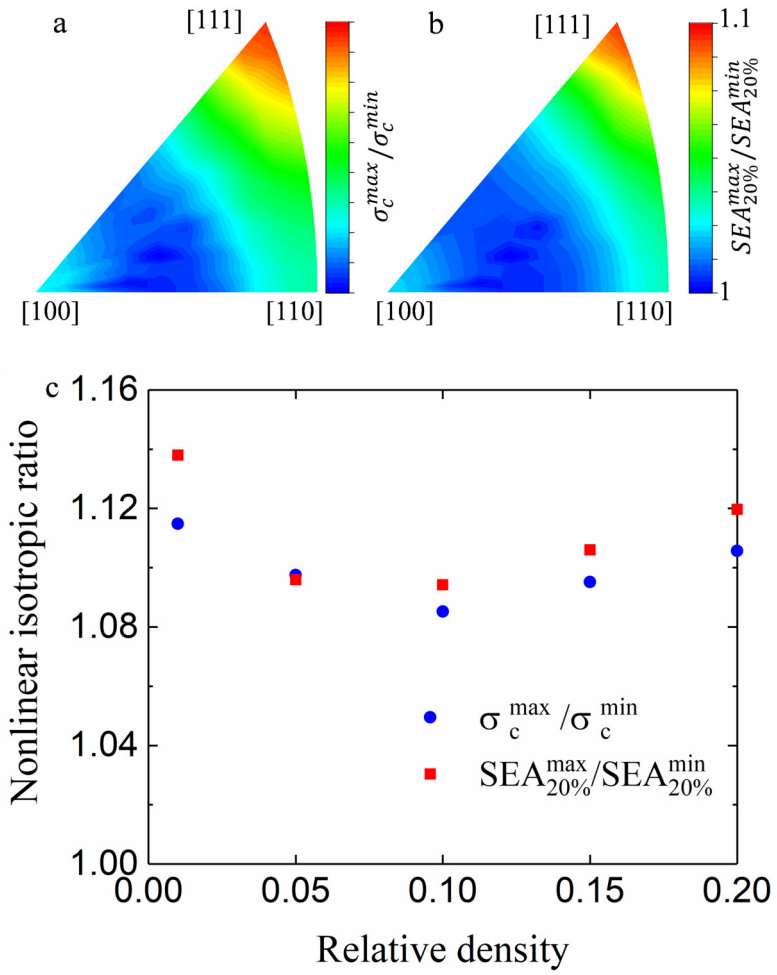


Figure IV.8: Pole figures for directional denpendency of (a) bending collapse strength distribution and (b) specific energy absorption distribution of the proposed mechanical metamaterial with a relative density of 0.1. (c) Nonlinear isotropic ratios as functions change with relative density.

tice with $\bar{\rho} = 0.1$. The largest nonlinear anisotropy ratios are $\sigma_c^{\max}/\sigma_c^{\min} = 1.08$ and $\mathrm{SEA}^{\max}/\mathrm{SEA}^{\min} = 1.09$. The softest direction is $[12, 4, 1]$, whereas the strongest direction is [111]. Similar trends are found for other relative densities.

The largest nonlinear anisotropy ratios are summarized by Figure IV.8c as a function of relative density. They initially decrease with the relative density to reach their minima for $\bar{\rho} = 0.1$, after which value they increase only slightly. For most values of the relative density, both nonlinear anisotropy ratios remain below 1.1, implying very limited nonlinear anisotropy. Even in the worst case, the nonlinear anisotropy ratios compare favorably with the case of other lattices displaying elastic isotropy [Gurtner 14, Tancogne-Dejean 18b, Tancogne-Dejean 18c, Tancogne-Dejean 18a]. That property makes the BCC-SC truss lattice a noteworthy alternative for load bearing and energy absorption.

## IV.4 Experiment

Samples were fabricated using a liquid photoresist (IP-Dip, Nanoscribe GmbH) and a commercial three-dimensional lithography system (Photonics Professional, Nanoscribe GmbH). The laser beam was focused by using a dip-in X63 objective lens with 1.4 numerical aperture. A Galvanometric scan speed of 10 m/s was used for the whole fabrication process. After polymerization was achieved, the sample was developed in a PGMEA (1-methoxy-2-propanol acetate) solution for 20 minutes to remove the unexposed photoresist.

In order to validate the design of the BCC-SC truss lattice, samples with different relative densities $\bar{\rho} = 0.01$, 0.05, 0.1, 0.15, and 0.2 were fabricated by direct laser writing. Scanning electron micrograph (SEM) images are shown in Figure IV.9. Both crystallographic directions [100] and [110] were considered to investigate the dependence of the compressive response with loading direction.

All [100] samples comprise $7 \times 7 \times 7$ unit cells. The unit cell lattice constant $L = 142.86$ µm for $\bar{\rho} = 0.01$ and $L = 71.43$ µm for $\bar{\rho} = 0.2$. For all other [100] samples, $L = 100$ µm. The strut diameter is $D = 5.2$ µm for $\bar{\rho} = 0.01$, $D = 8.4$ µm for $\bar{\rho} = 0.05$, $D = 12.2$ µm for $\bar{\rho} = 0.1$, $D = 15.2$ µm for $\bar{\rho} = 0.15$, and $D = 18.0$ µm for $\bar{\rho} = 0.2$.

The [110] unit cell is generated by cutting out a $2 \times 2 \times 1$ [100] structure along direction [001]. All [110] samples contain $7 \times 7 \times 10$ unit cells. Samples dimensions are $1414.21 \times 1414.21 \times 1428.57$ µm$^3$ for $\bar{\rho} = 0.01$ and $707.11 \times 707.11 \times 714.29$ µm$^3$ for $\bar{\rho} = 0.2$. All other samples have dimensions $989.89 \times 989.89 \times 1000$ µm$^3$. The strut diameter is the same as that of [100] samples with the same relative density.

Under compression, samples are placed between a fixed glass substrate and a flat loading device. Samples were placed between a glass substrate and a flat loading stamp driven with a stepping motor. Position was read directly from the linear stage. In addition, the true strain was obtained via image cross correlation from a digital camera equipped with a 20X objective lens facing the sample to monitor the deformation of the lateral faces of the sample under compression test.

Figure IV.10 summarizes the compressive stress-strain curves and acquired deformation frames obtained experimentally with the different samples. The [100] sample for $\bar{\rho} = 0.01$ first deforms elastically but then follows a weakly nonlinear and increasing behavior (see Figure IV.10a). After reaching the first peak stress of about 20 kPa at a strain of 0.1, the response of the sample retains slightly buckling oscillations. The sample collapses from lower to upper boundaries in a layer by layer fashion. Unlike other stretching dominated lattices or buckling structures, the amplitude of oscillations remains rather small. This indicates that the post-collapse behavior should be stable and that the sightly buckling mode originates from the low resilience of thin struts to imperfections and flaws.

For relative density $\bar{\rho} = 0.05$, the buckling behavior of structures with ultra-low strut aspect ratio $D/L$ is suppressed, and the deformation becomes uniform. The [100] sample exhibits an initially increasing elastic behavior followed by a weakly

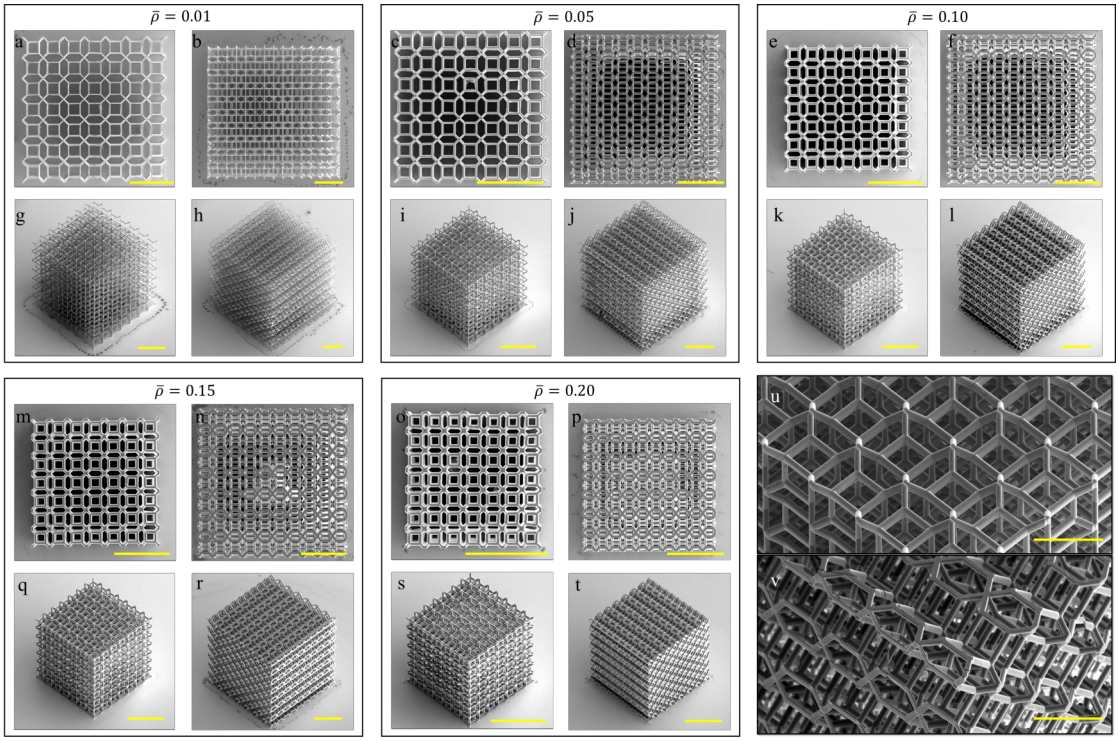


Figure IV.9: Scanning electron micrographs of BCC-SC truss micro-lattice samples fabricated via direct laser writing technology. (a–f) and (m–p) show top views of alternating [100] and [110] BCC-SC truss-lattice samples with varying relative density $\bar{\rho}$. (g-l) and (q-t) show isometric views of the same samples. (u) and (v) are close-up views of the samples with $\bar{\rho} = 0.05$. Scale bar lengths are (a–t) 300 µm and (u-v) 100 µm.

increasing elastic-plastic response (Figure IV.10b). The following plateauing behavior continues until the engineering strain reaches 0.25. During this process, the BCC-SC micro-lattice appears to possess a similar but enhanced bending-dominated mechanical behavior compared to the BCC lattice (see section A.3). This may be attributed to the facts that rotational micro-components allow for large steady deformations and that supporting micro-components provide additional structure stiffness and strength. The incredibly stable post-collapse response makes the BCC-SC lattice more suitable for energy absorption compared with other lightweight stretching-dominated truss lattices, such as the octet truss lattice [Tancogne-Dejean 16] and other hybrid lattices [Tancogne-Dejean 18c]. When the applied strain is larger than 0.25, rotational components contact each other and rotational degrees of freedom disappear. As a result, vertical struts have to support more bending moment, and are therefore very sensitive to shearing forces and flaws. When the compressive loading direction is not absolutely vertical, the shearing force introduced by friction between the loading stage and the sample results in uneven deformations. Hence, the mechanical behavior changes from a stable and increasing mode to an unstable and slightly oscillating mode.

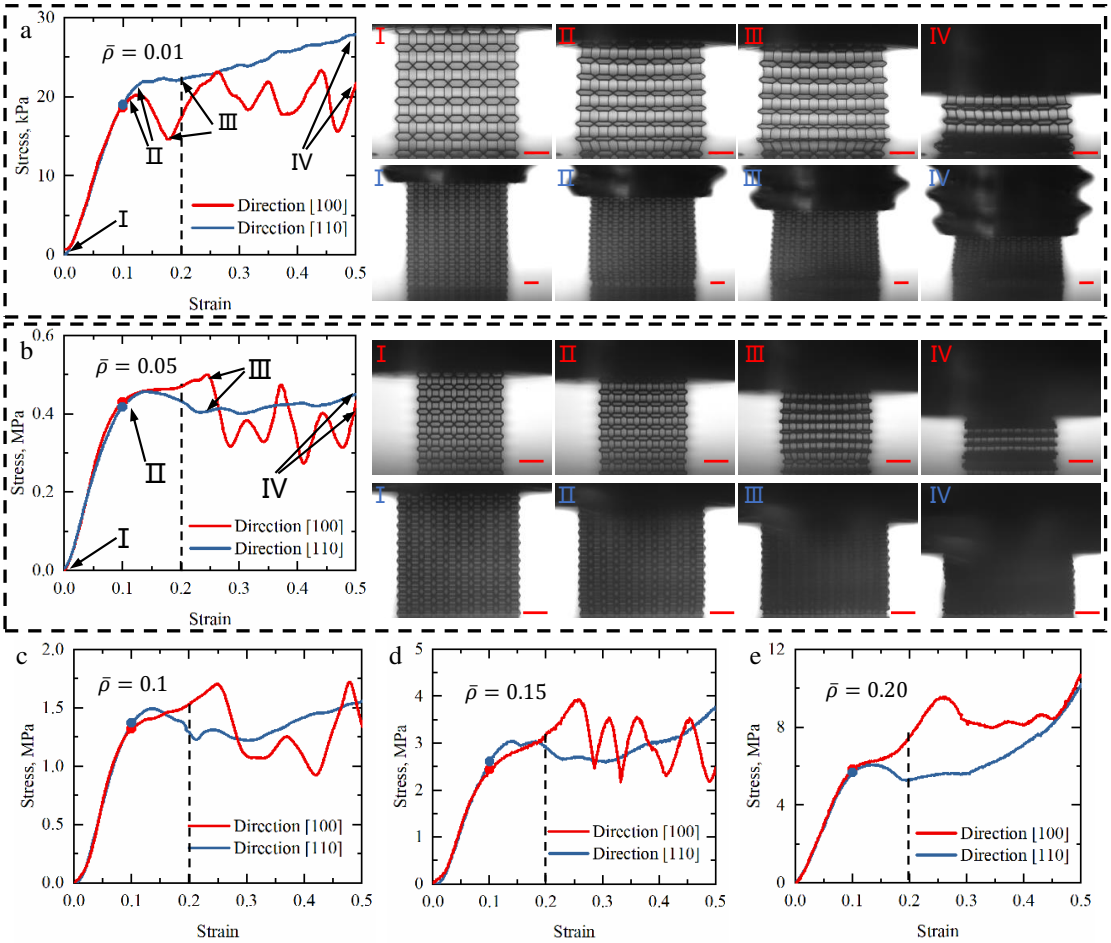


Figure IV.10: Compression experiments with BCC-SC micro-lattice samples fabricated by two-photon polymerization along directions [100] and [110]. (a) Nonlinear mechanical response and corresponding frames acquired during compression tests on samples with a relative density of 0.01. Frames I to IV show the initial, collapse deformation, global unstably or steady deformation, and large compression up to maximum applied strain. (b) Nonlinear mechanical response and corresponding frames acquired during compression tests on samples with a relative density of 0.05. Frames I to IV show the initial, collapse deformation, inelastic buckling, and large compression up to maximum applied strain. (c-e) Stress-strain curves are shown for samples with higher relative densities. All scale bars are 200 µmlong. The dotted line at 20% strain marks the upper limit of available numerical simulation data.

The compressive response of samples with relative density $\bar{\rho} = 0.1$ and 0.15 show trends similar to those at 5% relative density and their collapsing modes are similar. As the relative density increases, the unstable mechanical behavior at large strain gradually reduces. When the relative density is larger than 0.2, oscillation modes disappear and the mechanical behavior is enhanced.

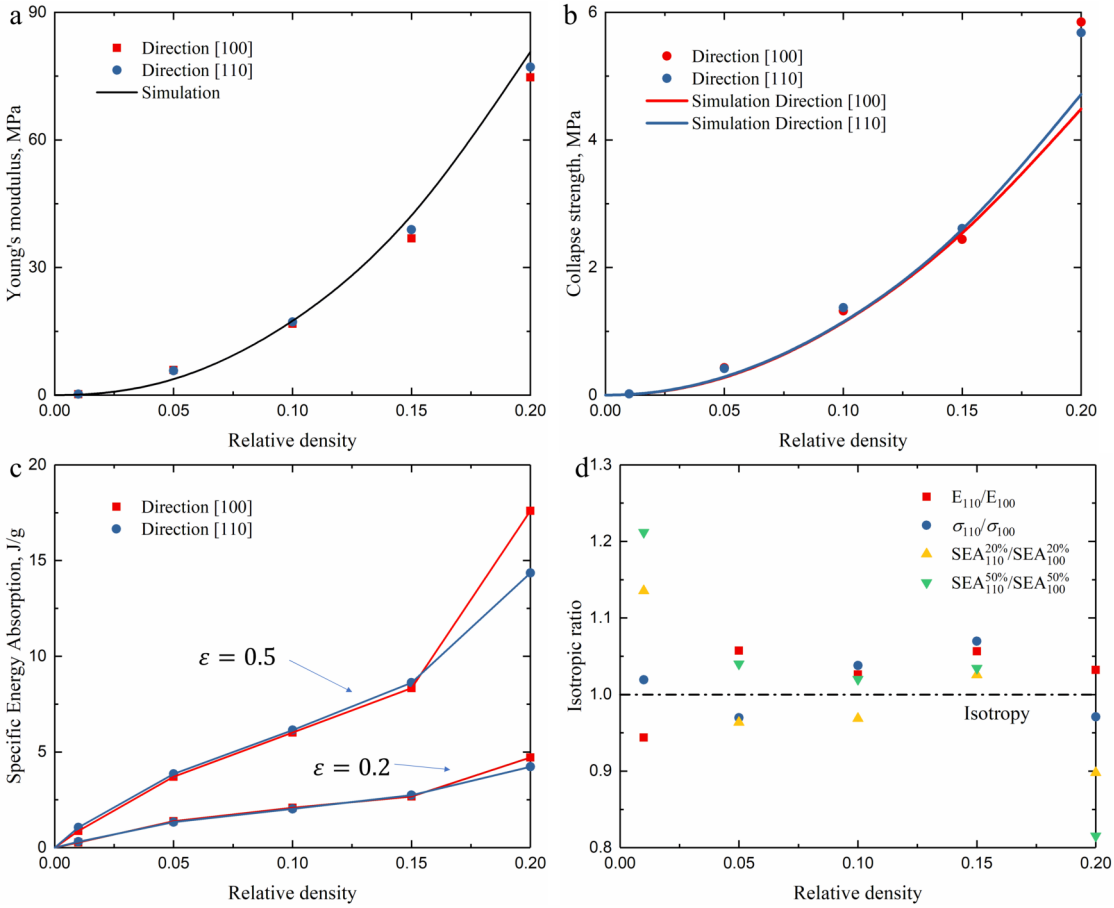


Figure IV.11: Mechanical data for samples measured during compression tests. (a) Young's modulus, (b) collapse strength, and (c) specific energy absorption are plotted against relative density for all tested samples. (d) Variations of isotropic ratios as a function of relative density demonstrate almost isotropic nonlinear mechanical response.

In contrast to [100] samples, all [110] samples exhibit almost the same elastic and elastic-plastic responses when the applied strain is less than 0.2. The following nonlinear response also appears to be more stable and to be slightly decreasing, at least for samples with relative density larger than 1%. Their stable behavior may be explained from the fact that [110] samples contain twice more rotational elements (i.e., inclined struts) compared to [100] samples, which provides enough rotational degrees of freedom to achieve stability. The decreasing response may be caused by brittle fracture of vertical struts (supporting elements) during fabrication (see Figure IV.9v) and by the smaller number of vertical struts.

The experimental Young's modulus and collapse strength of all samples are found to be in good agreement with numerical simulation and analytical results (Figure IV.11). When relative density is smaller than 0.15, $SEA_{50\%}$ and $SEA_{20\%}$ of BCC-SC samples appear to be almost linearly scale with relative density. At a

relative density of 0.2, samples possesses a SEA of about 17.5 $J/g$ which is twice as much as those with relative density of 0.15, while $SEA_{20\%}$ maintain linearly increasing trend which is line with simulation.

Elastic isotropy can be confirmed by the following two aspects. With same relative density, typical [100] and [110] samples exhibit nearly same elastic response. The absolute ratio of elastic modulus and collapse strength of [100] samples to that of [110] samples summarized in Fig. Figure IV.11 c are in fair agreement with simulation predictions. Experiment data are sightly higher or lower than the ideal linear isotropic ratio of 1. With regard to nonlinear isotropy, more complex mechanical responses should be identified. The trends of experiment results are in line with simulations,view from the SEA point. For all relative densities considered, deformation criterion, failure mode and nonlinear response of [100] samples are shown to be similar to those of [110] samples when applied strain is smaller than 0.2. The extreme values of about 1.13 and 0.9 can be found at relative densities of 0.01 and 0.2, relative density. For other relative densities, nonlinear isotropic ratio are close to 1. When the applied strain is 0.5, similar trend can be observed. The difference is that the extreme value at same relative density is sightly increasing. The contrast between test data and ideal isotropic ratio shows that our structure possesses not only elastic isotropy but also nearly nonlinear isotropy.

## IV.5 Conclusions

In this chapter, we have introduced a class of isotropic bending dominated truss lattice materials, formed by replacing the central connecting node of the body-centered cubic (BCC) truss lattice with a simple cubic (SC) truss lattice element, and we have examined its properties for energy absorption. The effective mechanical properties have been investigated both theoretically and numerically. Results show that the designed metamaterials exhibit not only isotropic stiffness, but also nearly isotropic nonlinear response. A series of samples with different relative densities were printed using two-photon polymerization in two different crystallographic directions, [100] and [110]. Uniaxial compression tests confirm that the BCC-SC lattice possesses nearly isotropic nonlinear response together with isotropic elastic properties.

# Chapter V

# Optimal isotropic, reusable truss lattice material with near-zero Poisson's ratio

## V.1 Introduction

Poisson's ratio $\upsilon$ is defined as the negative ratio of transverse to longitudinal strain [Timoshenko 70]. For a stable, isotropic and linear elastic material, Poisson's ratio is bound to remain between $-1$ [Milton 95, Huang 16], corresponding to 'dilational' or auxetic materials, and 0.5, a limit defining the 'incompressible' solid set by a positive energy requirement [Sokolnikoff 56, Gercek 07]. In nature, most conventional isotropic materials have a positive Poisson's ratio. Rubber, as well as most liquids, exhibits a Poisson's ratio of nearly 0.5. Rigid metals and polymers as a rule have a poisson's ratio ranging between 0.2 and 0.45 [Milton 95, Greaves 11]. For other soft metals and polymers, Poisson's ratio is usually between 0.33 and 0.5. By contrast, only a few natural materials such as bone have negative Poisson's ratio [Wojciechowski 15].

Recent advances in topological structural design have enabled the enlargement of the family of isotropic auxetics [Bückmann 14]. Carta *et al.* utilized threefold symmetry of the arrangement of voids to design a two-dimensional porous isotropic auxetic solid [Carta 16]. By embedding random re-entrant inclusions into a matrix, Hou *et al.* developed 2D composite structures with isotropic negative Poisson's ratio [Hou 12]. Combining the symmetry of a cubic lattice and that of additional diagonal elements, Cabras *et al.* presented a class of pin-jointed auxetic three-dimensional isotropic lattice material [Cabras 16]. Furthermore, by adopting finite small connections, Bückmann *et al.* designed, fabricated and characterized a three-dimensional auxetic isotropic metamaterial reaching an ultimate Poisson's ratio of $-0.8$ [Bückmann 14]. Lately, Frenzel et al. used auxetics combined with chirality to observe acoustical activity [Frenzel 17, Frenzel 19].

Isotropic structural materials with positive Poisson's ratio are generally designed for bearing different types of mechanical loads [Messner 16, Gurtner 14, Berger 17, Tancogne-Dejean 18a] or absorbing energy [Bonatti 19a]. The most popular way to optimise isotropy is to overlapp different structures in order to increase the number of equivalent directions and thus, via geometry increase, isotropy [Tancogne-Dejean 18c, Tancogne-Dejean 18b, Gurtner 14, Xu 16, Latture 18]. Gurtner *et al.* proposed the first optimal and isotropic three-dimensional truss-lattice structure [Gurtner 14]. Tancogne *et al.* further formulated analytical conditions on the lattice topology to achieve elastic isotropy [Tancogne-Dejean 18c] and studied the effect of bending ratio to axial stiffness of the micro-strut on structural isotropy [Tancogne-Dejean 18b]. Bonatti *et al.* recently reported a family of elastically-isotropic shell-lattice materials whose Young's modulus is always higher than that of optimal isotropic truss-lattices and approaches the Hashin–Shtrikman bound at high relative densities [Bonatti 19a]. Berger *et al.* presented a class of cubic-octet hybrid closed foams achieving the Hashin–Shtrikman upper bounds on isotropic elastic stiffness [Berger 17]. Tancogne *et al.* identified a class of low-density plate-lattice metamaterial showing optimal isotropic stiffness and nearly isotropic yield strength [Tancogne-Dejean 18a].

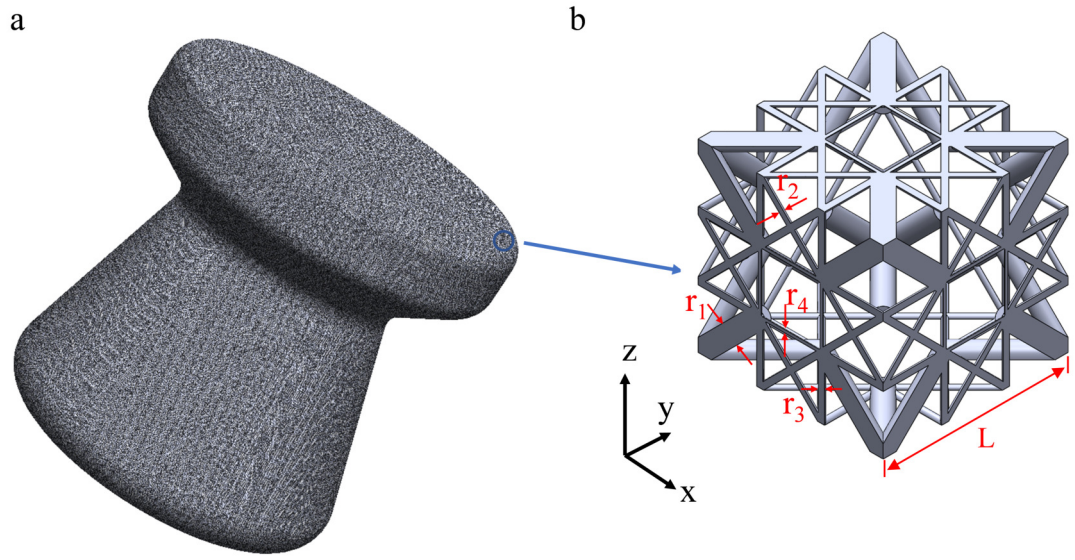


Figure V.1: Principle of the truss lattice material with near-zero Poisson's ratio. (a) Artistic illustration of a truss lattice bottle stopper and (b) corresponding representative unit cell with geometrical parameters indicated.

Cork, a conventional natural material, is emblematic among near-zero Poisson's ratio materials [Gibson 81, Fortes 89]. It shows very little lateral expansion when compressed and is widely used to seal bottles, especially for wine. As a composite, it is almost transversally isotropic and its Poisson's ratio is indeed a symmetric tensor. Independent Poisson's ratio constants $\upsilon_{12} = 0.097$, $\upsilon_{13} = 0.064$, and $\upsilon_{23} = 0.26$ have been reported for cork [Fortes 89]. Polymeric foams may have been the earliest case for lightweight isotropic material with a Poisson's ratio smaller than 0.1 [Greaves 11, Grima 06]. Their fabrication technique, however, differs significantly from current 3D printing technologies. With the new additive manufacturing techniques it is extremely difficult to program and print random structures such as foams and periodic motifs are hence preferred [Chen 20a, Bartlett 15, Bertoldi 10, Babaee 13, Florijn 14, Coulais 16, Fang 06, Zheng 14, Schaedler 11, Meza 14]. Recently, some efforts were made to design isotropic zero Poisson's ratio materials. Based on truss or thin frame beam theory, Sigmund presented a three dimensional optimal structure with zero Poisson's ratio [Sigmund 95]. Starting from a different structure, Guth *et al.* proposed another kind of 3D pin-jointed structure [Guth 15]. However, those well-designed isotropic structures have not been validated experimentally thus far. Moreover, subject to limitations of numerical algorithms, the effect of the nodal overlapping volume was not considered, which we find seriously influences mechanical properties, including isotropy and Poisson's ratio.

In this chapter, we aim at designing an isotropic near-zero Poisson's ratio material based on a periodic microstructure with cubic symmetry, that can be scaled easily and fabricated additively. We base our design on the hybrid truss lattice structure of Figure V.1 that was first presented by Sigmund [Sigmund 95]. The

unit cell follows simple cubic symmetry. Isotropy and near-zero Poisson's ratio are set as goals of a multi-objective optimization procedure where the radii of the struts are the optimized parameters. Optimization results in an almost isotropic design with Poisson's ratio less than 0.08 in all directions. Samples are printed using two-photon polymerization at a lattice constant of 300 $\mu$m in two different crystallographic directions, [100] and [110]. Uniaxial compression tests confirm the isotropic near-zero Poisson's ratio but also the recovery of the material after enduring strains up to 20%. Such a mechanical behavior thus makes it potentially attractive for product protection and goods packaging. When suffering from impact loading, limiting stress can pass through the protection toward the product. The layer-by-layer buckling failure mode will further enhance this protection ability. Moreover, the recovery ability can save space for packaging which is important in aerospace applications.

## V.2 Evaluation of isotropy and Poisson's ratio

The constitutive law of linear elasticity of three-dimensional composites relates the stress tensor $\boldsymbol{\sigma}$ to the strain tensor $\boldsymbol{\epsilon}$ via an effective order-4 symmetric stiffness tensor $\boldsymbol{C}$ as

$$\boldsymbol{\sigma} = \boldsymbol{C} : \boldsymbol{\epsilon}, \tag{V.1}$$

where $C_{ijkl} = C_{klij} = C_{jilk}$. For lattice materials with simple-cubic symmetry [Rand 07, Bückmann 14], the effective stiffness tensor has only three independent elements and can be rewritten in Voigt notation [Voigt 10],

$$\boldsymbol{C} = \begin{bmatrix} C_{11} & C_{12} & C_{12} & 0 & 0 & 0 \\ & C_{11} & C_{12} & 0 & 0 & 0 \\ & & C_{11} & 0 & 0 & 0 \\ & & & C_{44} & 0 & 0 \\ & sym & & & C_{44} & 0 \\ & & & & & C_{44} \end{bmatrix}. \tag{V.2}$$

Using the Christofell equation for elastic waves [Laude 15, Christensen 15], the independent stiffness elements can be expressed using the effective mass density and phase velocities in selected directions of propagation. The effective mass density $\rho$ is defined as the product of volume filling fraction $f$ by the mass density $\rho_0$ of the constituent material [Gibson 99a]. Only three phase velocities $v$ are required to identify all three independent stiffness constants. We consider the three bulk waves in direction [110]. One is a pure-shear wave S1 polarized along direction [001], the other two are quasi-longitudinal L and quasi-shear S2 waves with mixed polarization in the $(x, y)$ plane. For propagation in direction [110], the

Christofell equation leads to [Tsang 83, Bückmann 14]

$$C_{44} = \rho v_{\mathrm{S1}}^2, \tag{V.3}$$
$$C_{12} = \rho v_{\mathrm{L}}^2 - \rho v_{\mathrm{S1}}^2 - \rho v_{\mathrm{S2}}^2, \tag{V.4}$$
$$C_{11} = \rho v_{\mathrm{L}}^2 - \rho v_{\mathrm{S1}}^2 + \rho v_{\mathrm{S2}}^2. \tag{V.5}$$

For propagation along direction [100], Equation V.3 would be unchanged whereas Equation V.5 would give $C_{11} = \rho v_L^2$. Isotropy requires velocity to be independent of the direction of propagation and hence implies

$$v_{\mathrm{S1}} = v_{\mathrm{S2}} \quad \text{along direction [110]}. \tag{V.6}$$

Reciprocally, if Equation V.6 holds then there are only two independent stiffness constants instead of three and the stiffness tensor is isotropic. As a whole, Equation V.6 is a necessary and sufficient condition for isotropy. Poisson's ratio for compression along the principal axes can be expressed as [Hill 52, Bower 09]

$$\upsilon = \frac{C_{12}}{C_{11} + C_{12}}. \tag{V.7}$$

Hence, we can estimate Poisson's ratio in direction [110] using the following formula

$$\upsilon = \frac{v_{\mathrm{L}}^2 - v_{\mathrm{S1}}^2 - v_{\mathrm{S2}}^2}{2(v_{\mathrm{L}}^2 - v_{\mathrm{S1}}^2)}, \tag{V.8}$$

where velocities are measured along direction [110]. If isotropy is simultaneouly achieved, formula Equation V.8 is valid for all directions of propagation.

In practice, velocities are obtained numerically using a finite element model of the unit cell in Fig. Figure V.1(b) subjected to Bloch periodic boundary conditions. A small wavenumber $k = \pi/(100L)$ is considered along direction [110] and eigenfrequencies are obtained. The three lowest eigenfrequencies, when divided by $k$, give velocities $v_{\mathrm{S1}}$, $v_{\mathrm{S2}}$ and $v_{\mathrm{L}}$; they are readily classified as longitudinal or shear by comparing the polarization of the eigenfunctions.

We note another useful expression for the Poisson's ratio for cubic symmetry that is valid for an arbitrary compression direction [Wojciechowski 05, Paszkiewicz 02, Bückmann 14].

$$\upsilon(\phi, \theta) = -\frac{Ar_{12} + B(r_{44} - 2)}{16[C + D(2r_{12} + r_{44})]} \tag{V.9}$$

with

$$r_{12} = \frac{S_{12}}{S_{11}}, \tag{V.10}$$

$$r_{44} = \frac{S_{44}}{S_{11}}, \tag{V.11}$$

$$A = 2[53 + 4\cos(2\theta) + 7\cos(4\theta) + 8\cos(4\phi)\sin^4(\theta)], \tag{V.12}$$

$$B = -11 + 4\cos(2\theta) + 7\cos(4\theta) + 8\cos(4\phi)\sin^4(\theta), \tag{V.13}$$

$$C = 8\cos^4(\theta) + 6\sin^4(\theta) + 2\cos(4\phi)\sin^4(\theta), \tag{V.14}$$

$$D = 2[\sin^2(2\theta) + \sin^4(\theta) + \sin^4(2\phi)], \tag{V.15}$$

where $(\theta, \phi)$ are the azimuthal and polar angles in spherical coordinates. The compliance tensor $\boldsymbol{S}$ is the inverse of the stiffness tensor $\boldsymbol{C}$.

## V.3 Optimization of the structure

### V.3.1 Optimization strategy

The cubic-symmetry truss lattice structure of Figure V.1 was selected for optimization. The corresponding representative unit cell model contains 64 struts of four different types. The unit cell length $L$ being fixed to 300 µm, there are four geometrical parameters, $(r_1, r_2, r_3, r_4)$, available for optimization. The ranges of the design parameters were fixed as $14\,\mu\text{m} \leq r_1 \leq 16\,\mu\text{m}$, $4\,\mu\text{m} \leq r_2 \leq 6\,\mu\text{m}$, $4\,\mu\text{m} \leq r_3 \leq 6\,\mu\text{m}$, and $2\,\mu\text{m} \leq r_4 \leq 4\,\mu\text{m}$. Note that we adopt a geometry type similar to Sigmund's [Sigmund 95], but with completely different geometrical parameters. The ranges of the parameters are selected to satisfy the requirement of elastic buckling and the limitations of the 3D printer (Direct Laser Writing by Nanoscribe). Compared with the structure originally proposed by Sigmund, we consider larger values for $r_1$ but smaller values for $r_2$, $r_3$, and $r_4$.

Figure V.2 illustrates the detailed flowchart for optimization. The optimization problem aims at simultaneously imposing the isotropy condition Equation V.6 and minimizing Poisson's ratio Equation V.8. The objective functions to be minimized are thus selected as

$$Iso(r_1, r_2, r_3, r_4) = |v_{S1} - v_{S2}|, \tag{V.16}$$

$$v(r_1, r_2, r_3, r_4) = \left| \frac{v_L^2 - v_{S1}^2 - v_{S2}^2}{2(v_L^2 - v_{S1}^2)} \right|. \tag{V.17}$$

Eigenfrequency study, performed by a commercial finite element software package (COMSOL Multiphysics), was adopted to calculate the required velocities. To ensure convergence of simulations, the truss lattice structures were modeled with

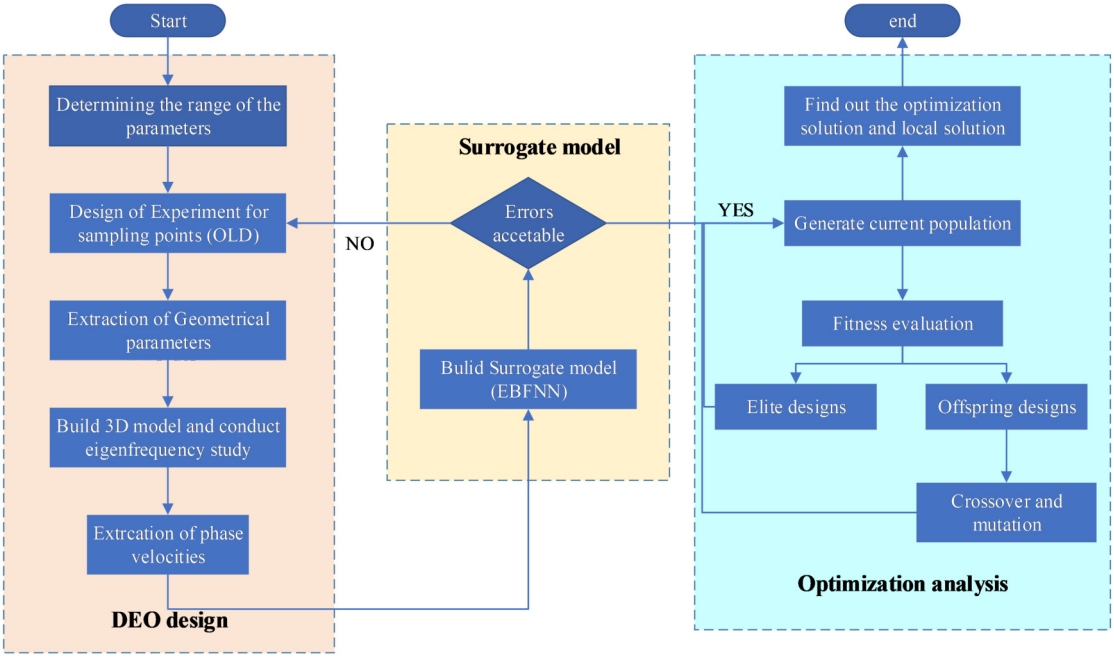


Figure V.2: Detailed flowchart for optimization assisted by an elliptical basis function neural network and coupled with finite element simulations.

several hundred of thousands of linear tetrahedral finite elements (type C3D10M). For the thinnest strut, there exist at least 10 elements around the circumferential direction. Bloch-periodic boundary conditions were imposed onto the representative unit cell shown in Figure V.1. The constituent material chosen is assumed isotropic and linearly elastic with Young's modulus $E_0 = 2$ GPa, $\upsilon_0 = 0.4$, and mass density $\rho_0 = 1000$ kg $\cdot$ m$^{-3}$.

The parameter space was sampled in order to reduce the computational burden during optimization. Toward this end, a surrogate model was created from a finite number of parameter space samples. One hundred sample points were first generated according to optimal Latin-hypercube design (OLD). This method was used to distribute sample points so that they are well spread over the design region without replicated coordinate values, often symmetric, and nearly optimal [Paszkiewicz 02]. The generated sample points are listed in Table A.1. A surrogate model was then generated and optimization was performed on the reduced parameter space, as described next.

### V.3.2 Surrogate models

The elliptical basis function neural network (EBFNN) technique has proven effective in approximating a continuous function of $n$ variables in very complex cases [Bishop 91, Schilling 01, Mak 00]. A detailed introduction to EBF is given in Ref. [Shi 18]. From the parameter space samples, a EBFNN was constructed to generate approximate surrogate models of the three velocities $\upsilon_{S1}$, $\upsilon_{S2}$ and $\upsilon_L$.

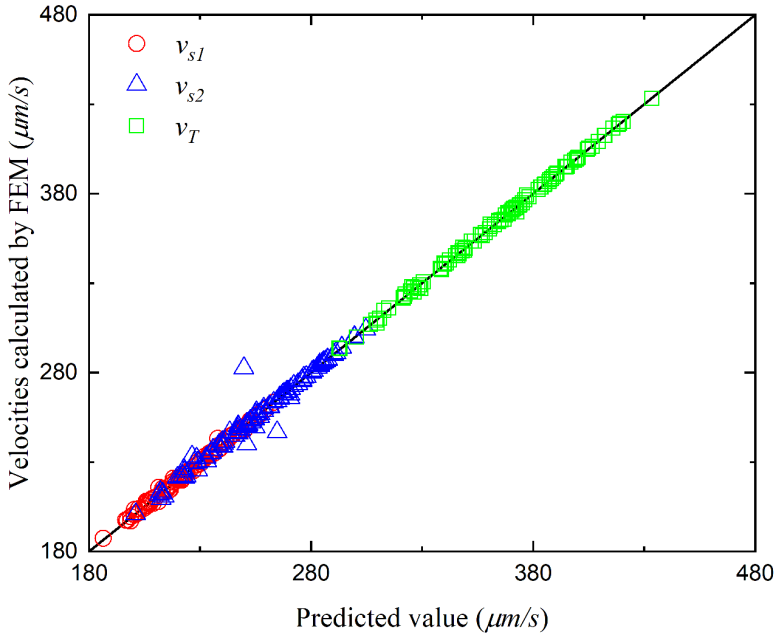


Figure V.3: Comparison of velocities predicted by EBFNN with velocities obtained by FEM.

| Velocity | RMSE | $R^2$ |
|---|---|---|
| $v_{S1}$ | 0.01546 | 0.99534 |
| $v_{S2}$ | 0.0403 | 0.96955 |
| $v_L$ | 0.00591 | 0.99934 |

Table V.1: Accuracy measures of the EBFNN surrogate models.

The coefficient of determination ($R^2$) and the root mean square error (RMSE) are used to evaluate the reliability of the surrogate models. These estimators are defined as

$$R^2 = 1 - \frac{\sum_{i=1}^{n}(y_i - \hat{y}_i)^2}{\sum_{i=1}^{n}(y_i - \bar{y})^2}, \tag{V.18}$$

$$\text{RMSE} = \sqrt{\frac{1}{n}\sum_{i=1}^{n}(y_i - \hat{y}_i)^2}. \tag{V.19}$$

In these expressions, $n$ is the number of samples, $y_i$ are the actual values of objective function at the sample points, $\hat{y}_i$ are the values predicted by the objective function, and $\bar{y}$ is the mean value of objective function over all sample points. All sample points defined by OLD are used for cross-validation error analysis. The closer $R^2$ is to 1 and RMSE is to 0, the more accurate the model. For all surrogate models, $R^2$ is larger than 0.969 and RMSE is smaller than 4%, as listed in

Table V.1. These values indicate that the surrogate models have high credibility. Figure V.3 compares the velocities predicted by the surrogate models with the actual velocities, for all sample points. It can also be observed that the prediction error remains small in all cases. Of course, the usefulness of the surrogate models is to produce smooth estimates of the velocities for any continuous value of the quadruplet $(r_1, r_2, r_3, r_4)$.

| structure | Initial | Optimum 1 | Optimum 2 | Optimum 3 | Optimum 4 |
|---|---|---|---|---|---|
| $r_1$ (µm) | 14.444 | 15.000 | 15.960 | 15.535 | 15.000 |
| $r_2$ (µm) | 4.040 | 4.500 | 4.707 | 4.121 | 4.300 |
| $r_3$ (µm) | 5.111 | 5.100 | 4.303 | 4.909 | 4.850 |
| $r_4$ (µm) | 3.677 | 2.400 | 2.485 | 2.222 | 2.350 |
| $v_{s1}$ (µm/s) | 207.483 | 218.59 | 211.481 | 198.819 | 211.037 |
| $v_{s2}$ (µm/s) | 283.900 | 219.256 | 211.703 | 201.040 | 213.036 |
| $v_L$ (µm/s) | 383.421 | 323.220 | 314.556 | 293.675 | 313.001 |
| $\upsilon_{min}$ | 0.112 | 0.076 | 0.086 | 0.067 | 0.075 |
| $\upsilon_{max}$ | 0.239 | 0.077 | 0.087 | 0.073 | 0.080 |

Table V.2: Optimization results. Geometrical parameters, angular velocities in the [110] direction, and minimal and maximal values of Poisson's ratio $\upsilon$ for all compression directions are given for the initial and selected optimized designs.

### V.3.3 Optimization

Non-dominated sorting genetic algorithm (NSGA-II) [Deb 02] is used to find solutions to the optimization problem. Figure V.2 displays the optimization flowchart we follow. The current population of individuals contains two parts, the elite and the offspring points. In our case, its size is 12. As nondominated points, elites, that constitute not more than 50% of the population, are always inherited from the previous generation. In contrast, the offspring points are used for selection, crossover and mutation to generate the next generation. The probability of crossover and mutation are 0.9 and 0.1, respectively. Once the population is generated, a fitness evaluation is adopted to decide where design points go. Population update is continued until the maximum iteration number of 2000 is attained. To account for possible errors caused by the surrogate models, not only the optimum solution but also some local minima were extracted. By comparing simulations and optimization results, we picked up the four optimum designs listed in Table V.2. Velocities and Poisson's ratios are estimated by conducting finite element simulations again after optimization.

Figure V.4 plots Poisson's ratio in spherical coordinates for both the initial and the optimum structure 1. The original structure proposed by Sigmund was indeed rather anisotropic, with the Poisson's ratio obtained by FEM varying between 0.112 and 0.239 depending on the direction. This may be attributed to the fact that

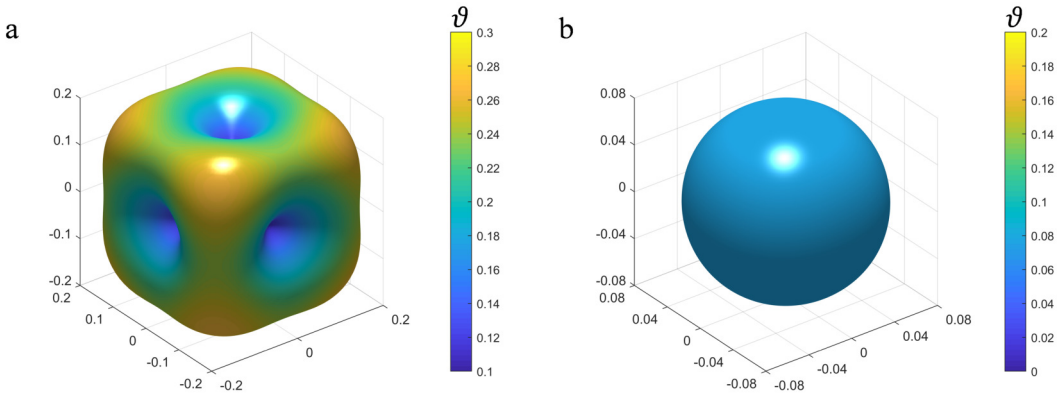


Figure V.4: Three dimensional polar plot of the Poisson's ratio following by Eq. (V.9) for (a) the initial structure and (b) the optimal isotropic structure 1.

the complex geometry of the nodes was not considered in the numerical algorithms used. In this case, actually, traditional truss or beam theories are not applicable. The mechanical properties obtained by such methods differ significantly from the FEM result. Moreover, the minimum Poisson's ratio was larger than the upper bound for cork, 0.1. After optimization, an almost isotropic value $\upsilon \approx 0.08$ is obtained for the four selected designs. The response of the optimum structure is clearly much more isotropic than cork.

## V.4 Experiment

All experimental samples are made from the 'IP-Dip' resin using the commercially available laser lithography system Photonic Professional GT (Nanoscribe GmbH, Germany). A drop of a negative-tone photoresist is placed on top of a fused silica substrate ($25 \times 25 \times 0.7$ mm$^3$) and polymerized using a femtosecond pulsed laser with vacuum wavelength $\lambda = 780$ nm. The laser beam is focused by using a dip-in $\times 63$ objective lens with 1.4 numerical aperture. A Galvanometric scan speed of 10 m/s was used for the whole fabrication process. After polymerization is achieved, the sample is developed in PGMEA (1-methoxy-2-propanol actetate) for 20 minutes to remove the unexposed photoresist.

Two different crystallographic directions are considered, [100] and [110]. Figure V.5 shows the unit cell models and the corresponding additively manufactured samples. The [100] sample, which is composed of $4\times4\times4$ unit cells, is constructed by stacking the corresponding unit cell in the three principal directions. Noting that the Poisson's ratio of lattice materials is mainly affected by the aspect ratio of micro-struts rather than by other geometrical parameters [Bückmann 14], we adopted the aspect ratios obtained from optimization and scaled the unit cell length proportionaly. The detailed geometrical parameters are: $L = 125$ µm, $r_1 = 6.3$ µm, $r_2 = 1.9$ µm, $r_3 = 2.1$ µm, and $r_4 = 1$ µm.

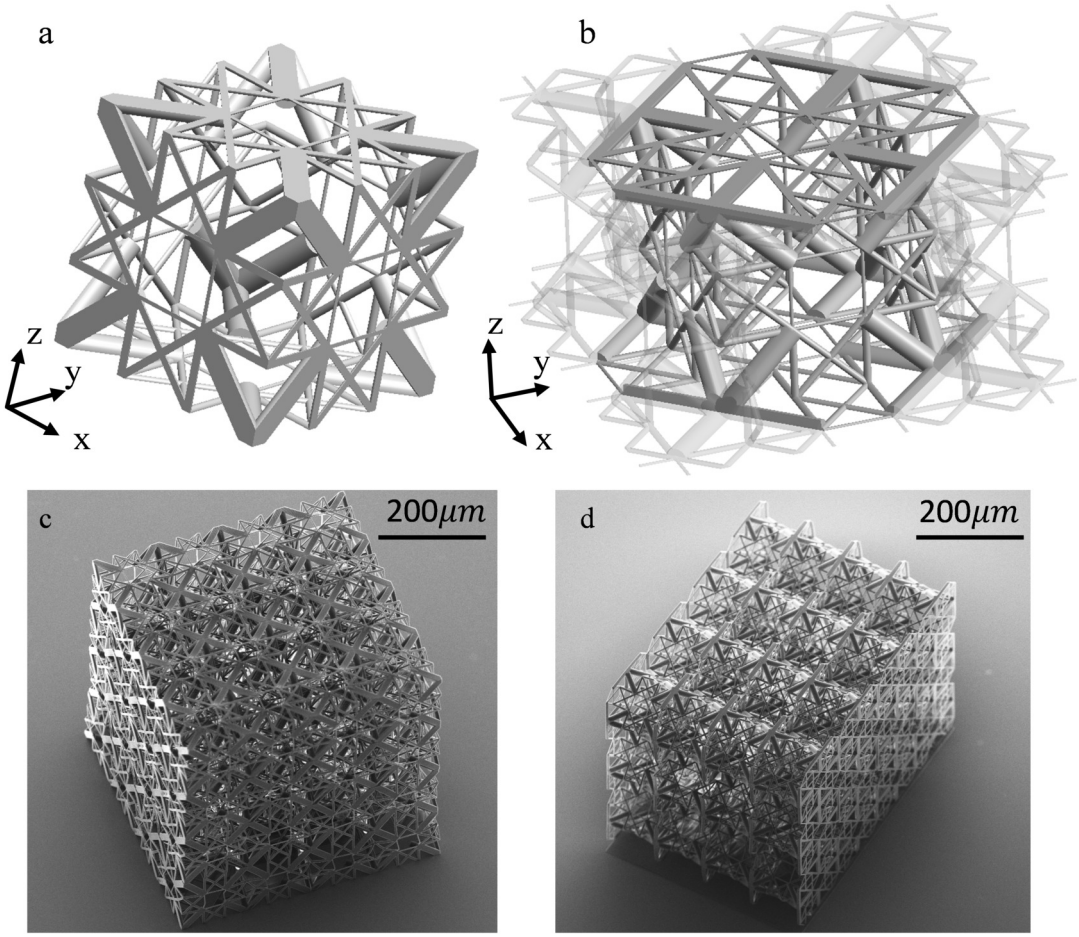


Figure V.5: Unit cell models of the isotropic truss lattice material for (a) the [100] direction and (b) the [110] direction. Electron micrographs are shown for (c) the [100] fabricated sample with $4 \times 4 \times 4$ unit cells and (d) the [110] fabricated sample with $4 \times 4 \times 3$ unit cells.

The [110] sample is generated by cutting out a [100] structure $2 \times 2 \times 1$ along the vertical direction. The horizontal basis vectors are then along directions [110] and $[\bar{1}10]$. It should be noted that the geometrical features of the [110] unit cell can be described by that of the corresponding [100] unit cell. Here, geometical parameters are $L = 150$ μm, $r_1 = 7.6$ μm, $r_2 = 2.3$ μm, $r_3 = 2.5$ μm, and $r_4 = 1.2$ μm. The [110] sample contains $4 \times 3 \times 4$ unit cells. The external dimensions are 848.4 μm $\times$ 636.3 μm $\times$ 450 μm.

Samples are placed between a fixed glass substrate and a flat loading device. The loading device is driven by a stepping motor with an attached force sensor. Position is directly read from the linear stage. The position is only used to monitor the fatigue of the material. The true strain is obtained via image cross correlation. To test the recovery ability of the samples, repeated compressive experiments are carried out at a speed of 0.001 mm/s, during which the applied displacement increases with loop number. A digital camera equiped with a 20× objective lens

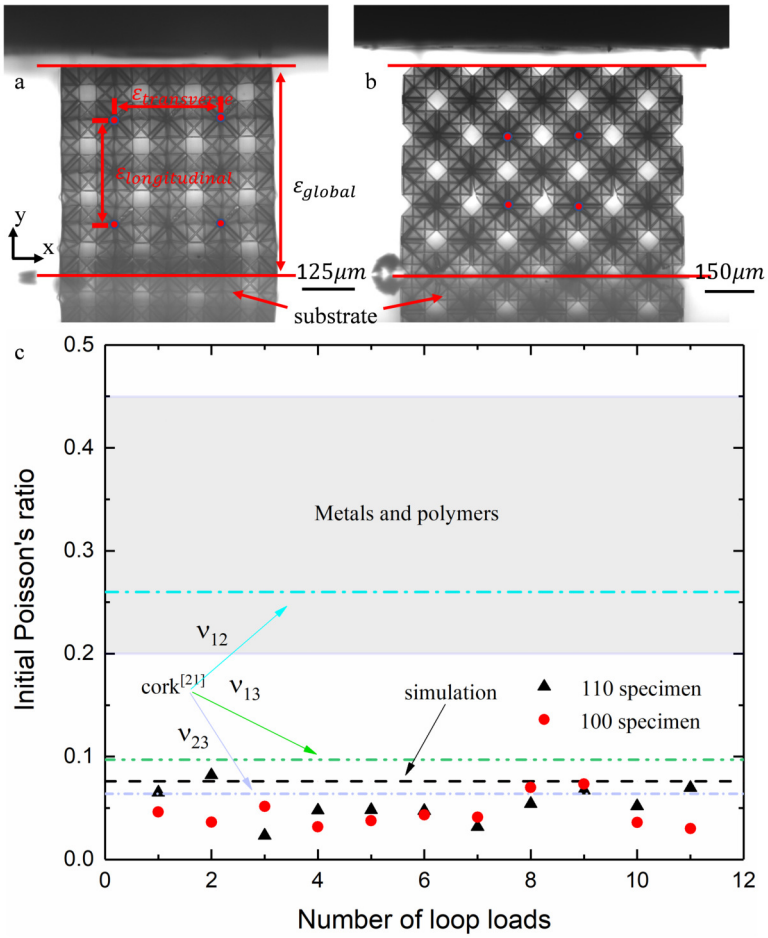


Figure V.6: Definition of reference points and reference lines used to determine the transverse strain, the longitudinal strain and the global strain, for (a) the [100] sample and (b) the [110] sample. (c) Poisson's ratio of the samples is plotted as a function of the number of experimental loop loads. Values for the FEM simulation, cork, metals and polymers are shown for comparison.

facing the sample is used to monitor the deformation of the lateral faces and hence to measure Poisson's ratio. Digital image correlation [Eberl 06] is used to track and analyze the displacement with sub-pixel resolution. To reduce the influence of boundaries, Poisson's ratio is calculated from the average local strain and the average transverse strain measured from 4 reference circles at the central row of unit cells as depicted in Figure V.6. Figure A.6 details the measurement of coordinates. Green stars and red stars stand respectively for undeformed and deformation coordinates. At the initial position, green stars overlap with red stars. Table A.2 lists representative data obtained from DIC for samples 100 and 110, where x and y stand for the original coordinates, and $x'$ and $y'$ are coordinates after deformation. The actual Poisson's ratio is calculated from the following

expression,

$$\upsilon = -\frac{(x_2' - x_1' + x_4' - x_3') - (x_2 - x_1 + x_4 - x_3)}{(y_1 - y_3 + y_2 - y_4) - (y_1' - y_3' + y_2' - y_4')}. \tag{V.20}$$

Global strain is determined by measuring the distance between the reference lines.

Figure V.6(c) presents the measured Poisson's ratio of the [100] sample and the [110] sample. For both samples, experimental data are in fair agreement with simulation results of Table Table V.2. The measurements are generally found to be smaller than the computed value. The contrast between samples shows that the proposed structure has a more isotropic response than cork and a much lower Poisson's ratio than other nature and man-made isotropic materials such as metals and Polymers. Moreover, the number of loop loading has a limited impact on the value of the Poisson's ratio. Even though some micro-struts break at large applied strain, the measured initial Poisson's ratio always fluctuates around the designed value of 0.076. For both configurations, the largest and the smallest Poisson's ratio measured in our cyclic experiments were about 0.08 and 0.025, respectively.

Figure V.7 summarizes the results of eleven cyclic compression experiments. A large vertical deformation together with a very small horizontal deformation are observed under compression, indicating that the structural materials have a nearly zero global Poisson's ratio. For both samples, the maximum applied strain increases almost linearly with the loop number. During the first and the last loop, the maximum strains of the [100] sample are 2% and 20%, respectively. As long as the applied strain remains smaller than 7%, the sample can recover completely after unloading. This property may be attributed to elastic buckling of the slender members in the micro-lattice. When the applied strain is increased above 7%, however, the recovery ability of sample weakens slightly. With a maximum applied strain of 20%, the sample can still recover almost 96.6% of its original height. In principle, the samples should possess even better recovery ability and should withstand larger strains. However, the slender micro-struts are very sensitive to flaws and imperfections. Hence the deformation of the sample may not be homogeneous and failure may start within any layer in the fashion of brittle break of the micro-struts . The compressive experiment validates our hypothesis. A similar trend regarding the recovery ability is found for the [110] sample . At large strain, brittle break of micro-struts is also the dominating failure mode of the tested sample . The only difference is that the recovery ability is further weakening. The [110] sample seems to be even more sensitive to flaws than the [100] sample. With a maximum applied strain of 16%, the [110] sample can almost recover 98.5% of its original height.

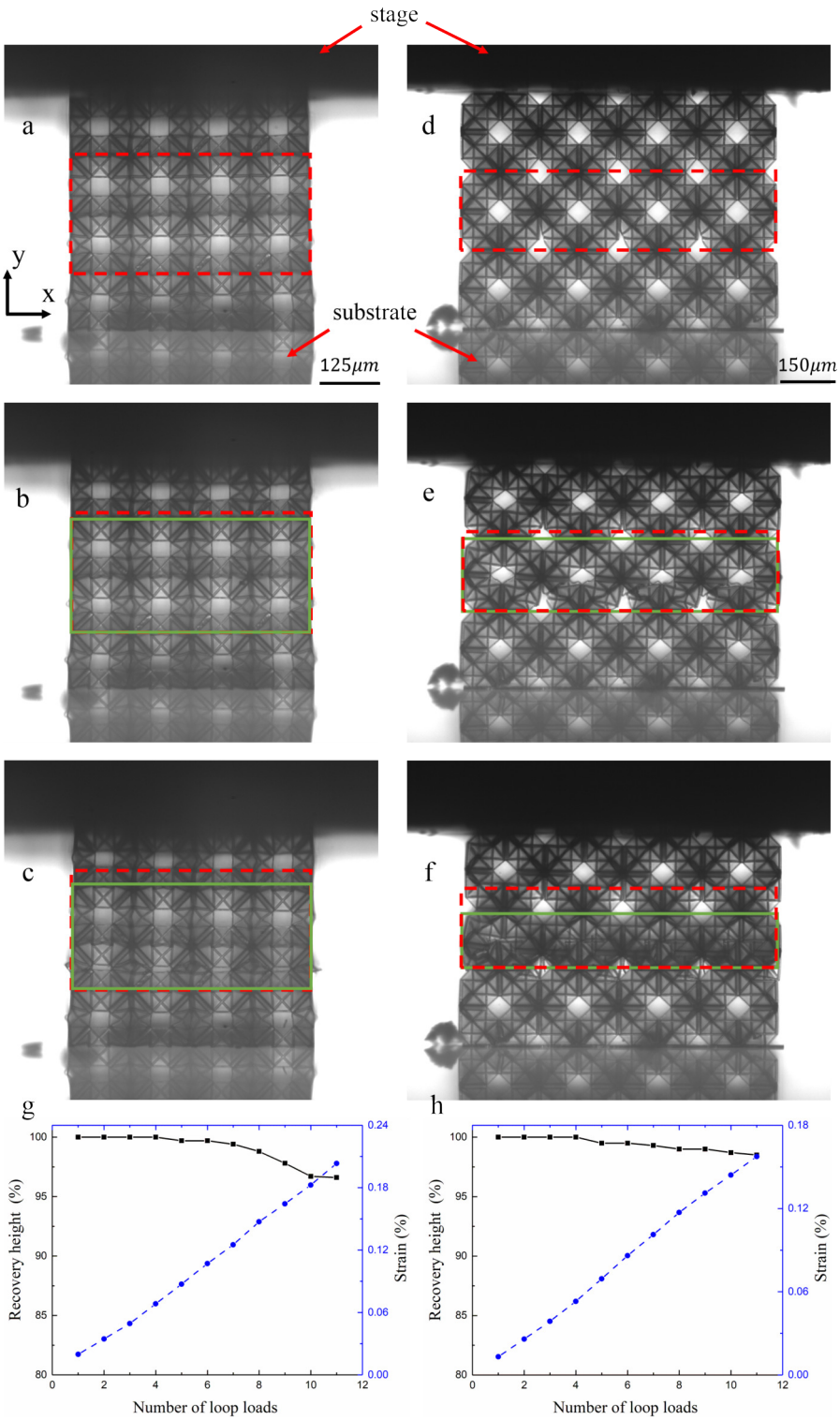


Figure V.7: (a-c) Views of the deformed [100] sample at 0%, 5% and 10% strain. (d-f) Views of the deformed [110] sample at 0%, 5% and 10% strain. The red dashed square and the green solid square are the initial and the deformed shapes of samples, respectively. (g,h) Recovery ability of the [100] and the [110] samples and maximum applied strain as a function of the loop number.

Compared with the original structure proposed by Sigmund, for which Poisson's ratio varies between 0.118 and 0.213, our structure is more isotropic. It would for instance make our structure more suitable as a bottle stopper. Moreover, our structure recovers 96.6% of its original shape after the 11th compressional test exceeding 20% strain. This mechanical behavior is attractive for product protection and goods packaging. When suffering from impact loading, limited stress can pass through the protection toward the product. The layer-by-layer buckling failure mode further enhances this protecting ability. Moreover, the recovery ability can save space for packaging which is important in aerospace applications. Compared with other traditional methods, our optimization method is simple and accurate. The optimization utilizing finite element simulation opens avenues for the design of 3D structures with very complex geometrical features, taking into account connected nodes, imperfections and so on.

## V.5 Conclusions

A new class of isotropic reusable cork-like metamaterial with near-zero Poisson's ratio was designed using a multi-objective genetic algorithm assisted by an elliptical basis function neural network combined with finite element simulations. We derived an objective function for simultaneously imposing elastic isotropy and controlling the value of Poisson's ratio. The optimal structures were fabricated and tested under repeated compression experiments. Results show that the samples fabricated using two-photon lithography have an almost isotropic near-zero Poisson's ratio. Furthermore, they can almost recover 96.6% of their original shape after the eleventh compressional test exceeding 20% strain. The number of loop loadings has a limited impact on the value of Poisson's ratio. Even though some micro-struts break at large applied strain, the Poisson's ratio still fluctuates around the designed value.

# Summary and Outlook

## Summary

With the scope of identifying the nodal effect on lattice materials, we successfully developed in chapter 1 an analytical model to predict the compressive stiffness and the strength of octet lattice material with cylindrical struts. The analytical model is in good agreement with finite element (FE) simulations and with experimental results, which validates its usefulness. Specimens of octet lattice material were manufactured from polyamid (PA). These compressive experimental results show that the compressive response of the octet lattice material changes from an unstable shear mode to a stable buckling free mode at a relative density between 0.22 and 0.23. This finding provides a guidance for material design. Moreover, the relative compressive stiffness and the strength not only depend on the relative density, but also on the strut joint, bend and shear. At low relative density, the strut joint effect is the dominating factor in stiffness analytical derivations. However, the importance of bend and shear are more obvious with an increase of the relative density.

Based on the above analysis, a new class of light-weight shell-lattice metamaterial was presented in chapter 2. Originating from the BCC truss lattice structure, we introduce spherical shell, hollow strut and smooth shell to optimize all hinges and bending parts such that they deform homogeneously. The mechanical properties are calculated numerically and verified experimentally under uniaxial compression. Compared to octet lattice metamaterials, the shellular metamaterial has a relative elastic modulus 2.4 times larger and a relative compressive strength about 5.4 times larger, for a relative density of 10%. The shell-lattice metamaterial has a specific energy absorption (SEA) nearly 3.56 times as large as the SEA of the BCC metamaterial.

Start from the last cubic lattice family, we have introduced inchapter 3 a class of lightweight simple-cubic closed tubular lattice material possessing ultra-high specific stiffness, ultra-high specific yield strength and stable post-yield response. Compared to the most stiff and strong smooth shellular lattice and tubular lattice materials, for the same relative density, the gain in average stiffness and strength is respectively 28% and 53%. Experiments with samples fabricated by direct laser writing (DLW) and numerical simulations demonstrate that the replacement of solid struts with closed tubes largely reduces the elastic and the yield anisotropy of simple-cubic lattice materials. As a direct benefit of the incredibly stable mechanical response of cylindrical tubes, the resistance of the closed tubular lattice

to buckling strength is further enhanced and recoverablity is foreseeable by further reducing the thickness of the shell. This work provides a feasible pathway for applications in lightweight design, loading support, and shocking absorption.

Chapter 4 proceeds with another attempt at conceiving an isotropic metamaterial with the nodal effect. we have shown a novel design of an extremely isotropic elastic metamaterial possessing isotropic behaviour beyond the linear regime and placing itself as a very promising candidate for energy absorption. The effective mechanical properties have been investigated both theoretically and numerically. Effect of geometrical parameters on mechanical properties are investigated, which helps us to identify the design map for isotropy. Analytical expressions for three elastic moduli and Poisson's ratio have been derived using Timoshenko beam theory. Good agreement between analytical prediction and simulation results are observed. Additional uniaxial compression simulations further show that the material possesses nearly isotropic nonlinear response together with elastic isotropic behavior. Compared with the BCC truss lattice, our materials are stiffer, stronger and can absorb more energy. Numerical results are confirmed by experimental tests.

Finally, optimization combined with the nodal effect was used in chapter 5 to design a new class of isotropic, reusable, cork-like metamaterial with near-zero Poisson's ratio. We derived an objective function for simultaneously imposing elastic isotropy and controlling the value of Poisson's ratio. Optimal structures were fabricated and tested under repeated compression experiments. Results show that the samples fabricated using two-photon lithography have an almost isotropic near-zero Poisson's ratio. Furthermore, they can almost recover 96:6% of their original shape after the eleventh compressional test exceeding 20% strain. The number of loop loadings has a limited impact on the value of Poisson's ratio. Even though some micro-structs break at large applied strain, the Poisson's ratio still fluctuates around the designed value.

## Outlook

The nodal effect on the mechanical properties of truss lattices has been identified in the present work. In the coming year, I would like to explore more possibilities on further research for functional metamaterial design and its fundamental theory. All mechanical metamaterials proposed in the thesis are only designed for application to support loading and absorb impact energy. However, numerous previous studies on lattice materials also show their potential in permeability, thermal conductivity, fatigue, and acoustic properties. That is, the nodal effect on the above physical properties of lattice materials may be treated through an extensive research.

In this thesis, octet lattice structure is the first example to show the nodal effect on mechanical properties. Based on small deformation assumption, we successfully derived an analytical model for elastic modulus and collapse strength.

Recent numerical study have shown that an octet truss lattice material of a relative density of 30% is free from any initial peak stress and exhibits the ideal engineering stress plateau of an energy absorption material prior to densification [Tancogne-Dejean 16]. We also show that the compressive response of the octet lattice material changes from an unstable shear mode to a stable buckling free mode at a relative density between 0.22 and 0.23. The underlying failure mechanism for lightweight octet lattice is still unclear. An equivalent and smart theoretical model is needed, which should be versatile enough to be applied to other truss lattices.

The deformation control and pathway guide of mechanical metamaterial is of great interest to many researchers. Previous works demonstrated how hierarchical architectures allow to extend the number of distinct reconfiguration steps [Coulais 18] and outlined a general design strategy for confined mechanical metamaterials [Florijn 14]. Up to date, no such study has focused on the stiffness task. How to combine the strategy to control flexible metamaterials and the demand to create high energy-absorption mechanical metamaterial constitutes another challenge.

# Appendix A
# Supplemental information

## A.1 Light-weight shell-lattice metamaterials for mechanical shock absorption

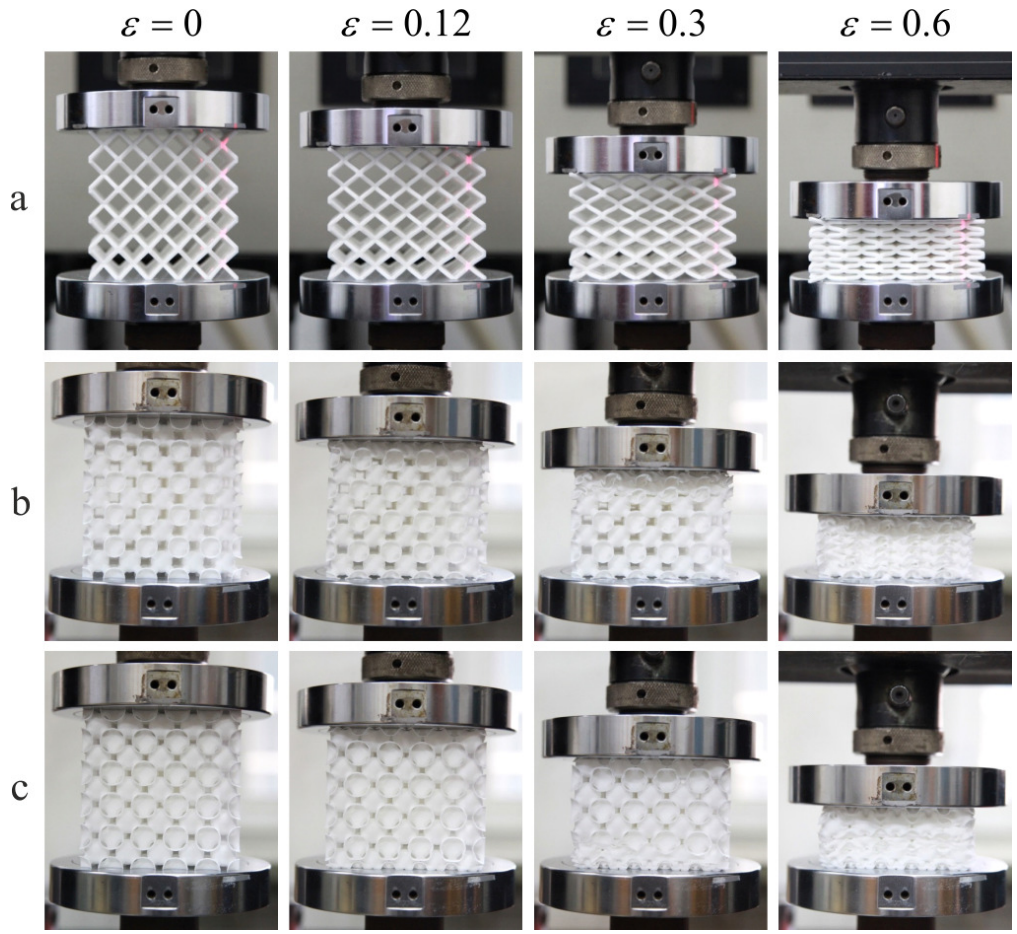


Figure A.1: Images corresponding to (a) TL, (b) SL1 and (c) SL2 metamaterials with a relative density of about 10% at different strains ranging from 0 to 0.6 (left to right).

## A.2 Effect of hole on mechanical properties

Additional simulations were then performed to investigate the effect of hole diameter (d=15$\mu$m) on the mechanical properties of closed tubular lattices. Figure A.2 shows that the introduction of holes will not significantly reduce both the elastic modulus and the yield strength for all considered relative densities. At low relative density, the elastic modulus and the yield strength respectively decrease by 9 % and 14 % for the [100] direction, and by about 7 % and 9 % for both the

[110] direction and the [111] direction. At high relative density, the influence of the holes on the elastic modulus remains unchanged, but are slightly suppressed on the yield strength. The yield strength decreases by 9 % for the [100] direction, by about 8 % for the [110] direction, and by 9 % for the [111] direction.

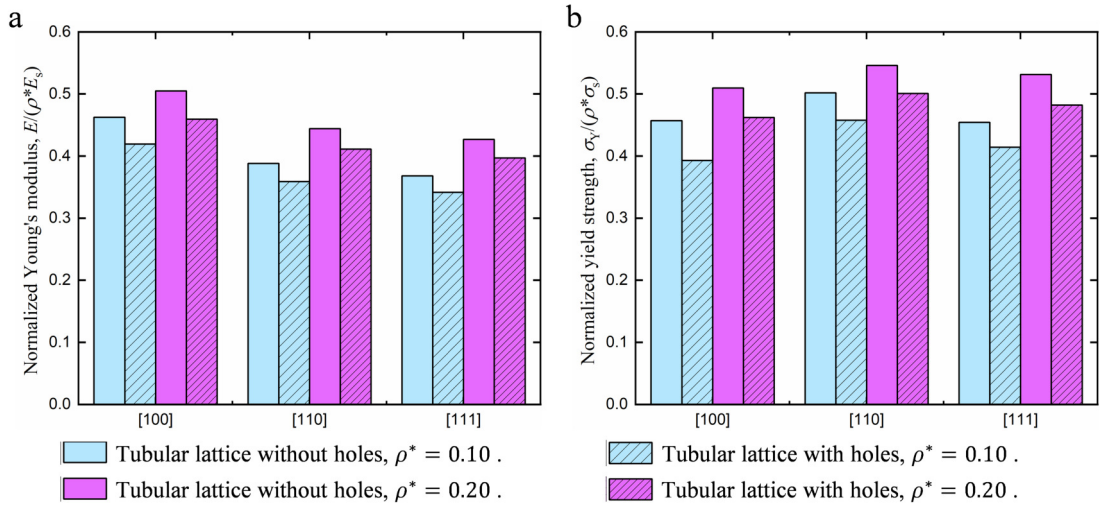


Figure A.2: Effect of holes (for a diameter d =15 $\mu$m) on the mechanical properties of the closed tubular lattice, for different relative densities.

## A.3 Elastic properties of bending-dominated lattice

### A.3.1 Compressive modulus and Poisson ratio of BCC lattice structures

Due to cubic symmetry, one strut of the unit cell is selected for further analysis, as shown in Figure A.3c. When the unit cell is under uniaxial compression, both ends of the micro-strut are able to move in the principal directions. Figure A.3c illustrates the deformation of the strut under compression. The strut can be considered as a clamped-clamped beam subjected to an axial force, a shear force and a bending moment. Based on Timoshenko's beam theory, and in a reference frame attached to the beam, the axial displacement $\delta_N$ and the shear deflection $\delta_S$ are given by

$$\delta_N = \frac{N l_e}{E_s A}, \tag{A.1}$$

$$\delta_S = \frac{S l_e^3}{12 E_s I}\left(1 + \frac{12 E_s I}{\kappa A G_s l_e^2}\right) = \frac{S k l_e^3}{12 E_s I}, \tag{A.2}$$

where $N$ and $S$ are the axial force and the shear force applied to the strut, $l_e$ is the effective length of the strut, $E_s$ is the elastic modulus of the strut material, $A = \pi R^2$ is the cross section area of the strut, $I = \pi R^4/4$ is the second moment of area of the beam, $G_s$ is the shear modulus of the strut material, and $\kappa$ is Timoshenko's shearing coefficient. The coefficient $k$ is introduced to incorporate both bending and shearing coupling effects.

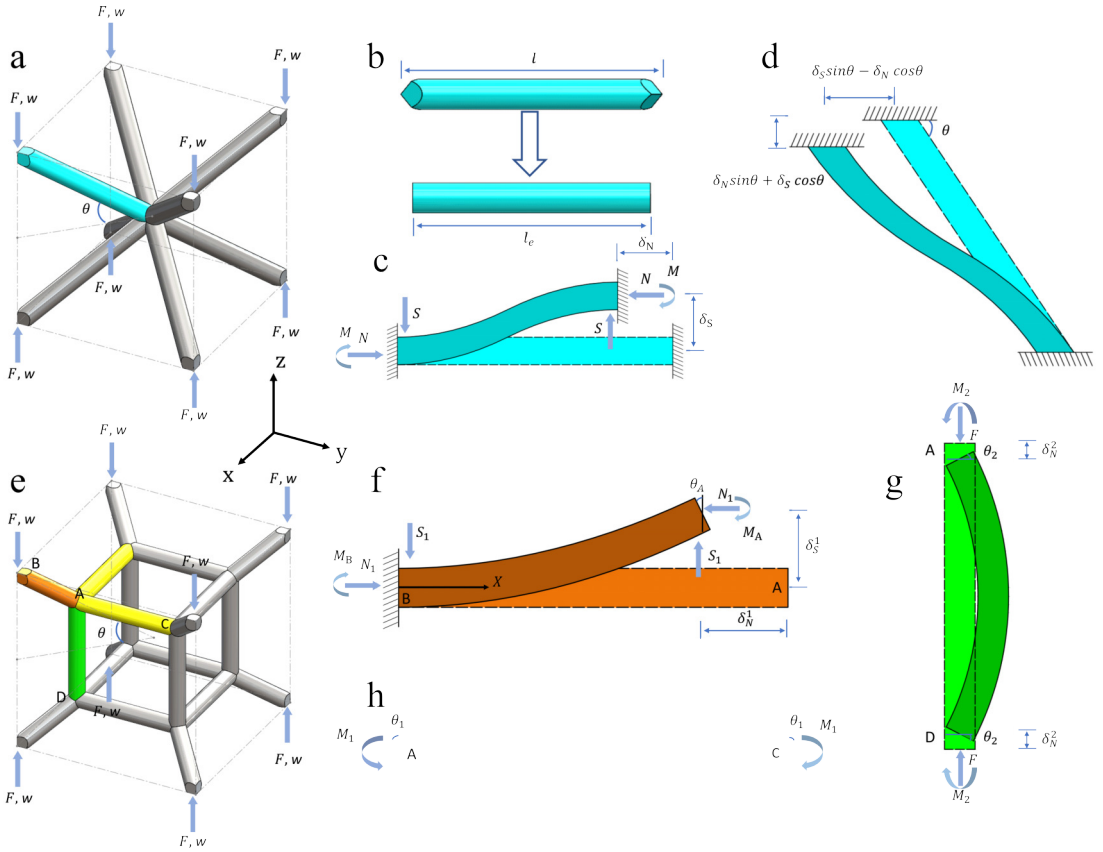


Figure A.3: Representative unit cells of a)BCC lattice and e) BCC-SC lattice under uniaxial compression. b) Effective model for irregular strut. c)- g) The corresponding simplied mechanical beam model.

For a circular strut, $\kappa$ is obtained by the following expression [Hutchinson 01]

$$\kappa = \frac{6\,(1+\nu_s)^2}{7+12\nu_s+4\nu_s^2}, \tag{A.3}$$

where $\nu_s$ is Poisson's ratio of the strut material. For an isotropic material, we further have

$$\frac{E_s}{2G_s\,(1+\nu_s)} = 1. \tag{A.4}$$

As a result, the above equations lead to

$$\delta_N = \frac{Nl_e}{\pi E_s R^2}, \tag{A.5}$$

$$\delta_S = \frac{kSl_e^3}{3\pi E_s R^4}, \tag{A.6}$$

$$k = 1 + \frac{7 + 12\nu_s + 4v_s^2}{1 + \nu_s}\left(\frac{R}{l_e}\right)^2. \tag{A.7}$$

The forces $N$ and $S$ originate from a global force $F$ oriented along direction [001]:

$$N = F\sin\theta, \tag{A.8}$$

$$S = F\cos\theta, \tag{A.9}$$

with $\sin\theta = 1/\sqrt{3}$ and $\cos\theta = \sqrt{2/3}$. $\theta$ is the angle between directions [110] and [001]. The global displacements $u$, $v$ and $w$ of the unit cell in the $x$, $y$ and $z$ directions, respectively, can then be expressed as

$$u = v = \frac{1}{\sqrt{2}}\left(\delta_S\sin\theta - \delta_N\cos\theta\right) = \frac{1}{3}\left(\frac{kFl_e^3}{3\pi E_s R^4} - \frac{Fl_e}{\pi E_s R^2}\right), \tag{A.10}$$

$$w = -\left(\delta_S\cos\theta + \delta_N\sin\theta\right) = -\frac{1}{3}\left(\frac{2kFl_e^3}{3\pi E_s R^4} + \frac{Fl_e}{\pi E_s R^2}\right). \tag{A.11}$$

The effective Young's modulus $E$ and Poisson's ratio $\nu$ of the BCC lattice material, therefore, are given by

$$E = \frac{\sigma_z}{\varepsilon_z} = \frac{\frac{-4F}{L^2}}{\frac{2w}{L}} = \frac{9\sqrt{3}\pi E_s}{3 + 2k\left(\frac{l_e}{R}\right)^2}\frac{R^2}{l_e l}, \tag{A.12}$$

$$\nu = -\frac{u}{w} = \frac{k - 3\left(\frac{R}{l_e}\right)^2}{2k + 3\left(\frac{R}{l_e}\right)^2}. \tag{A.13}$$

The expression for Young's modulus considers the mid-plane symmetry of the BCC unit cell, so that the force $F$ is distributed over 4 struts (hence the vertical stress is expressed as $\sigma_z = -4F/L^2$) and the strain is symmetrical with respect to the cell center (hence $\varepsilon_z = 2w/L$).

### A.3.2 [100] Shear modulus of BCC lattice

Consider the BCC unit cell sketched in Figure A.4a with an applied shear displacement. The strut can also be treated as a clamped-clamped beam. The local displacement $\delta_N$ and $\delta_S$, and the corresponding force $N$ and $S$, are related to the global shear displacement $u$ and global force $F$ via

$$\delta_N = \sqrt{2}u\cos\theta = \frac{2}{\sqrt{3}}u, \tag{A.14}$$

$$\delta_S = \sqrt{2}u\sin\theta = \frac{\sqrt{2}}{\sqrt{3}}u, \tag{A.15}$$

$$N\cos\theta + S\sin\theta = \sqrt{2}F. \tag{A.16}$$

By substituting Equation A.5, Equation A.6, Equation A.14 and Equation A.15 into Equation A.16, we obtain

$$F = \left(\frac{2\pi E_s R^2}{l_e} + \frac{3\pi E_s R^4}{k l_e^3}\right)\frac{u}{3}. \tag{A.17}$$

Therefore, the effective shear modulus of BCC lattice is

$$G = \frac{\tau}{\gamma} = \frac{\frac{F}{L^2}}{\frac{u}{L}} = \frac{\pi E_s}{3}\left(2 + \frac{3}{k}\left(\frac{R}{l_e}\right)^2\right)\frac{R^2}{l_e L}. \tag{A.18}$$

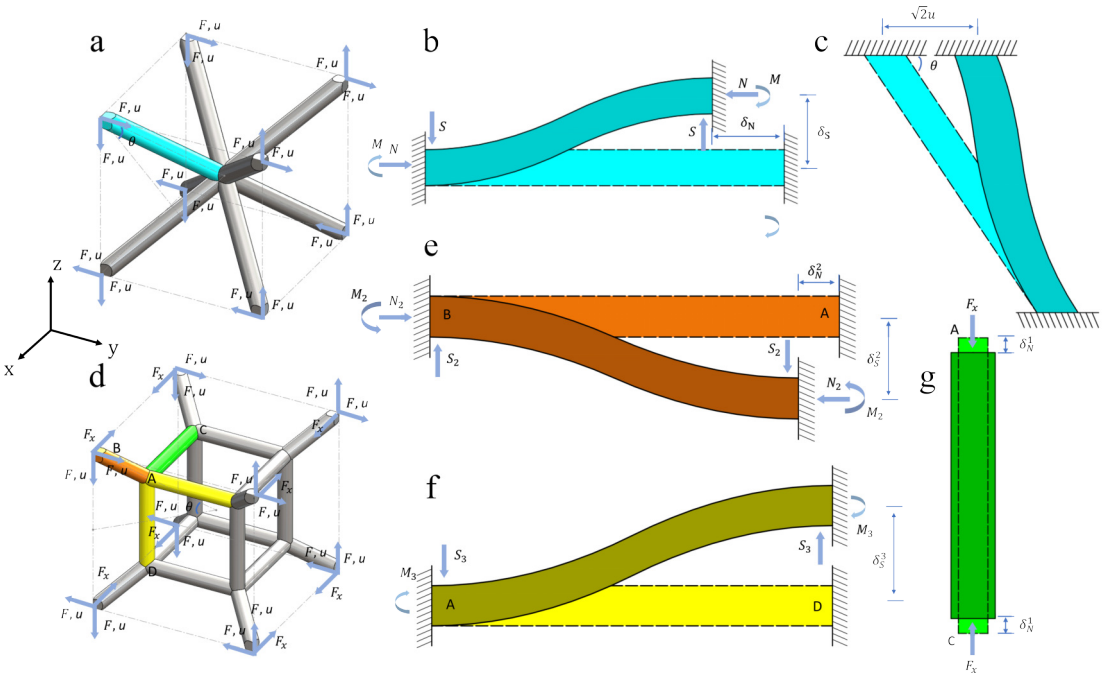


Figure A.4: (a)-(c) Deformation of struts in BCC unit models under pure shear loading.(d)-(g) Three different representive simplied beam models for BCC-SC lattice subjecting to pure shearing force.

### A.3.3 Bulk modulus of BCC lattice

Under hydrostatic pressure, the standard strut can again be considered a clamped-clamped beam subjected to an axial force. Based on Timoshenko's beam theory, we have

$$\delta = \frac{N l_e}{E_s A}. \tag{A.19}$$

The global force $F$ and the displacement $u$ are given by

$$N = \sqrt{3}F, \tag{A.20}$$

$$\delta = \sqrt{3}u. \tag{A.21}$$

We get an analytical expression for the bulk modulus from the definition

$$K = -\frac{dP}{dV/V} = \frac{2\pi E_s R^2}{l_e L\left(3 - 6\frac{u}{L} + 4\frac{u^2}{L^2}\right)}, \tag{A.22}$$

with $dP = 4F/L^2$, $V = L^3$, and $dV = L^3 - (L - 2u)^3$. Noting that $u \ll L$, we simply have

$$K \approx \frac{2\pi E_s R^2}{3 l_e L}. \tag{A.23}$$

### A.3.4 Compressive modulus and Poisson ratio of BCC-SC lattie

Different from the BCC lattice, when under compression the struts of the BCC-SC lattice can not be simply considered as clamped-clamped beams. As sketched in Figure A.3e, struts can be divided into three types, labeled AB, AC or AD according to their deformation behavior. Strut AB can be considered as a clamped-free beam (A is free and B is clamped) subjected to an axial force, a shear force and a bending moment. Based on the moment balance principle of statics,

$$M_A + M_B = S_1 l_1, \tag{A.24}$$

$$M\left(x\right) = S_1 l_1 - M_A - S_1 x. \tag{A.25}$$

It follows that $M_A = -M(l_1)$ and $M_B = M(0)$. The relative rotation between the ends of the beam sketched in Figure A.3f is calculated from the beam equation

$$\theta_A = \int_0^{l_1} \frac{M\left(x\right)}{E_s I} dx = \frac{l_1}{E_s I}\left(\frac{S_1 l_1}{2} - M_A\right). \tag{A.26}$$

Strut AC is only subject to a constant bending moment $M_1$ and thus the relative rotation at point A is given by

$$\theta_1 = \frac{M_1 l_2}{2E_s I}. \tag{A.27}$$

Strut AD is subject to a constant bending moment $M_2$ and an axial force $F$ and thus the relative rotation at point A is given by

$$\theta_2 = \frac{M_2 l_2}{2E_s I}. \tag{A.28}$$

Due to the fact that all struts are connected at a same rigid joint $A$, they must experience the same rotation and moment balance

$$\theta_A = \theta_2 = \sqrt{2}\theta_1, \tag{A.29}$$

$$M_A = M_2 + \sqrt{2}M_1. \tag{A.30}$$

Substituting these beam equations into the balance equations,

$$M_A = k_1 S_1 l_1, \tag{A.31}$$

$$k_1 = \frac{2l_1}{l_2 + 4l_1}. \tag{A.32}$$

We have, by Timoshenko's beam theory

$$\delta_N^1 = \frac{N_1 l_1}{E_s A}, \tag{A.33}$$

$$\delta_S^1 = \frac{k_2 S_1 l_1^3}{E_s I}, \tag{A.34}$$

$$k_2 = \frac{2 - 3k_1}{6} + \frac{E_s I}{\kappa A G_s l_1^2}, \tag{A.35}$$

$$\delta_N^2 = \frac{F l_1}{2E_s A}. \tag{A.36}$$

Thus, the relationship between global displacement and global force is

$$u_1 = v_1 = \frac{1}{\sqrt{2}}\left(\delta_S^1 \sin\theta - \delta_N^1 \cos\theta\right) = \frac{1}{3}\left(\frac{k_2 F l_1^3}{E_s I} - \frac{F l_1}{E_s A}\right), \tag{A.37}$$

$$w_1 = -\left(\delta_S^1 \cos\theta + \delta_N^1 \sin\theta + 2\delta_N^2\right) = -\frac{1}{3}\left(\frac{4k_2 F l_1^3}{E_s I} + \frac{2F l_1}{E_s A} + \frac{3F l_2}{E_s A}\right). \tag{A.38}$$

The effective Young's modulus and Poisson's ratio of the BCC-SC lattice are finally obtained as

$$E = \frac{\sigma_z}{\varepsilon_z} = \frac{\frac{-4F}{L^2}}{\frac{w_1}{L}} = \frac{12\pi E_s}{3 + \frac{2l_1}{l_2} + 16k_2\left(\frac{l_1}{R}\right)^2 \frac{l_1}{l_2}} \left(\frac{R}{l_2}\right)^2 \frac{l_2}{L}, \tag{A.39}$$

$$\nu = -\frac{2u_1}{w_1} = \frac{\frac{8k_2 l_1^2}{R^2} - 2}{2 + \frac{16k_2 l_1^2}{R^2} + \frac{3l_2}{l_1}}. \tag{A.40}$$

### A.3.5 [100] Shear modulus of BCC-SC lattice

Figure A.4 illustrates the way micro-struts deform under a pure shear displacement. For strut AB, only axial displacement occurs during deformation, thus

$$F_x = \frac{2E_s A\delta_N^1}{l_2}. \tag{A.41}$$

Strut AC can be considered as a beam with clamped-clamped boundary conditions and by virtue of Timoshenko's beam theory we have

$$\delta_N^2 = \frac{N_2 l_1}{E_s A}, \tag{A.42}$$

$$\delta_S^2 = \frac{k_3 S_2 l_1^3}{12E_s I}, \tag{A.43}$$

$$k_3 = 1 + \frac{7 + 12\nu_s + 4\nu_s^2}{1 + \nu_s}\left(\frac{R}{l_1}\right)^2. \tag{A.44}$$

The strut force and displacement can be expressed in terms of the macroscopic force and displacement as

$$N_2 = \sqrt{2}F\cos\theta + F_x \sin\theta = \frac{2F}{\sqrt{3}} + \frac{F_x}{\sqrt{3}}, \tag{A.45}$$

$$S_2 = \sqrt{2}F\sin\theta - F_x\cos\theta = \frac{\sqrt{2}F}{\sqrt{3}} - \frac{\sqrt{2}F_x}{\sqrt{3}}, \tag{A.46}$$

$$\delta_N^2 = \sqrt{2}u\cos\theta - \delta_N^1\sin\theta = \frac{2u}{\sqrt{3}} - \frac{\delta_N^1}{\sqrt{3}}, \tag{A.47}$$

$$\delta_S^2 = \sqrt{2}u\sin\theta + \delta_N^1\cos\theta = \frac{\sqrt{2}u}{\sqrt{3}} + \frac{\sqrt{2}\delta_N^1}{\sqrt{3}}. \tag{A.48}$$

Those equations lead to

$$u - \left(\frac{1}{2} + \frac{l_1}{l_2}\right)\delta_N^1 = \frac{l_1}{A}\frac{F}{E}, \tag{A.49}$$

$$u + \left(1 + \frac{k_3 l_1^3 A}{6Il_2}\right)\delta_N^1 = \frac{k_3 l_1^3}{12I}\frac{F}{E}. \tag{A.50}$$

Solving those equations, we get

$$u = \frac{k_4 F l_1}{E\pi R^2}, \tag{A.51}$$

$$k_4 = \frac{1 + k_3\left(\frac{1}{6} + \frac{l_1}{l_2}\right)\left(\frac{l_1}{R}\right)^2}{\frac{3}{2} + \left(1 + \frac{2}{3}k_3\left(\frac{l_1}{R}\right)^2\right)\frac{l_1}{l_2}}. \tag{A.52}$$

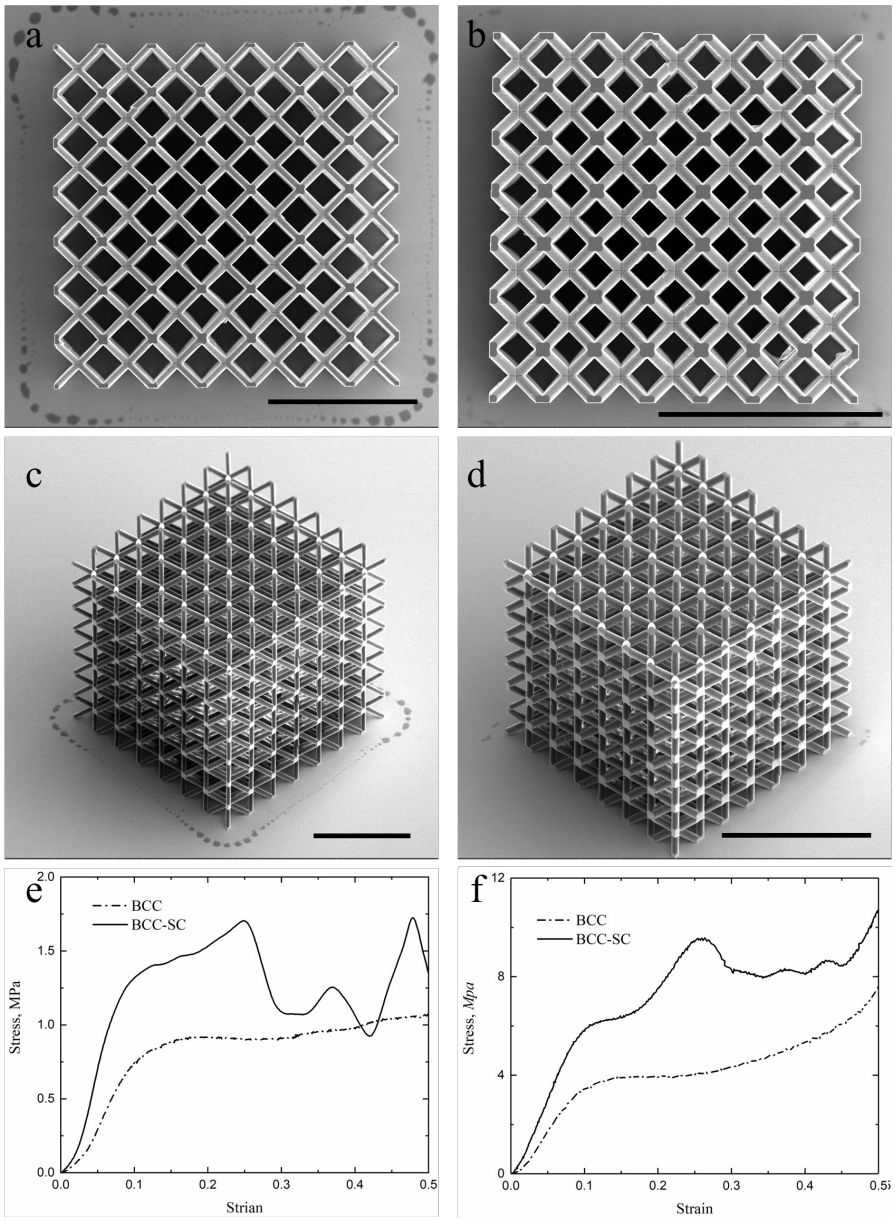


Figure A.5: BCC truss micro-lattice samples fabricated via direct laser writing technology. (a–b) Top views and (c–d) isometric views of [100] and [110] truss-lattice samples with relative density 0.05 and 0.1, respectively. (e–f) Engineering stress-strain curves of BCC-SC and BCC micro-lattice samples along the [100] direction. Under compression, both the elastic modulus and the SEA of BCC-SC lattice samples are always found to be about 1.7 times larger than those of the BCC lattice samples, which is very close to the simulation results, 2 and 1.67. Scale bar lengths are 300 $\mu$m.

Strut AD is subject to a shear force and a bending moment. Its deflection is given

by

$$\delta_S^3 = \frac{k_5 S l_2^3}{3\pi E_s R^4}, \tag{A.53}$$

$$k_5 = 1 + \frac{7 + 12\nu_s + 4\nu_s^2}{1 + \nu_s}\left(\frac{R}{l_2}\right)^2. \tag{A.54}$$

Finally, the effective shear modulus is given by

$$G = \frac{\tau}{\gamma} = \frac{\frac{4S}{L^2}}{\frac{2\left(2u + \delta_S^3\right)}{L}} = \frac{2\pi E_s}{2k_4 + \frac{k_5}{3}\left(\frac{l_2}{R}\right)^2 \frac{l_2}{l_1}}\left(\frac{R}{l_1}\right)^2 \frac{l_1}{L}. \tag{A.55}$$

#### A.3.5.a Bulk modulus of BCC-SC lattice

Thereafter, the bulk modulus can be also obtained via a function of Young's modulus and shear modulus as follow

$$K = \frac{E}{3\left(1 - 2\upsilon\right)} \tag{A.56}$$

### A.3.6 Poisson's ratio

Special attention was paid in the main text on the elastic isotropic lattice with relative density of 0.01. Here, we adopt the method described in our previous work to obtain the effective Poisson's ratio from digital image correlation (DIC) images of compressive experiments [Chen 20b]. The measured Poisson's ratio for the [100] and [110] samples are 0.497 and 0.488, respectively. Those values are close to the simulation result of 0.495, thus verifying our design. This value of the effective Poisson's ratio leads to a fairly large ratio of bulk modulus to shear modulus of about $K/G = 90.6$, making the elastically isotropic BCC-SC lattice an interesting structural basis in the field of transformation elastodynamics.

## A.4 Optimal isotropic, reusable truss lattice material with near-zero Poisson's ratio

| $r_1(\mu m)$ | $r_2(\mu m)$ | $r_3(\mu m)$ | $r_4(\mu m)$ | $v_{s1}(\mu m/s)$ | $v_{s2}(\mu m/s)$ | $v_L(\mu m/s)$ |
|---|---|---|---|---|---|---|
| 14.848 | 4.566 | 5.232 | 3.333 | 221.5465324 | 267.7280693 | 372.3135116 |
| 15.01 | 4.02 | 5.697 | 3.535 | 202.3732751 | 277.3469089 | 369.8477121 |
| 15.737 | 5.475 | 5.616 | 3.818 | 241.4262079 | 287.4988942 | 404.7687646 |
| 15.838 | 4.242 | 5.03 | 3.576 | 202.3710537 | 265.5510571 | 362.4280992 |

| | | | | | | |
|---|---|---|---|---|---|---|
| 15.071 | 5.354 | 4.687 | 2.889 | 238.7382643 | 246.6910231 | 364.4051816 |
| 15.333 | 4.808 | 4.061 | 3.556 | 216.5838332 | 263.2851873 | 373.8907347 |
| 14.727 | 4.828 | 5.273 | 2.667 | 231.2742225 | 239.0714804 | 349.3660261 |
| 14 | 5.455 | 5.576 | 2.444 | 241.159635 | 256.7541508 | 368.1372025 |
| 14.121 | 4.485 | 5.152 | 3.152 | 225.2541174 | 265.6843436 | 371.4249352 |
| 14.929 | 4.525 | 5.899 | 3.01 | 221.0178294 | 257.0651525 | 358.0740748 |
| 14.02 | 5.515 | 4.444 | 2.747 | 248.6236767 | 249.6455396 | 373.5130897 |
| 14.828 | 4.646 | 4.586 | 3.838 | 220.9311932 | 283.8335166 | 395.2832115 |
| 14.444 | 4.04 | 5.111 | 3.677 | 207.1116088 | 284.5443777 | 383.6650751 |
| 14.04 | 5.172 | 5.374 | 3.172 | 247.2241689 | 272.6596683 | 391.2624033 |
| 14.99 | 5.636 | 5.778 | 3.657 | 252.4667697 | 290.2979099 | 412.4993793 |
| 15.596 | 5.556 | 5.01 | 3.354 | 241.3817791 | 266.2397039 | 385.1090118 |
| 14.222 | 5.596 | 4.121 | 3.434 | 244.7805838 | 275.2365399 | 400.237025 |
| 15.556 | 5.131 | 4.081 | 2.909 | 223.0771052 | 236.9166827 | 347.9887327 |
| 15.758 | 5.01 | 5.737 | 2.263 | 216.1928596 | 229.7414282 | 327.7514051 |
| 14.505 | 5.677 | 4.101 | 2.283 | 221.6331686 | 244.6695117 | 346.8557977 |
| 15.818 | 5.152 | 4.848 | 2.788 | 228.6751365 | 235.3838884 | 346.7447257 |
| 14.141 | 4.424 | 4.525 | 2.202 | 208.2134435 | 221.3132811 | 316.1776975 |
| 15.98 | 4.364 | 5.475 | 2.424 | 207.1738091 | 210.6192641 | 307.4696488 |
| 14.808 | 5.313 | 4 | 3.071 | 232.384943 | 251.4671212 | 368.6037051 |
| 15.03 | 5.333 | 4.505 | 3.616 | 236.3613224 | 275.9696154 | 394.9499954 |
| 14.525 | 5.535 | 5.131 | 2.707 | 247.823958 | 251.4671212 | 371.9358666 |
| 15.172 | 4.626 | 5.434 | 2.061 | 200.2917849 | 222.2107432 | 309.0913007 |
| 15.152 | 5.758 | 5.071 | 3.919 | 249.8454693 | 294.0077164 | 419.2525599 |
| 15.232 | 4.061 | 4.788 | 3.172 | 200.4872717 | 250.7340457 | 345.1675026 |
| 15.778 | 5.717 | 5.515 | 2.162 | 215.3420477 | 247.9794588 | 341.3021952 |
| 15.273 | 5.293 | 5.172 | 2.323 | 218.1188489 | 239.426911 | 337.281387 |
| 15.636 | 4.667 | 4.566 | 3.98 | 214.6156365 | 280.9234289 | 390.6403999 |
| 14.97 | 5.798 | 4.707 | 2.242 | 221.7620121 | 250.4674728 | 349.8325287 |
| 14.162 | 4.283 | 5.293 | 2.384 | 219.1495975 | 222.0574638 | 324.8635318 |
| 15.657 | 5.879 | 4.949 | 2.646 | 238.4939058 | 248.3571038 | 362.9390306 |
| 15.253 | 4.101 | 4.242 | 3.737 | 198.9033843 | 269.5718654 | 371.6692937 |
| 14.889 | 5.939 | 5.051 | 3.232 | 256.5097923 | 270.8380867 | 398.5487298 |
| 15.879 | 4.343 | 4.283 | 3.374 | 201.4780344 | 250.1342566 | 349.6770278 |
| 14.101 | 4.444 | 4.343 | 2.97 | 220.3291827 | 282.5672952 | 357.0966408 |
| 14.909 | 4.869 | 5.838 | 3.717 | 232.0961557 | 289.9202649 | 399.3484486 |
| 15.051 | 6 | 5.394 | 2.525 | 238.0940464 | 260.0196691 | 369.5811392 |
| 15.697 | 5.374 | 4.465 | 2.182 | 204.6969024 | 232.384943 | 322.597662 |
| 15.414 | 4.586 | 4.323 | 2 | 186.4855291 | 213.3982868 | 293.3190696 |
| 14.747 | 5.576 | 5.495 | 2.02 | 212.7785047 | 253.2664884 | 342.7905607 |
| 15.394 | 4.788 | 4.768 | 3.293 | 221.448789 | 257.9759433 | 365.2715436 |
| 14.465 | 4 | 5.596 | 2.949 | 206.2874541 | 253.9329207 | 346.3670807 |
| 14.242 | 5.616 | 4.828 | 2.121 | 217.8078472 | 254.2439225 | 348.4552353 |
| 14.081 | 4.525 | 4.606 | 3.697 | 224.2100401 | 285.8772423 | 397.4380093 |
| 15.717 | 4.162 | 5.677 | 3.071 | 202.0467233 | 249.4456099 | 340.6357629 |

| | | | | | | |
|---|---|---|---|---|---|---|
| 15.96 | 4.707 | 4.303 | 2.485 | 211.4012113 | 211.6700057 | 314.6226888 |
| 15.212 | 4.687 | 4.727 | 2.566 | 220.3580614 | 224.5654707 | 330.7059217 |
| 15.859 | 4.384 | 4.869 | 2.848 | 206.3496545 | 232.0517269 | 329.0620553 |
| 15.172 | 4.222 | 5.071 | 3.899 | 207.1449304 | 285.9216711 | 387.5303825 |
| 15.293 | 4.99 | 5.212 | 3.859 | 230.1412876 | 287.2323213 | 399.9038088 |
| 14.626 | 5.919 | 4.525 | 3.798 | 252.5334129 | 291.0531998 | 420.3188516 |
| 15.434 | 4.404 | 5.98 | 2.465 | 213.2116857 | 225.9649785 | 323.9083122 |
| 14.182 | 5.737 | 4.889 | 3.313 | 256.7763652 | 277.7245538 | 405.4129825 |
| 14.303 | 5.253 | 4.626 | 3.879 | 241.759424 | 294.0521452 | 416.4979731 |
| 14.788 | 4.303 | 4.202 | 2.364 | 208.8754329 | 209.3908072 | 310.135378 |
| 14.404 | 5.818 | 5.313 | 3.939 | 259.2199503 | 304.1819161 | 433.069923 |
| 15.475 | 4.768 | 5.414 | 2.828 | 223.4325358 | 241.3817791 | 346.6336536 |
| 15.111 | 4.141 | 5.354 | 2.687 | 205.8698232 | 233.2290906 | 327.1738305 |
| 14.687 | 5.273 | 5.172 | 3.515 | 242.9145734 | 280.390283 | 398.6820163 |
| 14.485 | 4.889 | 4.04 | 3.596 | 225.6539768 | 273.614888 | 389.4408217 |
| 15.455 | 4.202 | 4.222 | 2.768 | 200.4894931 | 225.3874039 | 321.4202983 |
| 16 | 5.071 | 4.485 | 3.455 | 221.8264339 | 258.6423756 | 368.9147069 |
| 14.566 | 5.778 | 5.919 | 2.586 | 250.156471 | 261.152604 | 379.2221931 |
| 14.364 | 4.949 | 4.162 | 2.505 | 227.0090558 | 230.4078605 | 341.1911232 |
| 14.283 | 4.465 | 5.818 | 3.495 | 224.1656113 | 285.2552388 | 388.4856021 |
| 15.576 | 4.505 | 5.717 | 3.758 | 214.6578438 | 282.8782969 | 383.7539328 |
| 15.495 | 5.111 | 5.96 | 3.273 | 234.6952417 | 267.9057846 | 378.1781158 |
| 15.354 | 5.838 | 4.182 | 2.626 | 234.2953823 | 241.3373502 | 356.6079237 |
| 15.374 | 5.657 | 6 | 2.606 | 241.4928511 | 252.1335535 | 365.4492589 |
| 15.919 | 4.929 | 5.333 | 3.414 | 223.9434672 | 263.9516196 | 370.7585029 |
| 14.949 | 5.071 | 5.879 | 2.404 | 230.05243 | 238.560549 | 345.2341458 |
| 15.131 | 5.394 | 5.455 | 2.99 | 244.1585803 | 256.7763652 | 374.8681688 |
| 15.939 | 5.697 | 4.384 | 3.03 | 235.9836774 | 246.6910231 | 364.9827563 |
| 15.798 | 4.848 | 4.99 | 2.101 | 196.5619854 | 221.9241773 | 306.8476453 |
| 14.707 | 5.03 | 4.747 | 2.141 | 207.4936966 | 234.8729569 | 325.4188921 |
| 15.616 | 5.495 | 4.02 | 3.636 | 229.2749256 | 268.2834296 | 386.6862349 |
| 15.313 | 5.98 | 4.424 | 3.394 | 247.068668 | 269.4385789 | 394.927781 |
| 15.515 | 5.96 | 5.657 | 3.212 | 255.9100032 | 269.4385789 | 395.038853 |
| 14.646 | 5.899 | 4.404 | 2.929 | 251.3116203 | 255.2213565 | 382.2211385 |
| 14.061 | 4.97 | 4.97 | 2.525 | 236.45018 | 240.1599865 | 353.3424055 |
| 14.525 | 4.081 | 4.364 | 3.475 | 205.3811062 | 267.6836405 | 369.4478527 |
| 14.263 | 5.232 | 5.758 | 3.778 | 247.7351003 | 299.894535 | 418.49727 |
| 14.606 | 4.182 | 4.808 | 2.808 | 210.0727896 | 239.8934136 | 338.036677 |
| 14.343 | 4.909 | 5.535 | 2.04 | 208.5377739 | 238.560549 | 327.4848322 |
| 14.384 | 4.727 | 5.253 | 3.96 | 230.3856461 | 299.9833926 | 412.5882369 |
| 14.667 | 4.323 | 5.859 | 2.303 | 216.7571056 | 221.1999876 | 321.7535144 |
| 14.202 | 4.747 | 5.798 | 2.727 | 234.6508128 | 250.3119719 | 360.0289429 |
| 15.071 | 5.172 | 4.141 | 2.343 | 211.4678546 | 229.3859977 | 326.8183999 |
| 14.869 | 4.606 | 4.263 | 3.051 | 217.3702233 | 246.8465239 | 353.2757622 |
| 14.586 | 5.212 | 5.939 | 3.111 | 245.3137296 | 269.2164348 | 385.286727 |

| | | | | | | |
|---|---|---|---|---|---|---|
| 15.535 | 4.121 | 4.909 | 2.222 | 198.761212 | 200.9671029 | 293.6300714 |
| 15.677 | 5.434 | 4.667 | 4 | 234.6952417 | 286.454817 | 406.2127013 |
| 14.424 | 5.051 | 4.646 | 3.131 | 236.3168936 | 260.7971734 | 376.4676063 |
| 15.899 | 5.414 | 5.556 | 2.869 | 238.8715507 | 246.0690196 | 361.5173083 |
| 14.768 | 4.263 | 4.929 | 2.081 | 197.2839538 | 212.3764239 | 299.894535 |
| 14.323 | 5.859 | 5.636 | 3.253 | 263.3962594 | 280.1014957 | 409.0561457 |

Table A.1: Generated sample points and the corresponding wave velocity.

| Sample | $(x_1, y_1)$ | $(x_2, y_2)$ | $(x_3, y_3)$ | $(x_4, y_4)$ | $(x_1^{'}, y_1^{'})$ | $(x_2^{'}, y_2^{'})$ | $(x_3^{'}, y_3^{'})$ | $(x_4^{'}, y_4^{'})$ | $\upsilon$ |
|---|---|---|---|---|---|---|---|---|---|
| 100 | (955, 1091) | (1390, 1088) | (958, 1520) | (1393, 1517) | (955.262, 1093.368) | (1390.359, 1091.36) | (957.88,1520.803) | (1392.946,1517.93) | 0.0408 |
| 110 | (1099, 965) | (1456, 965) | (1099, 1319) | (1459, 1319) | (1099.793, 969.518) | (1456.573, 973.821) | (1099.027, 1321.176) | (1458.831, 1321.2) | 0.0697 |

Table A.2: Measured coordinates of speckles and calculated Poisson's ratio

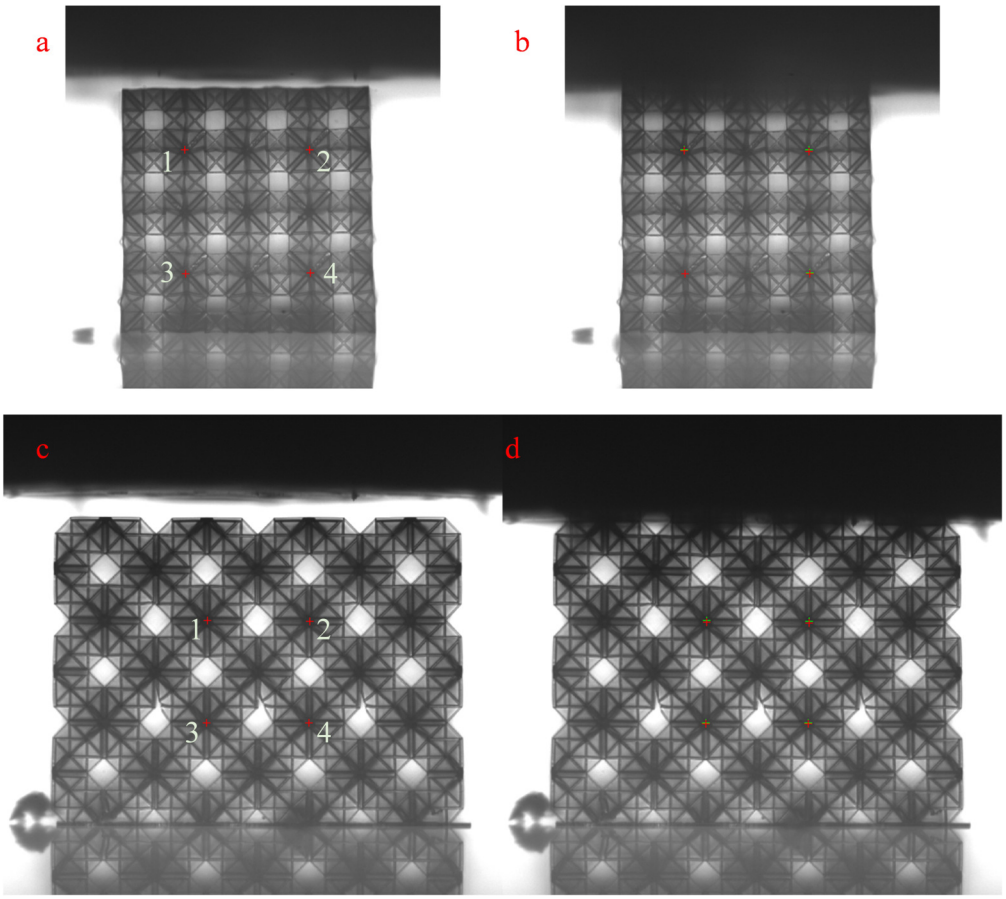


Figure A.6: Measured process by DIC: (a) [100] sample and (c) [110] sample selected points at Initial position (b) and (d) displacements of selected points when small elastic strain occurs (green stars and red stars are respectively non defromation and deformation coordinates. At initial position, green stars were overlapped by red stars.

# Bibliography

[Babaee 13] S. Babaee, J. Shim, J. C. Weaver, E. R. Chen, N. Patel & K. Bertoldi. *3D soft metamaterials with negative Poisson's ratio*. Advanced Materials, vol. 25, no. 36, pages 5044–5049, 2013.

[Babaee 16] S. Babaee, N. Viard, P. Wang, N. X. Fang & K. Bertoldi. *Acoustic Switches: Harnessing Deformation to Switch On and Off the Propagation of Sound*. Nature Reviews Materials, vol. 28, no. 8, pages 1630–1630, 2016.

[Bartlett 15] N. W. Bartlett, M. T. Tolley, J. T. Overvelde, J. C. Weaver, B. Mosadegh, K. Bertoldi, G. M. Whitesides & R. J. Wood. *A 3D-printed, functionally graded soft robot powered by combustion*. Science, vol. 349, no. 6244, pages 161–165, 2015.

[Berger 17] J. Berger, H. Wadley & R. McMeeking. *Mechanical metamaterials at the theoretical limit of isotropic elastic stiffness*. Nature, vol. 543, no. 7646, pages 533–537, 2017.

[Bertoldi 10] K. Bertoldi, P. M. Reis, S. Willshaw & T. Mullin. *Negative Poisson's ratio behavior induced by an elastic instability*. Advanced materials, vol. 22, no. 3, pages 361–366, 2010.

[Bishop 91] C. Bishop. *Improving the generalization properties of radial basis function neural networks*. Neural computation, vol. 3, no. 4, pages 579–588, 1991.

[Blasco 16] E. Blasco, J. Müller, P. Müller, V. Trouillet, M. Schön, T. Scherer, C. Barner-Kowollik & M. Wegener. *Fabrication of conductive 3D gold-containing microstructures via direct laser writing*. Advanced Materials, vol. 28, no. 18, pages 3592–3595, 2016.

[Bonatti 17a] C. Bonatti & D. Mohr. *Large deformation response of additively-manufactured FCC metamaterials: From octet truss lattices towards continuous shell mesostructures*. International Journal of Plasticity, vol. 92, pages 122–147, 2017.

[Bonatti 17b] C. Bonatti & D. Mohr. *Large deformation response of additively-manufactured FCC metamaterials: From octet truss lattices towards continuous shell mesostructures*. International Journal of Plasticity, vol. 92, pages 122–147, 2017.

[Bonatti 19a] C. Bonatti & D. Mohr. *Mechanical performance of additively-manufactured anisotropic and isotropic smooth shell-lattice materials: Simulations & experiments*. Journal of the Mechanics and Physics of Solids, vol. 122, pages 1–26, 2019.

[Bonatti 19b] C. Bonatti & D. Mohr. *Smooth-shell metamaterials of cubic symmetry: Anisotropic elasticity, yield strength and specific energy absorption*. Acta Materialia, vol. 164, pages 301–321, 2019.

[Bonatti 19c] C. Bonatti & D. Mohr. *Smooth-shell metamaterials of cubic symmetry: Anisotropic elasticity, yield strength and specific energy absorption*. Acta Materialia, vol. 164, pages 301–321, 2019.

[Bower 09] A. F. Bower. Applied mechanics of solids. CRC press, 2009.

[Bückmann 12] T. Bückmann, N. Stenger, M. Kadic, J. Kaschke, A. Frölich, T. Kennerknecht, C. Eberl, M. Thiel & M. Wegener. *Tailored 3D mechanical metamaterials made by dip-in direct-laser-writing optical lithography*. Advanced Materials, vol. 24, no. 20, pages 2710–2714, 2012.

[Bückmann 14] T. Bückmann, R. Schittny, M. Thiel, M. Kadic, G. W. Milton & M. Wegener. *On three-dimensional dilational elastic metamaterials*. New journal of physics, vol. 16, no. 3, page 033032, 2014.

[Cabras 16] L. Cabras & M. Brun. *A class of auxetic three-dimensional lattices*. Journal of the Mechanics and Physics of Solids, vol. 91, pages 56–72, 2016.

[Carta 16] G. Carta, M. Brun & A. Baldi. *Design of a porous material with isotropic negative Poisson's ratio*. Mechanics of materials, vol. 97, pages 67–75, 2016.

[Chen 20a] X. Chen, Q. Ji, J. Wei, H. Tan, J. Yu, P. Zhang, V. Laude & M. Kadic. *Light-weight shell-lattice metamaterials for mechanical shock absorption*. International Journal of Mechanical Sciences, vol. 169, page 105288, 2020.

[Chen 20b] X. Chen, J. Moughames, Q. Ji, J. A. I. Martínez, H. Tan, S. Adrar, N. Laforge, J.-M. Cote, S. Euphrasie, G. Ulliac*et al. Optimal isotropic, reusable truss lattice material with near-zero Poisson's ratio.* Extreme Mechanics Letters, vol. 41, page 101048, 2020.

[Chen 20c] Y. Chen, T. Frenzel, S. Guenneau, M. Kadic & M. Wegener. *Mapping acoustical activity in 3D chiral mechanical metamaterials onto micropolar continuum elasticity.* Journal of the Mechanics and Physics of Solids, vol. 137, page 103877, 2020.

[Chen 20d] Y. Chen, M. Kadic, S. Guenneau & M. Wegener. *Isotropic chiral acoustic phonons in 3D quasicrystalline metamaterials.* Physical Review Letters, vol. 124, no. 23, page 235502, 2020.

[Chen 21] Y. Chen, T. Frenzel, Q. Zhang, M. Kadic & M. Wegener. *Cubic metamaterial crystal supporting broadband isotropic chiral phonons.* Physical Review Materials, vol. 5, no. 2, page 025201, 2021.

[Christensen 86] R. Christensen. *Mechanics of low density materials.* Journal of the Mechanics and Physics of Solids, vol. 34, no. 6, pages 563–578, 1986.

[Christensen 15] J. Christensen, M. Kadic, O. Kraft & M. Wegener. *Vibrant times for mechanical metamaterials.* Mrs Communications, vol. 5, no. 3, pages 453–462, 2015.

[Coulais 16] C. Coulais, E. Teomy, K. De Reus, Y. Shokef & M. Van Hecke. *Combinatorial design of textured mechanical metamaterials.* Nature, vol. 535, no. 7613, pages 529–532, 2016.

[Coulais 18] C. Coulais, A. Sabbadini, F. Vink & M. van Hecke. *Multi-step self-guided pathways for shape-changing metamaterials.* Nature, vol. 561, no. 7724, pages 512–515, 2018.

[Craster 12] R. V. Craster & S. Guenneau. Acoustic metamaterials: Negative refraction, imaging, lensing and cloaking. Springer Science & Business Media, 2012.

[Crook 20] C. Crook, J. Bauer, A. G. Izard, C. S. de Oliveira, J. M. d. S. e Silva, J. B. Berger & L. Valdevit. *Plate-nanolattices at the theoretical limit of stiffness and strength.* Nature communications, vol. 11, no. 1, pages 1–11, 2020.

[Deb 02] K. Deb, A. Pratap, S. Agarwal & T. Meyarivan. *A fast and elitist multiobjective genetic algorithm: NSGA-II*. IEEE transactions on evolutionary computation, vol. 6, no. 2, pages 182–197, 2002.

[Deshpande 01a] V. S. Deshpande, N. A. Fleck & M. F. Ashby. *Effective properties of the octet-truss lattice material*. Journal of the Mechanics and Physics of Solids, vol. 49, no. 8, pages 1747–1769, 2001.

[Deshpande 01b] V. Deshpande, M. Ashby & N. Fleck. *Foam topology: bending versus stretching dominated architectures*. Acta materialia, vol. 49, no. 6, pages 1035–1040, 2001.

[Deubel 04] M. Deubel, G. Von Freymann, M. Wegener, S. Pereira, K. Busch & C. M. Soukoulis. *Direct laser writing of three-dimensional photonic-crystal templates for telecommunications*. Nature materials, vol. 3, no. 7, pages 444–447, 2004.

[Eberl 06] C. Eberl, R. Thompson, D. Gianola & S. Bundschuh. *Digital image correlation and tracking with Matlab*. Matlab Central file exchange, 2006.

[Fang 06] N. Fang, D. Xi, J. Xu, M. Ambati, W. Srituravanich, C. Sun & X. Zhang. *Ultrasonic metamaterials with negative modulus*. Nature materials, vol. 5, no. 6, pages 452–456, 2006.

[Florijn 14] B. Florijn, C. Coulais & M. van Hecke. *Programmable mechanical metamaterials*. Physical review letters, vol. 113, no. 17, page 175503, 2014.

[Fortes 89] M. Fortes & M. T. Nogueira. *The poison effect in cork*. Materials Science and Engineering: A, vol. 122, no. 2, pages 227–232, 1989.

[Frenzel 16] T. Frenzel, C. Findeisen, M. Kadic, P. Gumbsch & M. Wegener. *Tailored buckling microlattices as reusable lightweight shock absorbers*. Advanced Materials, vol. 28, no. 28, pages 5865–5870, 2016.

[Frenzel 17] T. Frenzel, M. Kadic & M. Wegener. *Three-dimensional mechanical metamaterials with a twist*. Science, vol. 358, no. 6366, pages 1072–1074, 2017.

[Frenzel 19] T. Frenzel, J. Köpfler, E. Jung, M. Kadic & M. Wegener. *Ultrasound experiments on acoustical activity in chiral mechanical metamaterials*. Nature communications, vol. 10, no. 1, pages 1–6, 2019.

[Gercek 07] H. Gercek. *Poisson's ratio values for rocks*. International Journal of Rock Mechanics and Mining Sciences, vol. 44, no. 1, pages 1–13, 2007.

[Gibson 81] L. Gibson, K. Easterling & M. F. Ashby. *The structure and mechanics of cork*. Proceedings of the Royal Society of London. A. Mathematical and Physical Sciences, vol. 377, no. 1769, pages 99–117, 1981.

[Gibson 99a] L. Gibson & M. Ashby. *Cellular Solids: Structure and Properties. Cambridge Univ Press*. Cambridge, UK, 1999.

[Gibson 99b] L. J. Gibson & M. F. Ashby. Cellular solids: structure and properties. Cambridge University Press, 1999.

[Greaves 11] G. N. Greaves, A. L. Greer, R. S. Lakes & T. Rouxel. *Poisson's ratio and modern materials*. Nature Materials, vol. 10, pages 823–836, 2011.

[Grima 06] J. N. Grima, R. Gatt, N. Ravirala, A. Alderson & K. E. Evans. *Negative Poisson's ratios in cellular foam materials*. Materials Science and Engineering: A, vol. 423, no. 1-2, pages 214–218, 2006.

[Gu 15] X. W. Gu & J. R. Greer. *Ultra-strong architected Cu meso-lattices*. Extreme Mechanics Letters, vol. 2, pages 7–14, 2015.

[Gümrük 13] R. Gümrük & R. Mines. *Compressive behaviour of stainless steel micro-lattice structures*. International Journal of Mechanical Sciences, vol. 68, pages 125–139, 2013.

[Gurtner 14] G. Gurtner & M. Durand. *Stiffest elastic networks*. Proceedings of the Royal Society A: Mathematical, Physical and Engineering Sciences, vol. 470, no. 2164, page 20130611, 2014.

[Guth 15] D. Guth, M. Luersen & P. Muñoz-Rojas. *Optimization of three-dimensional truss-like periodic materials considering isotropy constraints*. Structural and Multidisciplinary Optimization, vol. 52, no. 5, pages 889–901, 2015.

[Hill 52] R. Hill. *The elastic behaviour of a crystalline aggregate.* Proceedings of the Physical Society. Section A, vol. 65, no. 5, page 349, 1952.

[Hou 12] X. Hou, H. Hu & V. Silberschmidt. *A novel concept to develop composite structures with isotropic negative Poisson's ratio: Effects of random inclusions.* Composites science and technology, vol. 72, no. 15, pages 1848–1854, 2012.

[Huang 16] Y. Huang, X. Lu, G. Liang & Z. Xu. *Pentamodal property and acoustic band gaps of pentamode metamaterials with different cross-section shapes.* Physics Letters A, vol. 380, no. 13, pages 1334–1338, 2016.

[Hutchinson 01] J. Hutchinson. *Shear coefficients for Timoshenko beam theory.* J. Appl. Mech., vol. 68, no. 1, pages 87–92, 2001.

[Jang 13] D. Jang, L. R. Meza, F. Greer & J. R. Greer. *Fabrication and deformation of three-dimensional hollow ceramic nanostructures.* Nature materials, vol. 12, no. 10, pages 893–898, 2013.

[Kadic 12] M. Kadic, T. Bückmann, N. Stenger, M. Thiel & M. Wegener. *On the practicability of pentamode mechanical metamaterials.* Applied Physics Letters, vol. 100, no. 19, page 191901, 2012.

[Khelif 16] A. Khelif & A. Adibi, editeurs. Phononic crystals. Springer, Amsterdam, 2016.

[Knowles 15] K. M. Knowles & P. R. Howie. *The directional dependence of elastic stiffness and compliance shear coefficients and shear moduli in cubic materials.* Journal of Elasticity, vol. 120, no. 1, pages 87–108, 2015.

[Latture 18] R. M. Latture, M. R. Begley & F. W. Zok. *Design and mechanical properties of elastically isotropic trusses.* Journal of Materials Research, vol. 33, no. 3, pages 249–263, 2018.

[Laude 15] V. Laude. Phononic crystals: artificial crystals for sonic, acoustic, and elastic waves, volume 26. Walter de Gruyter GmbH & Co KG, 2015.

[Li 04] S. Li & A. Wongsto. *Unit cells for micromechanical analyses of particle-reinforced composites.* Mechanics of materials, vol. 36, no. 7, pages 543–572, 2004.

[Mak 00] M.-W. Mak & S.-Y. Kung. *Estimation of elliptical basis function parameters by the EM algorithm with application to speaker verification.* IEEE Transactions on Neural Networks, vol. 11, no. 4, pages 961–969, 2000.

[Messner 16] M. C. Messner. *Optimal lattice-structured materials.* Journal of the Mechanics and Physics of Solids, vol. 96, pages 162–183, 2016.

[Meyers 08] M. A. Meyers & K. K. Chawla. Mechanical behavior of materials. Cambridge university press, 2008.

[Meza 14] L. R. Meza, S. Das & J. R. Greer. *Strong, lightweight, and recoverable three-dimensional ceramic nanolattices.* Science, vol. 345, no. 6202, pages 1322–1326, 2014.

[Meza 17] L. R. Meza, G. P. Phlipot, C. M. Portela, A. Maggi, L. C. Montemayor, A. Comella, D. M. Kochmann & J. R. Greer. *Reexamining the mechanical property space of three-dimensional lattice architectures.* Acta Materialia, vol. 140, pages 424–432, 2017.

[Milton 95] G. W. Milton & A. V. Cherkaev. *Which elasticity tensors are realizable?* Journal of engineering materials and technology, vol. 117, no. 4, pages 483–493, 1995.

[Nguyen 16] B. D. Nguyen, J. S. Cho & K. Kang. *Optimal design of "Shellular", a micro-architectured material with ultralow density.* Materials & Design, vol. 95, pages 490–500, 2016.

[Paszkiewicz 02] T. Paszkiewicz, M. Pruchnik & P. Zieliński. *Elastic instabilities, phase transitions and soft modes in cubic media.* Physica B: Condensed Matter, vol. 316, pages 186–189, 2002.

[Rand 07] O. Rand & V. Rovenski. Analytical methods in anisotropic elasticity: with symbolic computational tools. Springer Science & Business Media, 2007.

[Schaedler 11] T. A. Schaedler, A. J. Jacobsen, A. Torrents, A. E. Sorensen, J. Lian, J. R. Greer, L. Valdevit & W. B. Carter. *Ultralight metallic microlattices.* Science, vol. 334, no. 6058, pages 962–965, 2011.

[Schilling 01] R. J. Schilling, J. J. Carroll & A. F. Al-Ajlouni. *Approximation of nonlinear systems with radial basis function neural networks.* IEEE Transactions on neural networks, vol. 12, no. 1, pages 1–15, 2001.

[Schittny 14] R. Schittny, M. Kadic, T. Bückmann & M. Wegener. *Invisibility cloaking in a diffusive light scattering medium*. Science, vol. 345, no. 6195, pages 427–429, 2014.

[Shi 18] L. Shi & B. Sun. *Modeling and optimization of vibration response characteristics of the orbital sander based on surrogate model*. Structural and Multidisciplinary Optimization, vol. 57, no. 6, pages 2259–2271, 2018.

[Sigmund 95] O. Sigmund. *Tailoring materials with prescribed elastic properties*. Mechanics of Materials, vol. 20, no. 4, pages 351–368, 1995.

[Sokolnikoff 56] I. S. Sokolnikoff, R. D. Specht*et al.* Mathematical theory of elasticity, volume 83. McGraw-Hill New York, 1956.

[Suwas 14] S. Suwas & N. P. Gurao. Crystallographic texture of materials. 2014.

[Tan 19] X. Tan, B. Wang, S. Zhu, S. Chen, K. Yao, P. Xu, L. Wu & Y. Sun. *Novel multidirectional negative stiffness mechanical metamaterials*. Smart Materials and Structures, vol. 29, no. 1, page 015037, 2019.

[Tan 20] X. Tan, S. Chen, B. Wang, J. Tang, L. Wang, S. Zhu, K. Yao & P. Xu. *Real-time tunable negative stiffness mechanical metamaterial*. Extreme Mechanics Letters, vol. 41, page 100990, 2020.

[Tancogne-Dejean 16] T. Tancogne-Dejean, A. B. Spierings & D. Mohr. *Additively-manufactured metallic micro-lattice materials for high specific energy absorption under static and dynamic loading*. Acta Materialia, vol. 116, pages 14–28, 2016.

[Tancogne-Dejean 18a] T. Tancogne-Dejean, M. Diamantopoulou, M. B. Gorji, C. Bonatti & D. Mohr. *3D Plate-Lattices: An Emerging Class of Low-Density Metamaterial Exhibiting Optimal Isotropic Stiffness*. Advanced Materials, vol. 30, no. 45, page 1803334, 2018.

[Tancogne-Dejean 18b] T. Tancogne-Dejean & D. Mohr. *Elastically-isotropic elementary cubic lattices composed of tailored hollow beams*. Extreme Mechanics Letters, vol. 22, pages 13–18, 2018.

[Tancogne-Dejean 18c] T. Tancogne-Dejean & D. Mohr. *Elastically-isotropic truss lattice materials of reduced plastic anisotropy*. International Journal of Solids and Structures, vol. 138, pages 24–39, 2018.

[Tancogne-Dejean 18d] T. Tancogne-Dejean & D. Mohr. *Stiffness and specific energy absorption of additively-manufactured metallic BCC metamaterials composed of tapered beams*. International Journal of Mechanical Sciences, vol. 141, pages 101–116, 2018.

[Tao 20] Q. Tao, C. Wang, K. Wang, Z. Xie & H. Tan. *Mixed-mode bending of a smart reconfigurable lattice structure with bi-directional corrugated core*. International Journal of Mechanical Sciences, page 105848, 2020.

[Timoshenko 70] S. Timoshenko & J. Goodier. *Theory of Elasticity*, 1970.

[Tsang 83] T. Tsang & H.-Y. Park. *Sound velocity anisotropy in cubic crystals*. Physics Letters A, vol. 99, no. 8, pages 377–380, 1983.

[Ushijima 11] K. Ushijima, W. Cantwell, R. Mines, S. Tsopanos & M. Smith. *An investigation into the compressive properties of stainless steel micro-lattice structures*. Journal of Sandwich Structures & Materials, vol. 13, no. 3, pages 303–329, 2011.

[Valdevit 13] L. Valdevit, S. W. Godfrey, T. A. Schaedler, A. J. Jacobsen & W. B. Carter. *Compressive strength of hollow microlattices: Experimental characterization, modeling, and optimal design*. Journal of Materials Research, vol. 28, no. 17, pages 2461–2473, 2013.

[Voigt 10] W. Voigt. Lehrbuch der kristallphysik:(mit ausschluss der kristalloptik), volume 34. BG Teubner, 1910.

[Wang 20] Y. Wang & O. Sigmund. *Quasiperiodic mechanical metamaterials with extreme isotropic stiffness*. Extreme Mechanics Letters, vol. 34, page 100596, 2020.

[Wojciechowski 05] K. W. Wojciechowski. *Poisson's ratio of anisotropic systems*. Computational methods in science and technology, vol. 11, no. 1, pages 73–79, 2005.

[Wojciechowski 15] K. W. Wojciechowski, F. Scarpa, J. N. Grima & A. Alderson. *Auxetics and other systems of "negative" characteristics*. physica status solidi b, vol. 252, no. 7, pages 1421–1425, 2015.

[Xu 16] S. Xu, J. Shen, S. Zhou, X. Huang & Y. M. Xie. *Design of lattice structures with controlled anisotropy*. Materials & Design, vol. 93, pages 443–447, 2016.

[Yang 20] H. Yang & L. Ma. *1D to 3D multi-stable architected materials with zero Poisson's ratio and controllable thermal expansion.* Materials & Design, vol. 188, page 108430, 2020.

[Zheng 14] X. Zheng, H. Lee, T. H. Weisgraber, M. Shusteff, J. DeOtte, E. B. Duoss, J. D. Kuntz, M. M. Biener, Q. Ge, J. A. Jackson*et al. Ultralight, ultrastiff mechanical metamaterials.* Science, vol. 344, no. 6190, pages 1373–1377, 2014.

[Zhu 19] S. Zhu, X. Tan, B. Wang, S. Chen, J. Hu, L. Ma & L. Wu. *Bio-inspired multistable metamaterials with reusable large deformation and ultra-high mechanical performance.* Extreme Mechanics Letters, vol. 32, page 100548, 2019.

[Zok 16] F. W. Zok, R. M. Latture & M. R. Begley. *Periodic truss structures.* Journal of the Mechanics and Physics of Solids, vol. 96, pages 184–203, 2016.

# List of Figures

# List of Tables

sPIM

**Titre :** Conception nodale des métamatériaux mécaniques en treillis
**Mots clefs:** Effet nodal, métamatériau mécanique

**Résumé :** Les joints ou nœuds avec une configuration géométrique complexe connectant des tiges se trouvent couramment dans les matériaux en treillis. L'existence des nœuds a un impact certain sur les propriétés mécaniques du réseau. La thèse s'intéresse principalement aux treillis cubiques élémentaires de poutres. La première innovation que nous proposons est un modèle analytique pour identifier les effets nodaux et de flexion sur la réponse en compression du réseau FCC. Sur la base des résultats obtenus, des métamatériaux mécaniques tubulaires BCC de forme ouverte ultra-résistants et légers sont présentés pour supporter la charge et absorber l'énergie. Le choix du nœud offre la possibilité de contrôler l'isotropie élastique des métamatériaux. Nous proposons une nouvelle classe de treillis élastiquement isotropes et légers, dominés par la flexion, en remplaçant le nœud interne du treillis BCC par un treillis SC. Des simulations numériques révèlent que les réseaux proposés possèdent non seulement une isotropie élastique, mais aussi une réponse non linéaire presque isotrope. En particulier, notre matériau avec une densité relative inférieure à 1% atteint presque la limite supérieure du coefficient de Poisson pour un matériau isotrope. Nous proposons également une nouvelle classe de métamatériau isotrope et réutilisable de type liège, qui est conçu à partir d'un matériau hybride en treillis avec une connexion de nœud complexe qui permet d'obtenir un coefficient de Poisson isotrope proche de zéro. Il peut récupérer 96,6 % de sa forme originale après un test de compression dépassant 20 % de déformation. Des tests de compression uniaxiale sont effectués pour toutes les conceptions proposées.

**Title :** Nodal design of lattice mechanical metamaterials

**Keywords :** Nodal effect, Mechanical metamaterial

**Abstract :** Joints or nodes with complex geometrical configuration at the connection between rods are commonly found in lattice materials. The existence of nodes definitely has a determinant impact on the mechanical properties of the lattice materials. The main focus of this thesis is elementary cubic truss lattices. The first innovation that is proposed is an analytical model to identify the effect of nodes and bending on the compressive response of FCC lattices. Based on the obtained result, lightweight ultra-strong open-form BCC shellular and closed-form SC tubular mechanical materials are presented, for supporting load and absorbing energy. The choice of nodes provides one with a possibility to control the elastic isotropy of lattice materials. We propose a new class of light-weight elastic isotropic bending-dominated truss lattice by replacing the inner node of the BCC lattice with a SC lattice. Numerical simulations reveal that the proposed lattices not only exhibit elastic isotropy but also a nearly isotropic nonlinear response. We also propose a new class of isotropic and reusable cork-like metamaterial that is designed from an hybrid truss-lattice material with complex node connection. The metamaterial shows an isotropic Poisson's ratio close to zero. It can recover 96.6% of its original shape after a compressional test exceeding 20% strain. Uniaxial compression tests are performed to confirm the designs in all cases.

UBFC UNIVERSITÉ BOURGOGNE FRANCHE-COMTÉ
Université Bourgogne Franche-Comté
32, avenue de l'Observatoire
25000 Besançon